UNIVERSITÀ DEGLI STUDI DI PADOVA

SEDE AMMINISTRATIVA: UNIVERSITÀ DEGLI STUDI DI PADOVA

DIPARTIMENTO DI BIOLOGIA

SCUOLA DI DOTTORATO DI RICERCA IN BIOSCIENZE E BIOTECNOLOGIE

INDIRIZZO: BIOTECNOLOGIE

CICLO XXV

UNRAVELING THE MECHANISMS OF ALPHA-SYNUCLEIN AGGREGATION AND TOXICITY

Direttore della Scuola: Ch.mo Prof. Giuseppe Zanotti

Coordinatore d'indirizzo: Ch.mo Prof. Giorgio Valle

Supervisore: Ch.mo Prof. Luigi Bubacco

Dottoranda: Nicoletta Plotegher

Table of contents

Abstract

Parkinson's disease is the second most common neurodegenerative disorder after Alzheimer's disease and affects about 1% of the population over 65 years old. This disorder can be both sporadic and familial and some genetic forms are due to mutations in *SNCA* gene, encoding for the protein alpha-synuclein (aS).

PD pathological hallmarks are the prominent death of the dopaminergic neurons in the *substantia nigra pars compacta* and the presence of proteins and lipid inclusions, termed Lewy's body (LBs), in the surviving neurons in parkinsonian brains. The main constituent of LBs is an aggregated fibrillar β-sheet rich form of aS. aS aggregation process was widely studied in the past years: the protein is unfolded in its native state, but in pathological conditions it tends to aggregate forming oligomeric species. These oligomers constitute a heterogeneous and transient ensemble and rapidly convert into amyloid fibrils when they reach a critical concentration. Amyloid fibrils then deposit in LBs along with several other proteins and lipids.

aS aggregation was mainly studied *in vitro*, but recently more efforts were put into the study of this process in cell and animal models, to identify not only aS aggregation intermediates, but also the associated toxic mechanism(s) that lead to neurons cell death in PD.

In this thesis two main issues were faced: the study of aS aggregation in cells using unconventional methods and the characterization of the effects of the family of chaperone-like proteins 14-3-3, on aS aggregation.

In the first part, two cellular models for the study of aS aggregation were set and characterized: the first one is obtained just overexpressing aS and allowed the characterization of an ensemble of heterogeneous oligomeric species (about 6±4 monomers per oligomer) using a new fluorescence microscopy method termed Number and Brightness analysis. These oligomeric species induced autophagic lysosomal pathway activation and mitochondrial fragmentation in this model.

The second cellular model provides a method to study aS fibrils and larger aggregates in a physiological environment: aS was overexpressed in cells

and aggregation was triggered by introducing in cell cytoplasm recombinant aS fibrils fragments, termed seeds. In both cases aS overexpression and aggregation cause cellular death, in good agreement with what was previously published by others groups.

The characterization of aS aggregation in cells went further looking at the variation in cellular metabolism, possibly induced by mitochondrial damage. These changes were quantified measuring NADH fluorescence properties in the two models with respect to the control. These results showed that in cells presenting aS oligomer or aggregates, NADH fluorescence lifetime and emission spectra change, suggesting that these measurements may be used to detect aS aggregates in live cells and in vivo using a non-invasive dye-free method.

The second part of the thesis concerns the ability of 14-3-3 chaperone-like proteins of interacting with aS and of interfering with aS aggregation process rescuing the induced toxicity in cells.

Among the seven 14-3-3 isoforms, 14-3-3 η can re-route aS amyloidogenic process *in vitro*, leading to the formation of curved objects rather than aS fibrils. These curved objects have diameters and curvatures that depend on 14-3-3 η amount in the aggregation assays; moreover, 14-3-3 η molecules were found in these aggregates, suggesting the formation of a stable complex between the two proteins. When aS amount is too large or seeds are used to trigger the aggregation process *in vitro*, 14-3-3 η is not able any more to affect aS aggregation and is sequestered into aS fibrils.

In cell models, 14-3-3 η overexpression leads to a rescue when aS was only overexpressed, but not when aggregation in cell cytoplasm was triggered by seeds. Overexpressed 14-3-3 η was found to interact with overexpressed aS using image correlation spectroscopy methods (cross raster image correlation spectroscopy and cross Number and Brightness analysis), mainly at plasma membrane. Moreover, 14-3-3 η is sequestered into aggregates when aS aggregation is triggered by seeds, highlighting another possible toxic mechanism due to aS aggregation. All the results obtained in cells are in good agreement with the *in vitro* results previously reported, further suggesting that 14-3-3 proteins and η isoform in particular are interesting in aS aggregation frame and may be used to interfere in the process to rescue its toxic effects.

Riassunto

La malattina di Parkinson è la seconda malattia neurodegenerative più comune dopo il morbo di Alzheimer e colpisce circa l'1% delle popolazione sopra i 65 anni di età. Questa malattia può essere sia sporadica che familiare e alcune forme genetiche sono dovute a mutazioni nel gene *SNCA* che codifica per la proteina alfa-sinucleina.

Le caratteristiche patologiche principali della malattia di Parkinson sono la morte prevalentemente dei neuroni dopaminergici della *substantia nigra pars compacta* e la presentza di inclusioni proteiche e lipidiche, dette corpi di Lewy, nei neuroni che sopravvivono nei cervelli dei pazienti affetti dalla malattia.

Il componente principale dei corpi di Lewy è una forma di alfa-sinucleina aggregata, fibrillare e ricca di foglietti beta. Il processo di aggregazione di alfa-sinucleina è stato ampiamente studiato negli anni passati: la proteina è non strutturata nella sua forma nativa, ma in condizioni patologiche tende ad aggregare formando specie oligomeriche. Questi oligomeri costituiscono un insieme etereogeneo e transiente e si convertono rapidamente in fibrille amiloidi quando raggiungono una concentrazione critica. Le fibrille amiloidi di alfa-sinucleina si depositano poi nei corpi di Lewy assieme ad altre proteine e lipidi.

L'aggregazione di alfa-sinucleina è stata principalmente studiata *in vitro*, anche se più recentemente maggiori sforzi sono stati effettuati per caratterizzare il processo in modelli cellulari ed animali, per identificare non soltanto i diversi prodotti dell'aggregazione, ma anche i meccanismi tossici ad essi associati, che causano la morte dei neuroni nei pazienti affetti dalla malattia di Parkinson.

In questa tesi due questioni principali sono state affrontate: lo studio dell'aggregazione di alfa-sinucleina in cellule utilizzando metodi non convenzionali di microscopia in fluorescenza e la caratterizzazione degli effetti di una famiglia di proteine chaperoniche, le 14-3-3, sul processo di aggregazione.

Nella prima parte, due modelli cellulari per lo studio dell'aggregazione di alfa-sinucleina sono stati approntati e caratterizzati: il primo viene ottenuto

sovraesprimento soltanto alfa-sinucleina e ha permesso la caratterizzazione di un ensemble di oligomeri eterogenei in cellule vive (circa 6±4 monomeri per oligomero) utilizzando un nuovo metodo di microscopia in fluorescenza chiamato *Number and Brightness analysis.* Queste specie oligomeriche inducono l'attivazione del sistema autofagico-lisosomiale e la frammentazione dei mitocondri in questo modello cellulare.

Il secondo modello cellulare fornisce un metodo per lo studio delle fibrille di alfa-sinucleina e di aggregati più grandi in un ambiente di rilevanza fisiologica: alfa-sinucleina è stata sovrespressa in cellule e l'aggregazione è stata promossa introducendo nel citoplasma delle cellule frammenti di fibrille ottenute da alfa-sinucleina ricombinante, detti *seeds*. In entrambi i casi la sovraespressione e l'aggregazione di alfa-sinucleina hanno causato morte cellulare, in buon accordo con quello che è stato riportato in precedenza da altri gruppi di ricerca.

La caratterizzazione dell'aggregazione di alfa-sinucleina in cellule è continuata osservando la variazione nel metabolismo cellulare, potenzialmente indotta da danni ai mitocondri. Queste variazione sono state quantificate misurando le proprietà della fluorescenza del NADH nei due modelli, rispetto al controllo. Questi risultati hanno mostrato che in cellule che presentano oligomeri o aggregati di alfa-sinucleina, il tempo di vita della fluorescenza del NADH e il suo spettro di emissione cambiano. Quindi, queste misure potrebbero essere ottimizzare per rilevare la presenza di aggregati di alfa-sinucleina in cellule e in vivo, utilizzando un metodo di indagine non invasivo e *dye-free*.

La seconda parte della tesi riguarda l'abilità delle proteine chaperoniche 14-3-3 di interagire con alfa-sinucleina e di interferire con il suo processo di aggregazione, riducendone la tossicità in cellule.

Tra le sette isoforme della famiglia di 14-3-3, la 14-3-3 η può revertire il processo di fibrillazione di alfa-sinucleina *in vitro*, portando alla formazione di oggetti curvi invece che di fibrille canoniche. Questi oggetti curvi hanno diametri e curvature che dipendono dalla quantità di 14-3-3 η nel saggio di aggregazione: inoltre, molecole di 14-3-3 η sono state trovate in questi aggregati, suggerendo la formazione di un complesso stabile costituito dalle due proteine. Quanto la quantità di alfa-sinucleina è troppo grande o i *seeds* vengono

utilizzati per promuovere il processo di aggregazione *in vitro*, la 14-3-3 η non è più in grado di interferire con il processo di aggregazione di alfa-sinucleina e viene sequestrata nelle fibrille.

Nei modelli cellulari, la sovraespressione di 14-3-3 η riduce la tossicità indotta da alfa-sinucleina quando quest'ultima è soltato sovraespressa e oligomerizza, ma non quando l'aggregazione in cellule viene promossa dai *seeds*.

È stato mostrato, utilizzando tecniche di *image correlation spectroscopy* (*cross raster image correlation spectroscopy* e *cross Number and Brightness analysis*) che la 14-3-3 η sovraespressa può interagire con alfa-sinucleina sovraespressa, principalmente alla membrana plasmatica.

Inoltre, la 14-3-3 η viene sequestrata negli aggregati quando il processo di aggregazione di alfa-sinucleina è indotto dai *seeds*, evidenziando un altro possibile meccanismo di tossicità dovuto all'aggregazione.

Tutti i risultati ottenuti in cellule sono in buon accordo con i risultati ottenuti *in vitro* e precedentemente riportati; questo rafforza ulteriormente l'idea che le proteine 14-3-3 e in particolare l'isoforma η siano particolarmente interessanti nel contesto dello studio dell'aggregazione di alfa-sinucleina e che potrebbero essere utilizzare per interferire con il processo di aggregazione e ridurne gli effetti tossici.

Chapter 1

Introduction

"In the fields of observation chance favors only the prepared mind."

Louis Pasteur

1.1 Parkinson's disease

1.1.1 Etiopathogenesis and clinical features

Parkinson's disease (PD) is the second most common neurodegenerative disorder after Alzheimer's disease and affects about 1% of the population over 60 years old (de Lau *et al*., 2006).

PD is a motor disorder, characterized by both motor and non-motor symptoms. The motor symptoms include resting tremors, usually unilateral and in the most distal part of the limbs; rigidity, due to an increased resistance in the joints; bradikinesia or akinesia, i.e. slowing down of the movements; difficulties in planning, initiating and executing movements; postural instability, mainly in the last stages of the disease (Jankovic, 2008). Non-motor symptoms are cardiovascular or gastrointestinal symptoms, hyposmia and olfactory dysfunctions, anxiety, depression and dementia (Dickson *et al*., 2009).

Pathologically, PD is characterized by the prevailing death of the dopaminergic neurons in the *substantia nigra pars compacta* (Figure 1.1).

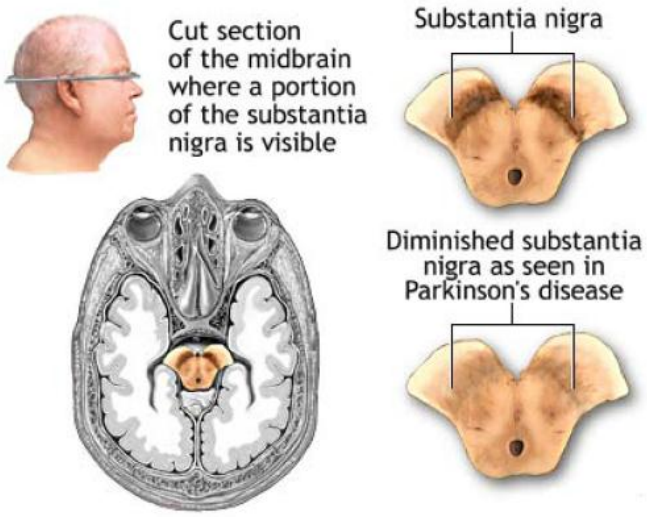

Figure 1.1 – Comparison between the *substantia nigra pars compacta* in a healthy and a PD-affected brain, showing the loss of pigmentation due to prominent dopaminergic neurons death.

Functional imaging (i.e. positron emission tomography) suggests that about 60% of the dopaminergic neurons in that region have to

degenerate and about 80% of dopamine depletion has to occur before the first Parkinsonism symptoms display (Dauer and Przedborski, 2003).

Moreover, proteins and lipids aggregates, termed Lewy Bodies (LBs) and Lewy Neurites (LNs), were found in the *post-mortem* analysis of the surviving neurons in brains of patients with a PD diagnosis.

LBs are eosinophilic cytoplasmic inclusions, whose main constituents are ubiquitin and, more important to this thesis, an aggregated form of the proteins alpha-synuclein (aS) (Figure 1.2). Electron microscopy showed that aS present in LBs and LNs is organized into filaments 200-600 nm long and with a diameter of 5-10 nm (Spillantini *et al*., 1998). X-ray diffraction revealed that aS filaments in LBs present a β-sheet structure (Serpell *et al*., 2000) characteristic of amyloid fibrils.

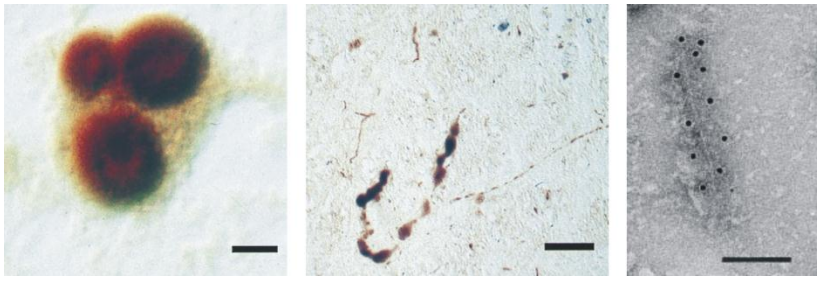

Figure 1.2 – LBs, on the left, and LNs, in the middle, double-stained with aS and ubiquitin antibodies (Scale bar 10 μm and 90 μm respectively). On the right, fibrils purified from LBs and immuno-stained with aS antibody. The gold nanoparticles conjugated with the secondary antibody appears as black dots (Scale bar 100 nm). Adapted from Spillantini *et al.*, 1998.

Braak and co-workers associated the diffusion of LBs in different brain regions to the disease staging (Braak *et al.*, 2003). Pathological studies of healthy and PD affected brains have shown that aS inclusions form in a similar and precise order in the different regions of diseased brains, allowing the identification of six stages of LBs deposition in relationship with PD progression (Braak staging is summarized in Figure 1.3).

Interestingly, aS inclusions can deposit early in the enteric nervous system and in the peripheral nervous system (Braak *et al.*, 2006). It is quite established now that aS pathology starts in some nerve and spreads in a prion-like manner. However, the mechanism(s) by which the pathology diffusion occurs is still unclear and several possibilities were proposed in

the literature and few will be discussed in section 1.3.3 (Goedert *et al.*, 2013).

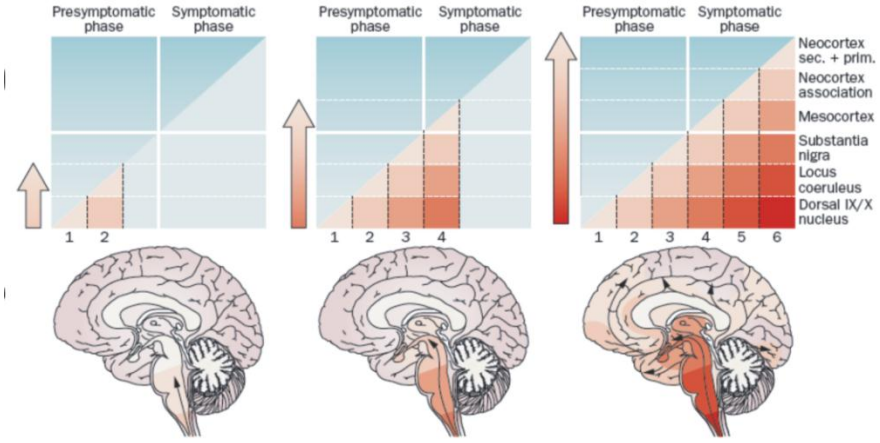

Figure 1.3 – Six stages of PD pathology. Patients with aS deposition belong to one of these stages and disease spreading means involvement of additional brain regions and symptoms worsening. Stage 1: LBs are observed in the olfactory bulb, the anterior olfactory nucleus and/or the dorsal motor nuclei of the vagal and glossopharyngeal nerves in brainstem. Stage 2: lesions occur in the pontine tegmentum. Stage 3: LBs are found in pedunculopontine nucleus, the cholinergic magnocellular nuclei of the basal forebrain, the pars compacta of the substantia nigra. Stage 4: the hypothalamus, portions of the thalamus and the anteromedial temporal mesocortex (first cortical region). First PD symptoms occur during stage 3 and early stage 4. Stage 5-6: lesions emerge in the neocortical high-order association areas (stage5) and first-order association areas and primary fields (stage 6). Adapted from Goedert *et al.*, 2012.

1.1.2 Etiology of Parkinson's disease

PD is mainly sporadic and its etiology remains unclear because it is a multifactorial disorder. Several factors can contribute to the disease etiopathogenesis: protein aggregation, oxidative stress, genetic predisposition, mitochondrial dysfunctions, protein degradation pathways failure and exposure to environmental toxins.

However, about 5-10% of PD cases are genetic and several studies identified genetic loci associated to the disease. In particular, mutations in 5 genes have been identified as strongly related to PD genetic forms. Autosomal recessive early onset forms of this disorder are inherited through mutations in *parkin*, *DJ-1* or *PINK1* genes (Kitada *et al.*, 1998; Bonifati *et al.*, 2003; Valente *et al.*, 2004), that encode for proteins involved in the

maintenance of mitochondrial function in response to oxidative stress (Berman and Hastings, 1999).

Gene (locus)	Inheritance	Dementia	LBs pathology	Mitochondrial regulation	Lysosomal trafficking
***SNCA* (*PARK1-4*)**	AD	++	+++	-	+
***Parkin* (*PARK2*)**	AR	-	+/-	+++	-
***PINK1* (*PARK6*)**	AR	-	+/-	+++	-
***DJ-1* (*PARK7*)**	AR	-	?	+++	-
***LRRK2* (*PARK8*)**	AD	+/-	++	-	+
***ATP13A2* (*PARK9*)**	AR	+++	?	-	+++
***VPS35* (not assigned)**	AD	+/-	?	-	++

Table 1 – Main genes associated to PD. AD = autosomal dominant; AR = autosomal recessive. +++, strong; ++, established; + reported in experimental studies; +/- case series. Adapted from Tofaris, 2012.

Mutations on Leucine-rich repeat kinase 2 (*LRRK2*) gene, encoding for a large multidomain kinase (Funayama *et al.*, 2002) and on *SNCA* gene, encoding for aS, cause autosomal dominant and late onset forms of PD.

Other genes were linked to PD genetic forms; they include vacuolar protein sorting VPS35 gene, which encodes for a subunit of retromer complex, responsible for transmembrane proteins recycling from endosomes to the trans-Golgi network and whose mutation causes autosomal dominant and late-onset PD (Zimprich *et al.*, 2011); *ATP13A2* that encodes for a lysosomal type 5 P-type ATPase responsible for lysosomal acidification (Ramirez *et al.*, 2006; Di Fonzo *et al.*, 2007) and causes a parkinsonism with a complex phenotype and dementia.

Finally, other putative loci and genes have been identified and linked to monogenic forms of PD and to susceptibility for the disorder, as for example glucocerebrosidase *GBA* or ubiquitin carboxyterminal hydrolase 1

UCHL1 (*PARK5*) gene. For extensive reviews see Hardy 2010, Gasser et al., 2011 and Lesage and Brice, 2012.

1.1.3 *SNCA* mutations

SNCA gene was the first gene to be linked to familial PD. In particular, single point mutations, i.e. A30P, E46K and A53T (Polymeropoulos *et al*., 1997; Kruger *et al*. 1998; Zarranz *et al*. 2004) and gene duplication (Chartier-Harlin *et al*. 2004) and triplication (Singleton *et al*. 2003), were recognized as responsible for autosomal dominant form of PD.

Moreover, the susceptibility to PD is increased when polymorphisms are present in some regions of *SNCA* gene, i.e. in 3'UTR or in the promoter region (Fuchs *et al*. 2008).

The detailed effects that these mutations have on the protein structure and functionality will be discussed further on. These familial PD forms establish a further link, after aS fibrils presence in LBs, between this protein and this fatal neurodegenerative disorder.

1.1.4 Clinical treatments

The therapeutic treatments administrated to patients that are diagnosed with PD and show the first symptoms are mainly devoted to the restoring of the depleted dopamine or to symptom treatment, because an actual cure for this disorder has not been discovered yet.

The available drugs are dopamine agonists and the precursor of dopamine levodopa. These drugs are all able to pass the blood barrier and treat the motor symptom of PD, without any effects on the progression on the PD pathology (for a review see Shapira, 2009).

Otherwise a surgical treatment, termed deep brain stimulation (DBS) is available. DBS is based on the stimulation of specific brain regions and allows the alleviation of PD symptoms rather that curing the disease (Krause *et al.*, 2001).

A promising therapeutic strategy comes from the application of stem cell therapy: grafts from human fetal neuronal tissue in PD patients replaced the lost cells and ameliorated the symptoms, proving in principle that this treatment is suitable for PD. However, some issues have to be solved: the tissue availability, the standardization of the grafts, the collateral effects and the fact that the spreading of the disease will hit anyway also the healthy grafted neurons, just postponing the problem instead of solving it (Politis *et al.*, 2012).

1.2 Alpha-synuclein

The fact that aS is the major component of LBs and LNs and that mutations in the gene encoding for the protein lead to autosomal dominant forms of PD made this protein a particularly interesting topic for all the people trying to unravel PD molecular mechanism(s) and etiopathogenesis.

aS is a small protein constituted by 140 amino acids that belongs to the synucleins family (aS, β-synuclein and γ-synuclein), that share a quite high sequence identity and similar expression pattern (Clayton *et al.*, 1998). Synucleins are expressed in all the central nervous system, mainly at presynaptic terminal in mammalian brains, but their physiological functions are still subject of debate.

1.2.1 Alpha-synuclein structure and function

aS does not acquire a secondary structure when purified from heterologous expression system; for this reason it has always been considered a intrinsically disordered protein (Weinreb *et al.*, 1996). However, it has been recently purified as an alpha-helical homotetramer from mammalian cells overexpressing aS and from human red blood cells (Bartels *et al.*, 2011). Other laboratories failed to reproduce the results obtained by Bartels and collaborators, and found aS as an unfolded monomer in central nervous system, in erythrocytes, in mammalian cells and in *E. coli* (Fauvet *et al.*, 2012).

The primary structure of aS can be divided in three parts: N-terminus, non-beta amyloid component (NAC) and C-terminus (Figure 1.4).

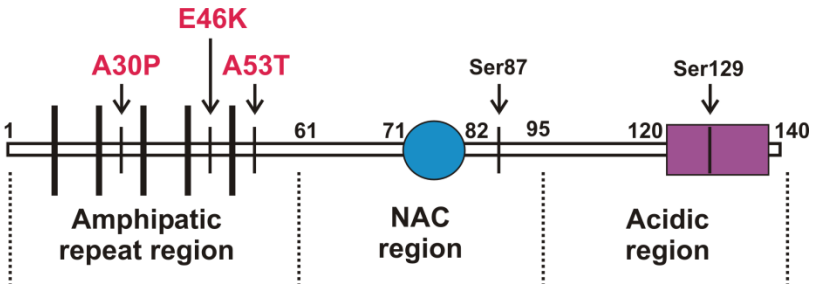

Figure 1.4 – aS primary structure divided into N-terminus, NAC and C-terminus.

N-terminus is constituted by the first 60 amino acids and can form, along with the NAC region, an amphipatic alpha-helix responsible for aS interaction with lipidic membranes (Bartels *et al*., 2010). The single point mutations A30P, E46K and A53T responsible for familial form of PD are all located in this region, accounting for variation in protein-membrane interaction (see 1.2.2) or in protein aggregation propensity (see 1.2.4).

The NAC region, from residue 61 to residue 95, is believed to be responsible for the primary intramolecular interactions that cause aS misfolding and aggregation (Weinreb *et al*., 1996). This region acquires a β-sheet structure when aS forms amyloid fibrils (see 1.2.4.4).

The remaining part of the protein constitutes the C-terminus, which includes 14 acidic residues and does not acquire a defined secondary structure in solution, when aS is bound to the membranes or when it forms amyloid fibrils.

aS physiological function(s) are still not defined, but mounting evidences ascribe to the protein a major role in synaptic vesicles recycling (Lotharius *et al*., 2002), in promoting SNARE-complex assembly (Burrè *et al*. 2010) and in neurotransmitters release (Liu *et al*. 2004). It has been shown that aS is involved in synaptic plasticity and learning (Clayton *et al*., 1998), even if knockout mice are viable and present only an altered dopamine (DA) release and lowered level of striatal DA (Abeliovich *et al*. 2000), supporting the hypothesis that aS can be involved in the modulation of DA release.

Furthermore, the fact that aS can be found in both cytosolic fraction and bound to the membranes in vivo (Lee *et al*., 2002) suggests its involvement in membrane related function(s), as it will be explain in the next paragraph.

1.2.2 Membrane bound alpha-synuclein

aS contains an apolipoprotein repeat motif (KTKEGV) in the first 100 amino acids. For this reason it acquires an alpha-helical secondary structure upon binding to detergent micelles, liposomes (Davidson *et al*.,

1998) or negatively charged lipids or detergents membranes (Jao *et al*., 2004; Jao *et al*., 2008). Alternatively, aS showed interactions with membranes that are composed by a mixture of negative and neutral phospholipids (Davidson *et al*., 1998).

While C-terminus remains unfolded, it is N-terminus that drives aS membrane binding (Bartels *et al*., 2010) and acquires an alpha-helical structure. aS alpha-helix was first described bound to SDS micelles as a broken structure, going from residue 3 to residue 92, with a break from amino acid 37 to 45 (Ulmer *et al*., 2005). Other studies supported this result (Chandra *et al*., 2003; Bisaglia *et al*., 2005), which was further confirmed when aS was studied bound to larger lipid vesicles (Bortolus *et al*., 2008).

Another model proposed the formation of an extended alpha-helix, with a periodicity of 11/3 (Bussel *et al*., 2005). The idea in this case is that the 11 lysine residues lying at the interface between the membrane and the protein are responsible for the binding (Jao *et al*., 2004; Jao *et al*., 2008). The presence of a single extended alpha-helix was also proposed by Georgieva and collaborators (Georgieva *et al*., 2010), but they also proposed that both extended and bent helices were possible conformations that aS N-terminus can acquire when interacting with detergents and lipids (Figure 1.5).

Other studies suggested that aS can exist in both conformations, switching from the extended helix to the broken one depending on the binding partners and on the curvature of the membrane (Ferreon *et al*., 2009; Trexler and Rhoades, 2009). Moreover, it was also shown that aS presents different binding affinities for the membranes depending on the diameters of the membrane vesicles used (Middleton and Rhoades, 2010).

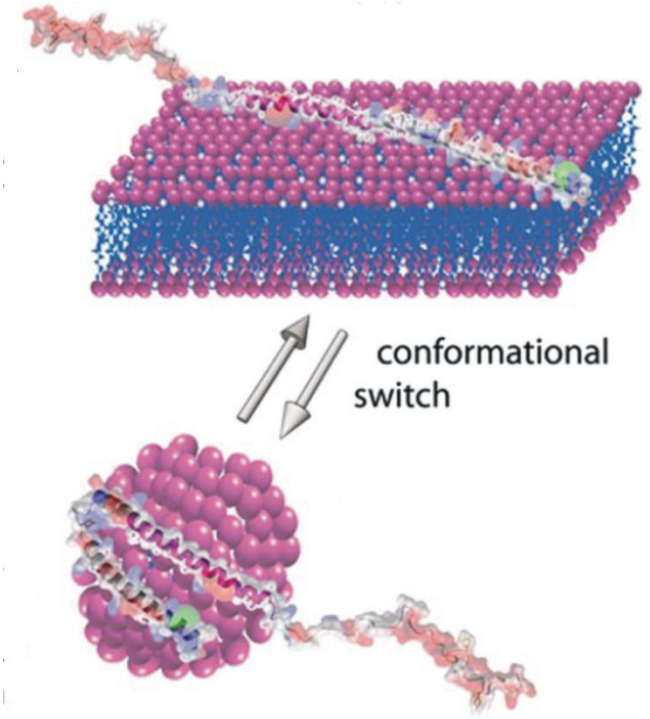

Figure 1.5 – Membrane bound alpha-helical aS conformational changes induced by membranes curvature and lipids concentration. Adapted from Ferreon *et al.*, 2009.

Very interestingly, aS binding to the membranes can induce membrane curvature and membrane tubulation, as apolipoproteins do (Varkey *et al.*, 2010). It has been shown that there is an increased fibrils formation when aS is aggregated in the presence of brain membranes (Lee *et al.*, 2002) and micelles (Necula *et al.*, 2003), meaning that membranes play an important role also in aS aggregation. Moreover, it has been proposed that the binding of aS to the membrane increases the local concentration, favouring the triggering of the aggregation process (Auluck *et al.*, 2010, Lee *et al.*, 2012).

The increase of aS local concentration at the membranes can lead not only to an increased aggregation propensity, but also to membrane permeabilization. It has been shown by different groups that monomeric aS (Zakharov *et al.*, 2007; Tosatto *et al.* 2012) and aS oligomers (Kim *et al.*, 2009; van Rooijen *et al.*, 2010) can form pores with defined conductance levels in lipid membranes upon the application of a potential.

The pathological mutants affect aS membrane binding properties; in particular, A30P seems to have a lower ability to interact with lipid

membranes *in vitro* (Perrin *et al*., 2000; Jo *et al*., 2002), while E46K interacts more easily with negatively charged liposomes, compared to wild type aS (Choi *et al*., 2004). On the contrary, A53T seems to be less affected in term of membrane binding variations in comparison to the others (Perrin *et al*., 2000). Accordingly, structural studies suggest that A53T does not show any variations when bound to SDS micelles, while A30P induces a slight destabilization in the alpha-helical structure close to the site of the mutation (Bussell *et al*., 2004). Similar NMR studies were performed by Fredenburg and co-workers (Fredenburg *et al*., 2007), which lead to the conclusion that the modification induced by this mutation does not induce relevant alteration of the protein alpha-helical propensity.

Altogether these indications support the idea of a crucial role for membrane bound aS not only in the protein physiological function, but also in PD pathogenesis.

1.2.3 Alpha-synuclein aggregation *in vitro*

As previously mentioned, a fibrillar β-sheet rich form of aS is the major component of LBs and LNs (Spillantini *et al*., 1998). Considering the presence of aS aggregated forms into LBs and the PD-related single point mutations that could affect aS stability, functionality and aggregation propensity, a significant effort was put over the years into the study of the aS aggregation process *in vitro*. These studies are simplify by the availability of recombinant aS, which can be easily expressed in *E. coli* and purified in quite large amount and to a high purity. The interest is related not only to aS fibrillization process and aS fibrils, but also to the early aS oligomeric intermediates and to those molecules that could interfere with aS aggregation. In the next sections a brief presentation of aS aggregation kinetics and aS aggregates obtained *in vitro* can be found.

1.2.3.1 Aggregation prone alpha-synuclein

Natively unfolded aS, in pathological conditions, acquires a structure prone to aggregate. It is still not clear how this conversion

occurs, but considering the importance of this event in the initiation of the oligomerization, it has been studied in two different conditions: in solution or at the lipidic membranes.

aS conformational changes were studied in solution by nuclear magnetic resonance and molecular dynamics (Dedmon *et al*., 2004; Bertoncini *et al*., 2005; Allison *et al*., 2009), and single molecule fluorescence techniques (Trexler *et al*., 2010; Yap *et al*., 2011).

All the studies on aS in solution *in vitro* converged upon the identification of long range interactions between C-terminus and the central part of the protein and continuous rearrangements of the two termini. This means that the unfolded state of aS in solution is constituted by an ensemble of different, transient and dynamic conformations.

Some of these conformations can be, in particular conditions, prone to establish transient or stable bounds with other aS molecules and corresponding to a favorable form. This conformation is an energy minimum and drives the first steps of protein oligomerization.

The increased aS aggregation propensity in the presence of membranes (Lee *et al*., 2002; Necula *et al*., 2003) could mean that aS alpha-helical structure directly converts into a β-sheet aggregation prone conformation, as it has been shown for other amyloidogenic proteins (reviewed in Butterfield and Lashuel, 2010).

1.2.3.2 Alpha-synuclein aggregation kinetics

The first steps of self-interaction of aS monomers occur rarely. It is primary driven by hydrophobic interactions due to a hydrophobic stretch in the middle of aS sequence (from residue 71 to 82), constituted by 12 amino acids (VTGVTAVAQKTV) (Giasson *et al*., 2001).

After these first steps, monomers start to aggregate and form oligomeric species. As soon as their concentration reaches a critical point, these oligomers are rapidly converted into protofilaments, protofibrils and, finally, into amyloid fibrils (Figure 1.6).

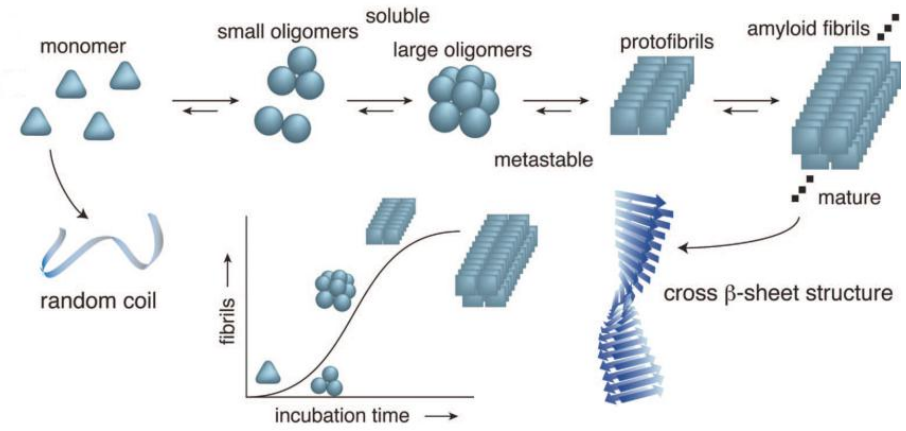

Figure 1.6 – Schematic representation of aS aggregation showing the different on-pathway aggregation products and the sigmoidal lineshape of the kinetic of the process. Adapted from Takahashi and Mihara, 2008, originally depicting amyloid-beta aggregation process.

Measuring the kinetic of aS amyloid formation, we will observe a sigmoidal shape (Figure 1.6): an initial lag phase, that suggested a nucleation mechanism, where oligomers acts as nuclei (Wood *et al*., 1999); a subsequent fast oligomers assembly into higher molecular weight species that lead to a decrease in oligomers concentration and to an increase in fibrillar species concentration; eventually, the process reaches a plateau, i.e. the chemical equilibrium, when mature fibrils are the main polymers in solution. However, the process as described above is an oversimplification, since aS aggregation is likely to be more complex, characterized by different competing pathways (Kaylor *et al*., 2005), leading to multiple forms of aggregation intermediates, oligomers and fibrils.

Several fluorescence spectroscopy techniques allow the quantitative determination of the kinetic properties of aS aggregation *in vitro*. Among those, the most commonly used are Thioflavin T (ThT) binding assay (Levine, 1993) and fluorescence polarization spectroscopy (Luk *et al*., 2007) (see 2.4.1 and 2.4.2). However, several other techniques are available (fluorescence correlation spectroscopy, absorbance measurement, dynamic light scattering) and new methods are applied to this kind of experiments to overcome some of the current limitations (see for example, Nath *et al*., 2010).

These measurements provided information for the comparison of the aggregation kinetic in different conditions that lead to the identification of the main parameters that have proposed to affect aS fibrillization *in vitro*, i.e. protein concentrations, pH values, buffer conditions, temperature and agitation rate and type, solution-air interfaces (Giehm *et al*. 2010).

Considering the importance of the possible relationship between aS pathological mutants aggregation propensity and PD etiopathogenesis, several studies have been performed to unravel this issue. The kinetic parameters of the pathological mutants fibrillization were compared to those of the wild type: A53T presents an increased rate of aggregation and a shorter lag phase, while A30P has a longer lag phase and a lower growth rate, leading to a decrease in the midpoint of the fibrillization transition (Conway *et al*., 1998; Conway *et al*., 2000; Li *et al*., 2001). Also the third mutant E46K shows an increased fibrillization rate, as A53T does, with a double lag phase compared to the wild type (Fredenburg *et al*., 2007).

These results show that the effects that missense mutations have on aS aggregation propensity is not univocal, raising further questions on how mutations affect aS aggregation.

1.2.3.3 Alpha-synuclein oligomeric species

In 2004, Pountney and co-workers were able to purify aS annular oligomers from inclusions in patients affected by MSA (Pountney *et al*., 2004); on-pathway aS oligomeric species were then identified *in vitro* in aggregation assays, but only recently they become more important in PD because they were proposed as the most toxic aggregation intermediate in the aS fibrillization pathway (Winner *et al*., 2011).

Interestingly, Conway and co-workers (Conway *et al*., 2000) observed that both A30P and A53T mutants shared an accelerated oligomerization *in vitro*, but not an accelerated fibrillization, suggesting that an increased fibrillization rate is not directly linked to a higher cytotoxicity in PD. Accordingly, also E46K mutant, which shows also

an increased aggregation rate with respect to wild-type aS, has been shown to form soluble non fibrillar species (Fredenburg *et al*., 2007).

Given these observations, the characterization of these aggregation intermediates acquires more importance, especially if it could lead to the identification of putative toxic mechanism(s) related to these species (discussed in 1.3.2).

Unfortunately, the biophysical characterization of aS oligomeric species is hindered *in vitro* by the fact that they often form a heterogeneous ensemble, constituted by transient species that are difficult to isolate and analyse. Moreover, they seem to be in an unstable equilibrium with aS monomers and to convert to aS monomers, decreasing their detectable fraction, when size-exclusion chromatography is used for their purification (Bhak *et al*., 2009).

The fact that size-exclusion chromatography can decrease the fraction of detectable could explain the differences in the estimated amount of oligomeric species when aS aggregated in solution was analysed by size-exclusion chromatography (about 15% of the total soluble protein) (Lashuel *et al*., 2002) or by Small Angle X-ray Scattering (SAXS) (about 30-40%) (Giehm *et al*., 2011 (b)).

Several groups prepared oligomeric species by mean of different protocols (aS aggregation at 37°C, protein incubating on ice or resuspension after lyophilisation), testing also the aggregation products obtained from the pathological mutants and found a heterogeneous ensemble of oligomers (Figure 1.7) (Lashuel *et al.*, 2002; Giehm *et al.*, 2011 (b); Conway *et al.*, 2000; Kaylor *et al.*, 2005; Fredenburg *et al.*, 2007).

These soluble oligomers and protofibrils showed annular or elliptical shapes, probed by atomic force microscopy and electron microscopy, with diameters going from 4.5 to 55 nm, depending on the technique used for the analysis. The estimation of the average number of aS monomers constituting these oligomers goes from 16 (Giehm *et al.*, 2011 (b)) to more than 42 (Conway *et al.*, 2000; Fredenburg *et al.*, 2007; Lashuel *et al.*, 2002), as well.

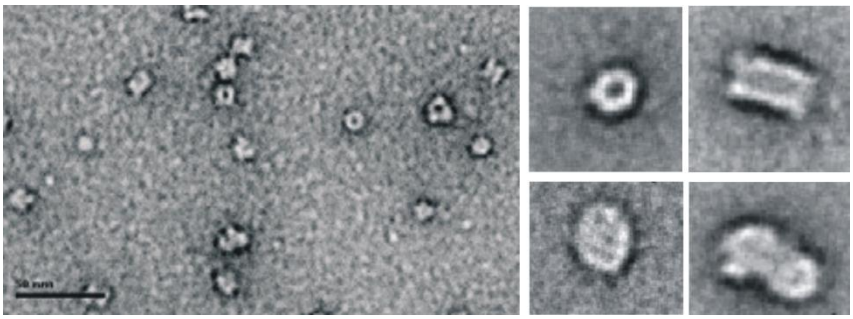

Figure 1.7 – Oligomeric species analysed by transmission electron microscopy (on the left). Scale bar 50 nm. On the right details of the oligomers showing different morphologies and the typical annular structure. Adapted from Lashuel *et al.*, 2002.

More recently, Cremades and co-workers showed by single molecule fluorescence experiments (single molecule two-color coincidence detection -smTCCD) that aS oligomeric species are present as a heterogeneous ensemble during aS aggregation process. Oligomers distribution was divided into three different classes: small (2-5 monomers), medium (5-15 monomers) and large oligomers (15-150 monomers) (Cremades et al., 2012), somehow confirming the variety reported before. Also the mass fraction of soluble oligomers is in quite good agreement with the previous results (less than 5%).

Oligomers secondary structure was characterized by different content of β-sheets probed by Raman spectroscopy (Apetri *et al.*, 2006) and Fourier transform infrared spectroscopy (Kaylor *et al.*, 2005).

As it can be deduced from the various results obtained from the biophysical characterization of aS oligomers, several problems arise in the study of these species *in vitro*. The first problem found is the fact that oligomers structural, morphological and functional characteristics are extremely various and dependent on experimental conditions. The second is that varying the technique used for the analysis induces a great variability in the obtained results. Finally, the fact that these oligomers, mainly obtained *in vitro* using recombinant aS, are not always found in vivo. It is manifest that from the pathological point of view, different oligomeric species acquire importance only when evidences that they are present in PD cell or animal models or in vivo can be provided. For

this reason, the most recent efforts concern mainly their characterization in a more physiological environment (see 1.3.2).

1.2.3.4. Alpha-synuclein amyloid fibrils

aS amyloid fibrils are the end product of aS aggregation and the most characterized being stable in solution and easy to isolate. They share several structural characteristics with amyloid fibrils formed by other amyloidogenic proteins (Dobson, 1999) that are linked to other neurodegenerative disorders, i.e. Alzheimer's disease, Huntington's disease, amyotrophic lateral sclerosis (Ross *et al*., 2005).

A previously mentioned, the first attempt to study aS fibrils structure was performed by X-ray diffraction (Serpell *et al*., 2000), and the data suggested a β-sheet structure for the fibrils, with β-strands perpendicular to the fibril axis.

In the early years of 2000, nuclear and electron resonance techniques were applied to the characterization of aS fibrils structure: the main goal was to define both the structure of the fibril core and of the N-term and C-term to finally develop a complete model for aS amyloid fibrils.

The structural features of aS fibrils were studied by site-direct spin labeling and electronic paramgnetic resonance (EPR) (Der-Sarkissian *et al*., 2003; Chen *et al*., 2007) and solid state nuclear magnetic resonance (ss-NMR) (Heise *et al*., 2005; Vilar *et al*., 2008).

EPR and NMR spectra analysis allowed the determination of the fibrils core region, as well of loops, buried sites and secondary structure elements. Overall, the data suggest that aS fibrils have a β-sheet core region (including not only the NAC domain), not exposed to the solvent and organized in an ordered in-register parallel structure with β-strands planes perpendicular to the fibril axis. 5 or 6 β-strands, turns and loops were identified within this core region, with slight differences for the various reports (Figure 1.8).

The papers propose that N-terminus showed a more heterogeneous and less ordered structure, remaining still quite rigid,

while C-terminus was describe as flexible and completely unfolded. Moreover, Heise *et al.* and Vilar *et al.* identified two different types of fibrils in the sample (Heise *et al*, 2005; Vilar *et al.*, 2008).

In a more recent work (Comellas *et al*., 2011) Comellas *et al*., by assigning via ss-NMR 106 residues *versus* 62 residues presented in a previous assignment (Heise *et al*., 2005), further improved the available set of data on this topic. The novelty of their model is due to the identification of a motif repeated twice in the fibrils secondary structure, constituted by a long β-strand and two short β-strands, which is compared in Figure 1.8 (D) with the other results. In Figure 1.9 aS molecule is represented, as it should be folded within a fibril, following Comellas' model.

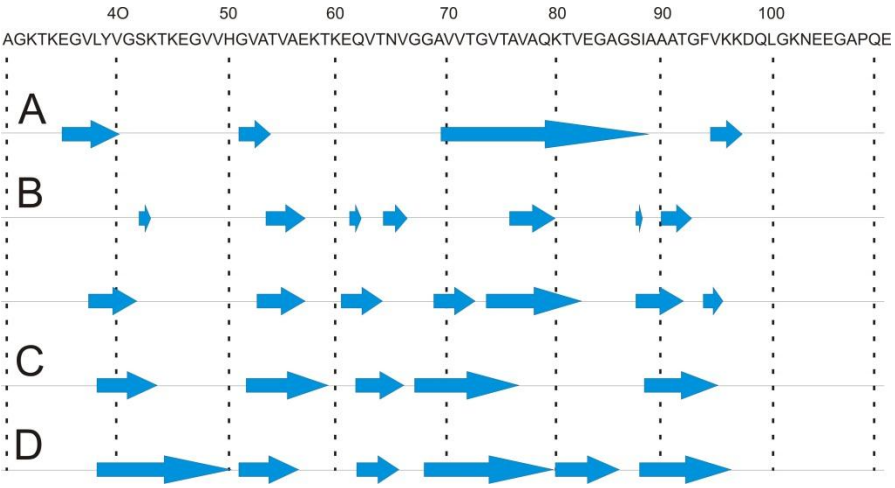

Figure 1.8 – Core region of aS fibrils: amino acidic sequence and β-strands representation for different models (A) β-strands distribution obtained from EPR experiments (Chen *et al.*, 2007). (B) β-strands in two different type of fibrils found aggregating aS and analysing the aggregation products by NMR (Heise et al., 2005). (C) Five β-strands were proposed by Vilar et al., 2008 in a model based on ss-NMR experiments. (D) Most recent β-strands distribution in aS fibrils core regions obtained by ss-NMR assignment (reproposed in an alterantive representation in Figure 1.9) (Comellas *et al.*, 2011).

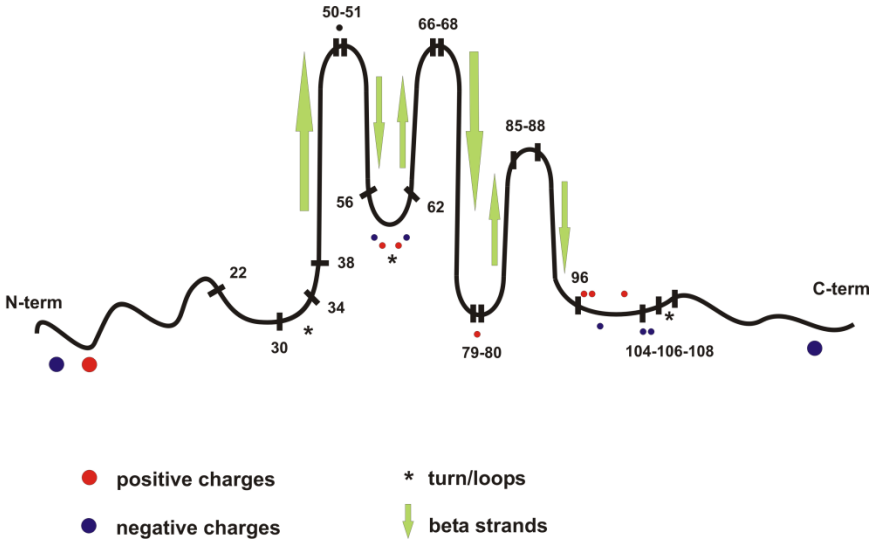

Figure 1.9 – Arrangement of aS molecule in fibrils, following the results obtained by Comellas *et al.*, (2011) by ss-NMR. Free termini are believed to be flexible and responsible for the hierarchical assembly of fibrils discussed further on (Figure 1.10, Khurana *et al.*, 2003). Fibril axis is perpendicular to the plane that contains the folded protein.

Comellas and co-workers could also identify structural features in N- and C- termini, in disagreement with the previous NMR and EPR works.

aS fibrils morphology was probed by transmission electron microscopy (TEM) and atomic force microscopy (AFM). In particular, the latter is suitable to study aS fibrils diameters, periodicity and curvature, while both can be used to measure fibrils length and to qualitatively evaluate their morphology.

Both these imaging techniques allowed the identification of a strong dependence of aS fibrils morphologies, lengths and heights on the experimental conditions, i.e. solution pH, salt concentration, aS concentration (Hoyer *et al.*, 2002; van Raaij *et al.*, 2008), in good agreement with the kinetic and structural data previously discussed. In particular, twisted and untwisted fibrils with different periodicity could be found.

More interestingly, van Raaij and co-workers compared the morphological characteristics of aS, A30P and E46K fibrils measuring heights and periodicities with a robust statistical analysis (van Raaij *et al.*, 2006). They found respectively mean heights of 10.0±1.1 nm,

8.1±1.2 nm and 9.0±0.8 nm for aS, A30P and E46K fibrils, and periodicity of 81±24 nm, 103±20 nm and 76±34 nm.

Khurana *et al*. (Khurana *et al*., 2003) after AFM experiments for the characterization of aS fibrils morphology, proposed a hierarchical assembly mechanism for the fibrils (Figure 1.10): aS monomers, in aggregating conditions, first assembly in protofilaments (3.8±0.6 nm); after protofilaments elongation, two of them intertwine and form protofibrils (mean height 6.5±0.6 nm), probably to minimize the exposure of hydrophobic interfaces. For the same reasons, two protofibrils intertwine into mature fibrils (9.8±1.2 nm).

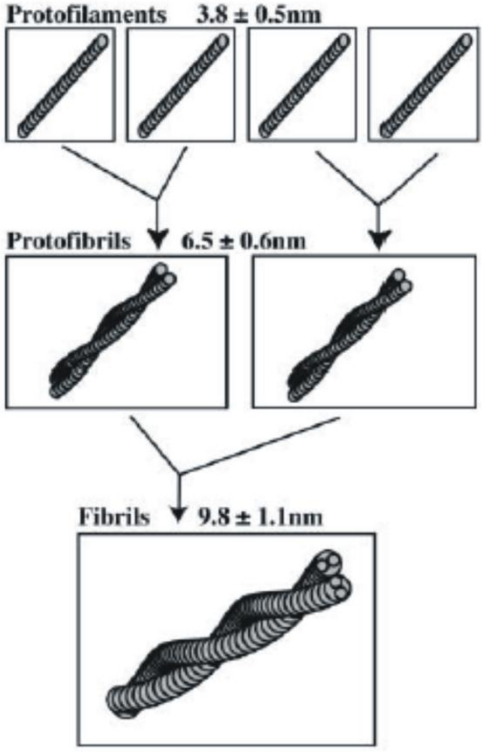

Figure 1.10 – Hierarchical aS fibrils assembly at the latest stages. Protofilaments, protofibrils and fibrils diameters characterized by AFM (Khurana *et al.*, 2003).

Detailed height measurements for aS fibrils and deletion mutants fibrils, lacking N-terminus, C-terminus or both, were performed to determine the role of the two terminals in fibril assembly (Qin *et al*., 2007). The authors showed that the removal of C-terminus leads to the formation of protofibrils, while in the absence of N-term the fibrils structure is conserved, but the mean diameter is smaller because of the

N-terminus removal. The absence of both termini leads to the formation of protofilaments, further highlighting the key role for C- and N-termini in mature fibrils formation.

1.2.3.5 Aggregation inhibitors and enhancers

aS fibrillization can be strongly affected by various factors that can enhance or inhibit aggregation. It has been shown that fibrils elongation rate is directly proportional to protein concentration (Wood *et al*., 1999), which is in good agreement with the fact that *SNCA* gene triplication, responsible for rare and aggressive genetic PD forms, causes an increased dosage of aS (Singleton *et al*., 2003).

Covalent chemical modifications of aS, such as nitration, oxidation and phosphorylation (Serines 87 and 129), lead to variation in the rate and in the final products of the aggregation process (Uversky *et al*., 2002; Yamin *et al*., 2003; Paleologou *et al*., 2010; Paleologou *et al*., 2008).

Divalent and trivalent metal ions (for example, Al^{3+}, Cu^{2+}, Fe^{3+} or Pb^{2+}) (Bisaglia *et al*., 2009) have been shown to strongly accelerate aS aggregation rate *in vitro*. The effect of these compounds suggests a critical role for electrostatic interactions in the aggregation rate modifications.

Other molecules, such as chaperones (Dedmon *et al*., 2005 (b); Luk *et al*., 2008; Ebrahimi-Fakhari *et al*., 2011) or properly designed peptides (El-Agnaf *et al*., 2004; Sievers *et al*., 2011), can slow down or inhibit aS aggregation process, directly interacting with the protein or with other aggregation intermediates.

The study of a family of molecular chaperones, i.e. 14-3-3 proteins, that can interfere with aS aggregation process is part of the research project presented in this thesis and it will be further discussed in this introduction (Section 1.4) and in Chapter 4.

1.3 Alpha-synuclein in cell model for PD

The interest for the study of aS aggregation in cell models is due to the idea of correlating specific aS aggregates to potential toxic effects (Section 1.3.2). This approach seems to be the most promising to find out which are the most toxic species in PD, responsible for neurons death, and which are the related toxic mechanisms. Moreover, recent findings suggest that misfolded aS could be responsible for PD spread in different brain regions, as described by Braak staging (see 1.3.3).

1.3.1 Cell models for the study of alpha-synuclein aggregation

1.3.1.1 Available cell models and methods

Two main approaches were used to study aS oligomerization and/or aggregation and its toxic effects in cell models. One method is based on the transient transfection of aS in cells or on the use of stable cell lines overexpressing aS, which can be used to study early steps of the aggregation process. However, the overexpression does not lead to the formation of large inclusions that resemble LBs; therefore, it can be used only to partially study aS aggregation process in cells (Section 1.3.1.2). To trigger massive aggregation and fibrils formation in cell cytoplasm a second method has to be used. Recombinant aS fibrils fragments, termed seeds (Wood *et al.*, 1999), are introduced in cells during or after aS transfection and lead to the formation of LBs-like inclusions (Luk *et al*., 2009; Danzer *et al.*, 2009; Waxman *et al*., 2010; Nonaka *et al*., 2010). To validate this cell model several imaging experiments were performed days after transfection: cells were fixed and immunostained to detect aS and phosphorilated Ser129 aS (Luk *et al*., 2009; Waxman *et al*., 2010), since the latter has been shown to be present in a large fraction of the aS in LBs (Fujiwara *et al*., 2002).

Nonaka *et al*. performed TEM imaging on cells properly fixed and stained (Nonaka *et al*., 2010). Since TEM microscopy resolution is higher than fluorescence confocal microscopy one (about 0.2-2 nm *versus* 200-300 nm), they were able to identify aS amyloid fibrils in cell

cytoplasm, further validating the model. The presence of β-sheet forms of aS was confirmed also by Thioflavin S measurements (Luk *et al*., 2009).

Besides conventional fluorescence imaging assays, performed on cells by staining or immune-staining after fixation, confocal microscopy imaging and advanced microscopy techniques, i.e. Förster resonance energy transfer (FRET), fluorescence lifetime imaging (FLIM) and fast recovery after photo-bleaching (FRAP) were used for a more in depth study of aS aggregation in live cells.

To make aS detectable in live cells, the protein was fused with a fluorescent protein or with a tag composed by four cysteines (C4 tag) inserted in a 12-mer peptide (FLNCCPGCCMEP). Biarsenical compounds (FlAsH and ReAsH) can be used to stain the protein in the cytoplasm of live cells: they covalently bind C4 tag and can stain the protein directly in the cytoplasm of live cells after permeating cells membrane (Roberti *et al*., 2008). Since the C4 tag plus the biarsenical dye have jointly a molecular weight of about 1.3 kDa, it is more likely that they cannot seriously affect aS aggregation process. However, some drawbacks were shown: FlAsH reagent can bind also to proteins that are rich in cysteines, at least in some cell lines, and the staining is typically less efficient than the conventional methods of staining (Stroffekova *et al*., 2001; Hearps *et al.*, 2007).

On the contrary, fluorescent proteins are stable highly specific bright molecules, but large and folded (EGFP molecular weight is about 28 kDa, compared to the 14.6 kDa aS): for this reason they could affect aS behaviour and aggregation in cells. In the past years, certain results threw doubts about this issue (McLean *et al.*, 2001), but more recent data suggest that; aS fused with EGFP or YPF show similar aggregation products and kinetics in vitro (van Ham *et al.*, 2010) and are suitable for the study of aS aggregation in live cells (Nath *et al.*, 2011).

1.3.1.2 Advanced fluorescence microscopy methods

Biomolecular fluorescence complementation (BiFC) allowed Outeiro and co-workers to visualize aS dimers and oligomers in living cells (Outeiro *et al*. 2008 *Plos One*). The technique is based on the generation of BiFC aS mutants, where aS is fused with GFP fragments that become fluorescent only when aS molecules associate. The authors also demonstrated that these low molecular weight species are essential steps for the formation of larger aggregates and are the cause of cytotoxicity.

aS fused with a C4 tag was overexpressed in SH-SY5Y and staining was performed with both FlAsh and ReAsH, whose emission spectra partially overlap and allowed FRET imaging (Roberti *et al*., 2008). Images by confocal microscopy were acquired every 24 hours for 3 days and FRET analysis was performed. FRET intensity distribution defined two different ensembles, one characterized by FRET energies between 60% and 80% representing aS aggregates, while the second, with energies between 30% and 45%, corresponding to the non-aggregated form of the protein.

The same authors further investigated aS aggregation in living cells by FRAP and confocal fluorescence anisotropy (CFA) (Roberti *et al*., 2011).

FRAP data provide information on protein mobile fraction and diffusion coefficient D, while CFA evaluates the changes in size of aS molecules. In SHSY5Y cells transfected with aS and stained with ReAsH, several structures were identified based on the FRAP and CFA information: free protein (D=10 $\mu m^2/s$); membrane bound protein or small aggregates and large aggregates.

FRET measurements were further used to study aS conversion into aggregates in cells through the development of a FRET sensor. Since aS develops an intrinsic fluorescence emission during the aggregation process, Schierle-Kaminski *et al*. fused aS with a yellow fluorescent protein (aS-YFP) and measured FLIM-FRET occurring between the growing oligomers and the YFP (Schierle-Kaminski *et al*.,

2011). aS-YFP was introduced in SH-SY5Y cells through electroporation and measurements of the excited state lifetime allowed to monitor FRET pixel by pixel. The average lifetime is about 2970±70 ps for cytoplasmic homogeneous protein at the beginning of the process and becomes 1480±40 ps after 4 days.

In this thesis other advanced microscopy techniques, described in chapter 2, were used to characterize aS oligomerization and aggregation in live cells, adding further pieces to the aS aggregation puzzle in live cells.

1.3.2 Alpha-synuclein toxic mechanisms

Several toxic mechanisms have been related to aS aggregation process and aS oligomeric species and fibrils. Given the heterogeneity of the aggregation products, it is reasonable to suppose that cytotoxicity can be exerted in different ways.

Among the most studied noxious effects ascribed to aS is the ability of monomeric or oligomeric aS of interacting in a disrupting way with lipid membranes (Reynolds *et al.*, 2011) or to form well characterized pores that are similar to the one formed by the pore-forming toxins and could exert a pathological effect (Zakharov *et al.*, 2007; Tosatto *et al.*, 2012; Kim *et al.*, 2009). Membrane destabilization or disruption and pores formation can cause membrane damages, calcium leakage and transmembrane potential dissipation (see Butterfield and Lashuel, 2010 for a wide review).

To prove if the effects mentioned above are also present in aS cell models, aS was overexpressed in dopaminergic doxycycline-treated cells, aS aggregates were identified in cells, localized at the cell membranes by fluorescence microscopy and conductance variations were revealed (Feng *et al.*, 2010). The increased of membrane currents upon voltage application was found independently also in HEK293 overexpressing aS (Tsigelny et *al.*, 2007).

If aS oligomers induce plasma membrane destabilization, they could also damage intracellular membranes, i.e. vesicles containing neurotransmitters (Mosharov *et al.*, 2006) and mitochondrial membranes.

The latter are very likely to be damage because of the indirect proof of mitochondrial fission and variation in mitochondrial morphology induced by aS overexpression in HeLa cells (Nakamura *et al.*, 2011). The authors could not verify that the mitochondrial associated aS was in an oligomeric form in cells, but were able to demonstrate aS oligomers interaction with mitochondrial-like membranes *in vitro*. Furthermore, aS overexpression in PC12 lead to mitochondrial depolarization, mitochondrial-mediated cell death (Smith *et al.*, 2005; Tanaka *et al.*, 2001) that could induce ROS production.

However, not only membranes but also other cellular structures are affected by the presence of aS or its pathological mutants or its aggregated forms. aS overexpression in PC12 cells was shown to induce endoplasmatic reticulum (ER) stress (Smith *et al.*, 2005) and Golgi fragmentation was seen in COS-7 presenting aS aggregates (Gosavi *et al.*, 2002). The idea of ER stress induced by aS was further confirmed by the finding of aS oligomers within ER in a in vivo mice model for PD (Colla *et al.*, 2012)

Both ubiquitin-proteasome system and autophagic lysosomal pathway were shown to be involved in the clearance of monomeric, oligomeric or aggregated aS. Moreover, clearance mechanisms were impaired in some cell and animal models for aS aggregation, probably because of the presence of an excessive amount of misfolded protein. The literature on these aspects is wide and sometimes controversial: for a complete review see Ebrahimi-Fakhari *et al.*, 2012.

Indirectly, as it was shown for amyloid forming chimeric proteins in a recent paper (Olzscha *et al.*, 2012), aS could induce severe disequilibrium in proteins homeostasis sequestrating essential proteins during the aggregation process in cell. Molecular crowding induced by aS aggregates and aS ability of co-aggregating with other proteins or chaperones (Xu *et al.*, 2002; Dedmon et al., 2005), as far as the findings, by co-localization and proteomics studies, of several proteins in LBs (Shirakashi *et al.*, 2006; Xia *et al.*, 2008), further support this hypothesis.

Finally, it has been shown that neuroinflammation mechanisms (reviewed in Maguire-Zeiss and Federoff, 2010) and oxidative stress

(Cremades *et al.*, 2012) can be induced by the presence of aS oligomers and fibrils.

Figure 1.11 summarizes the most important toxic mechanisms related to aS aggregation in cells. What remains unclear in the PD etiopathogenesis is when aS oligomerization or aggregation is the cause of the toxicity and when it is the results of previous pathological conditions that affect aS normal functionality and induce aS aggregation.

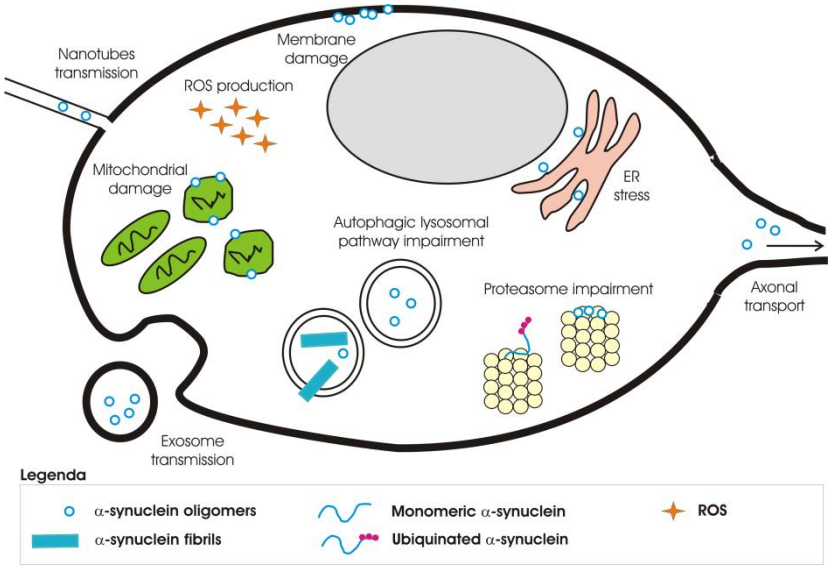

Figure 1.11 – Summary of the main proposed toxic mechanisms related to aS aggregation and transmission: membrane damages, mitochondrial dysfunction, clearance mechanisms impairment, ER stress and ROS production. Among the aS aggregates transmission mechanism (detailed at section 1.3.3): exosome transmission, axonal transport and nanotubes transport.

1.3.3 PD propagation through misfolded alpha-synuclein

Braak staging for PD states that LBs first appear in the olfactory bulb and that only later in the disease evolution LBs emerge in other brain regions (Braak *et al.*, 2003). This suggests that the transmission of misfolded or aggregated aS from unhealthy to healthy neurons could be responsible for the spread of the pathology and the disease progression.

This hypothesis was further supported on the basis of clinical evidences (Kordower *et al.*, 2008; Li *et al.*, 2008), showing the presence of LBs in neurons grafted in parkinsonians brains 10 years after surgery.

These results drove the first studies in cellular models to verify the cell-to-cell transmission of oligomeric aS via endocytosis, which gave positive results (Desplats *et al.*, 2009; Hansen *et al.*, 2011). The transmitted aggregates work as seeds and trigger aS aggregation process in the recipient cells. The same mechanism was exploited in the LBs-like cell models where aS seeds were untaken by cells and start inclusions formation (Nonaka *et al.*, 2010).

These first finding lead to more detailed studies on aS aggregates transmission among neurons: Volpicelli-Daley and co-workers showed that preformed recombinant aS fibrils were uptaken by mice primary cultured neurons (Volpicelli-Daley *et al.*, 2011). These fibrils affected neurons excitability and connectivity and caused cell death. Moreover, they could show that there was intracellular fibrils propagation, due to the movement of fibrils from neurons soma to the neurites and vice-versa. In vivo preformed fibrils propagation was recently documented by the same group: transmission from neuron to neuron in non-transgenic mice brain after fibrils injection cause the spreading of PD pathology in mice, which start to show the typical PD symptoms (Luk *et al*., 2012).

The precise mechanism(s) that cause aS spread from neuron to neuron or aS uptake from the extracellular space are not clear and some hypotheses have been proposed: (i) direct cell-to-cell transfer due to the increased protein concentration in the extracellular space caused by cell lysis; (ii) exosomes or vesicles can protect the misfolded protein from the proteolitic enzymes and carry it to recipient cells; (iii) molecular chaperones can mediate aS transmission; (iv) misfolded aS could move through the slow movement of axonal transport; (v) membrane nanotubes interconnecting cells over long distances can be an highway for aS aggregates (Steiner *et al.*, 2011).

A couple of hints about the possible mechanism came from two recent papers: the first one propose that overexpressed aS can be transmitted from transfected SH-SY5Y cells to normal SH-SY5Y cells by exosomes (Alvarez-Erviti *et al.*, 2011). The second, showed how fibrillar aS was transferd along axons trough anterograde axonal transport, without the

requirement of a synaptic contact between soma and axons (Freundt *et al.*, 2012).

Among the remaining mechanisms, tunnelling nanotubes, which allow the movement of molecules and of cytoplasmic content (Sherer and Mothes, 2008) seems promising, given its involvement in prion protein transfer (Gousset et *al.*, 2009).

1.4 14-3-3 proteins

The scientific community is showing a growing interest in molecular chaperones in the frame of PD studies: indeed, molecular chaperones can assist protein folding and modulate protein-degradation pathways (Ebrahimi-Fakhari *et al.*, 2011), which are some of the mechanisms impaired in the pathogenesis of PD. Moreover, several *in vitro* studies showed that some molecular chaperones or chaperone-like proteins can interfere with aS aggregation process (Dedmon *et al.*, 2005; Luk *et al.*, 2008). This evidence could be the basis of the therapeutic potential of these proteins, which can prevent protein misfolding and aggregation, but the results presented in the literature are not conclusive and need to be further consolidated.

In this frame a family of chaperone-like proteins, 14-3-3 proteins, gained relevance in the recent years.

1.4.1 14-3-3 proteins structure and function

14-3-3 proteins are a family of highly conserved acidic proteins, expressed in the cytoplasm of all eukaryotic cells and represent about 1% of the total soluble brain proteins. In humans there are seven 14-3-3 isoforms: β/α, γ, ε, ζ/δ, η, σ, and τ, where α and δ are the phosphorylated form of β and ζ, respectively (Aitken, 2006), associated to a wide range of functions, that includes signalling, cell cycle control, apoptosis, exocytosis, cytoskeletal rearrangements, transcription and enzyme activity (Berg *et al.*, 2003).

The different 14-3-3 proteins form both hetero-dimers and homo-dimers (Figure 1.12, panel A), with different propensities depending on the isoform, but β and η were found also as monomers (Yang *et al.*, 2006).

The proteins show a high sequence identity and the X-ray crystallographic structure is available for all the isoforms: each monomer in a 14-3-3 dimer is constituted by nine antiparallel alpha-helices (termed from αA to αI) (Gardino *et al.*, 2006).

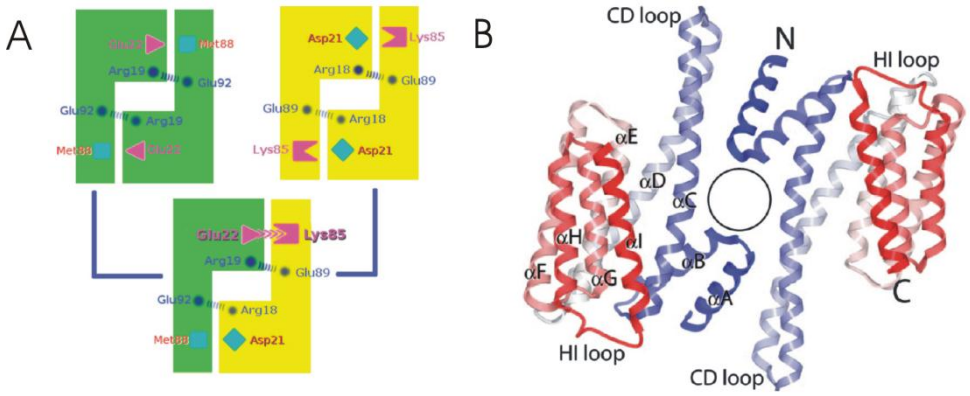

Figure 1.12 – 14-3-3 proteins dimerization: hetero- or homo- dimers formation (panel A) with the residues involved in the hydrogen bond formation highlighted. Secondary structure of 14-3-3 proteins with helices and loops properly termed and the groove represented with a circle (Yang *et al.*, 2006).

The first four helices form the dimer interface, while αC, αE, αG and αI form a peptide-binding groove constituted by a hydrophobic patch and a positively charged patch (Figure 1.12, panel B) (Yang *et al.*, 2006).

The most relevant variation among the different isoforms from the structural point of view seems to lie within the loop regions (in particular αC-αD loop) and along the C and D helices (Figure 1.13) (Gardino *et al.*, 2006). These features may account for the specificity in the interaction with their binding partners.

Actually, 14-3-3 proteins are able to associate with over 100 binding partners and, as mentioned before, are involved in the regulation of a wide range of cellular processes (Bustos and Inglesios, 2006).

The main structural feature of 14-3-3 proteins molecular recognition is a phosphorylated motif in the binding partners that defines this family of proteins as phosphoserine/threonine binding molecules (Yang *et al.*, 2006). In addition, there are other reports that identified interactions between 14-3-3 proteins and the C-terminus of target binding partners (Shikano *et al.*, 2006).

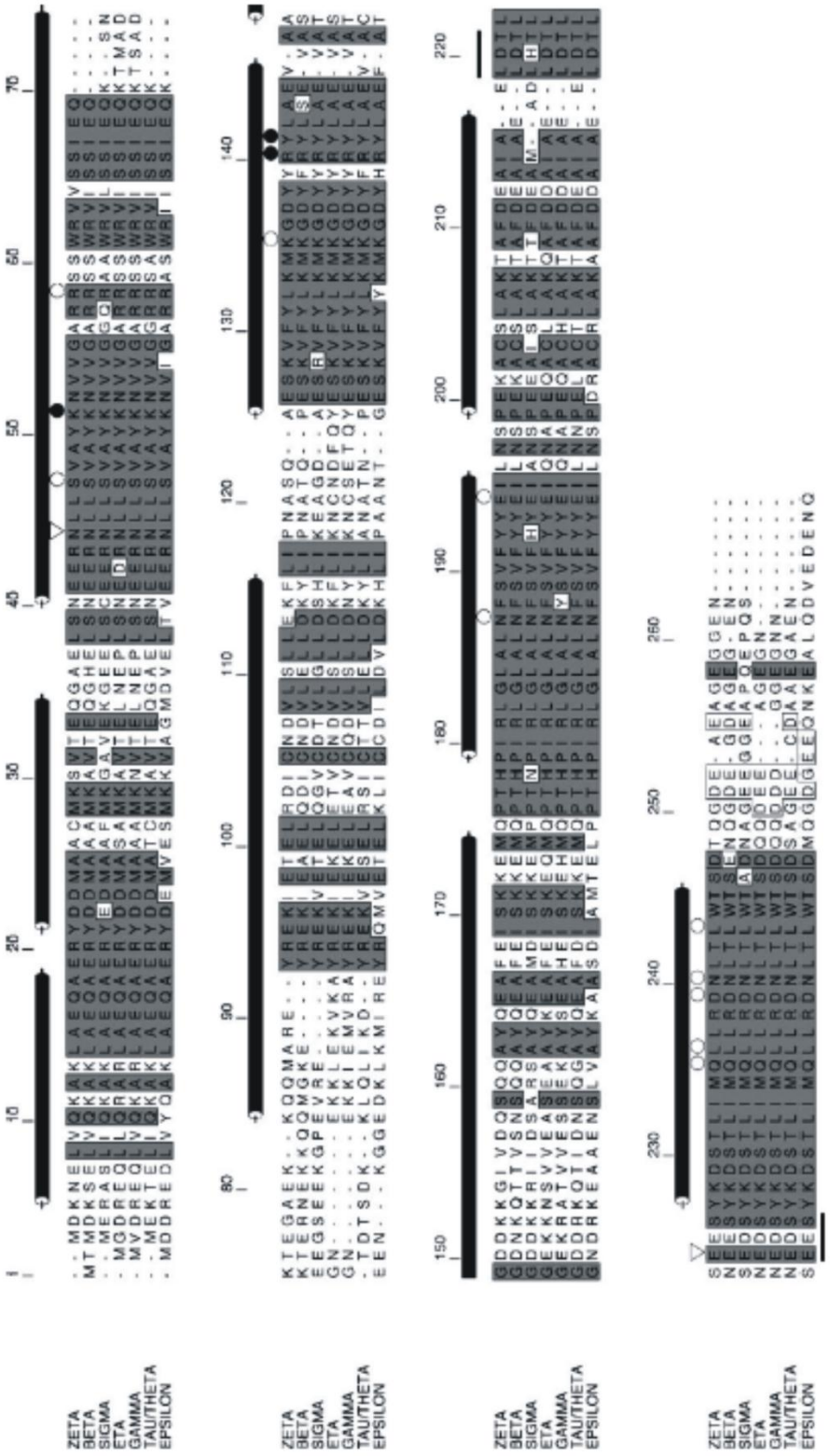

Figure 1.13 – Structure-based sequence alignment of human 14-3-3 proteins (Gardino et al., 2006).

Different mechanisms of action have been proposed to account for 14-3-3 ability to modulate so many different cellular processes: (i) 14-3-3 proteins can induce conformational changes of the target protein; (ii) they can physically hinder access to specific structural features; (iii) they work as scaffolding protein and (iv) help moving the binding proteins (Bridges and Moorhead, 2005).

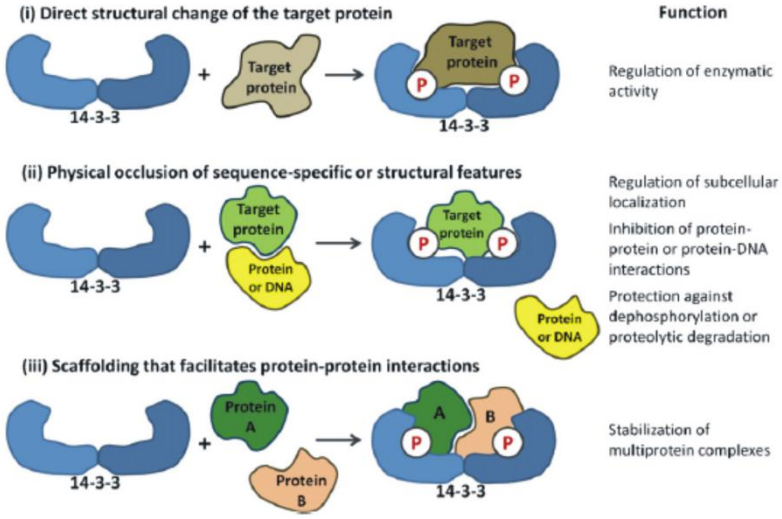

Figure 1.14 – Mechanisms of action of 14-3-3 proteins and related possible function (Obsil *et al.*, 2011).

Interestingly, the rationale for the presence of different isoforms in 14-3-3 protein family is still object of debate: it is still unclear whether they have distinct and specialized functions or whether they are just under the control of temporal and tissue specific regulation (van Hemert *et al.*, 2004). Baxter *et al.*, (2002) reported an isoform-specific characterization of 14-3-3 proteins distribution in murine brains, providing some hints on the importance of the heterogeneous pattern of localization in different brain regions.

1.4.2 14-3-3 chaperone-like proteins and PD

14-3-3 proteins were shown to be present in the cerebrospinal fluid and in some disease-specific lesions and protein inclusions in brains, suggesting a possible involvement of these proteins in the pathogenesis of neurodegenerative disorders, such a Creutzfeld-Jakob disease, Alzheimer's

disease, polyglutamine diseases, amyotrophic lateral sclerosis, Parkinson's disease and LBs diseases (Berg *et al.*, 2003; Steinacker *et al.*, 2011). Interestingly, strong evidence, emerging from clinical and basic studies, suggests a role for 14-3-3 proteins also in neurodevelopmental disorders and neuropsychiatric disorders (Foote and Zhou, 2012).

A first potential association of 14-3-3 proteins to PD was suggested by the association of a significant portion of 14-3-3 proteins bound to synaptic membranes: ε, η, γ, β and ζ are all found in purified synaptic membranes, but not to mitochondrial and myelin membranes (Martin *et al.*, 1994). One of the isoforms (14-3-3 ζ) was found to activate tyrosine hydroxylase, which is the rate limiting factor of dopamine synthesis in dopaminergic neurons that are the most affected by PD (Wang *et al.*, 2009)

Moreover, 14-3-3 proteins were found in LBs in parkinsonian brains (Kawamoto *et al.*, 2002; Berg *et al.*, 2003; Umahara *et al.*, 2012).

But the actual link between this family of chaperone-like proteins and PD comes from their ability to interact with a subset of the PD related proteins, i.e. LRKK2, parkin and aS.

LRRK2 is a large multidomain protein member of Roco protein family with kinase and GTPase activity. It has been shown that 14-3-3 proteins have a regulatory effect on its function: LRRK2 pathological mutants showed a decreased phosphorylation of two serines, which prevents 14-3-3 binding and results in subcellular redistribution of LRRK2 and neurodegeneration (Dzamko *et al.*, 2010; Nichols *et al.*, 2010). The two isoforms most involved in this process seems to be η and γ (Li *et al.*, 2011).

Parkin is an ubiquitine ligase protein that is important for degradation pathway that is negatively regulated by 14-3-3 η (Sato *et al.*, 2006).

More relevantly, to the work that will be presented here, it has been shown that 14-3-3 proteins are strongly related to aS, as it will be discussed later on (Section 1.4.3).

Finally, Yacoubian and co-workers observed differential neuroprotective effects of the various isoforms of 14-3-3 in dopaminergic

cell models for PD where toxicity was induced by MPP+ and rotenone (Yacoubian *et al.*, 2010; Slone *et al.*, 2011).

1.4.3 Alpha-synuclein and 14-3-3 proteins

The main association between PD and 14-3-3 proteins family implies aS protein and aggregation. As mentioned before, 14-3-3 proteins were immunohistochemically detected in LBs in human PD: older reports suggest that only ζ, τ, ε and γ isoforms are present in the inclusions (Berg *et al.*, 2003), while citing preliminary results still not published but anticipated in a review Umahara and co-workers propose that all the isoforms are in LBs, but the staining can have different intensity (Umahara *et al.*, 2012).

14-3-3 proteins were also found co-localized with aS in A53T transgenic mice, with different distributions in brain regions (Shirakashi *et al.*, 2006).

Ostrerova *et al.*, (1999) found that regions of aS and 14-3-3 shared sequence homology: two regions were seen between amino acid 8 and 61 in aS that share respectively 43% and 36% of sequence homology with regions going from amino acid 45 to 102 in 14-3-3 proteins. This region in 14-3-3 is involved in dimerization; therefore, the authors propose that the two proteins can interact. Co-immunoprecipitation of aS and 14-3-3 (β and ε isoforms) from rat brain homogenate showed that the two proteins can be associated in both cytosolic and membrane fractions. Soluble aS and 14-3-3 complexes (about 54-83 kDa) were also found in human primary neurons cell culture after aS overexpression (Xu *et al.*, 2002).

Moreover, aS and the isoform η are co-immunoprecipitated from the *substantia nigra* of PD patients (Sato *et al.*, 2006). Interestingly they could also show how aS is able to sequester 14-3-3 η from parkin-14-3-3 η complex, interfering with the regulation of parkin by the chaperone. Since the *in vitro* interaction between recombinant aS and isoform η could not be proved, Sato *et al.*, (2006) suggested that an alternative interaction pathway mediated by aS modification could exist.

Very interestingly, it was also shown that 14-3-3 η and ε expression is upregulated in A53T transgenic mice, while γ is downregulated and the other isoforms expression was unchanged (Kurz et *al.*, 2011). In another report τ, ε and γ isoforms were the found to be downregulated in transgenic aS mice models (Yacoubian *et al.*, 2010). However, these variations in 14-3-3 expressions in PD models further link this family of molecular chaperons to PD.

Although the rational for the presence of differential 14-3-3 proteins is still not clear, it is plausible that different isoforms could bind different ligands mediating the effects described above via independent pathways.

1.5 Aim of the project

The research project proposed in this thesis can be divided into two different parts: the first one is releting to the study of aS aggregation in cell models, while the second one is related to the study of 14-3-3 proteins effects on aS aggregation *in vitro* and in the same cell models.

The need of a more detailed characterization of aS aggregation in cells is particularly relevant for the first steps of the process: for this reason we applied advanced fluorescence microscopy techniques, i.e. Number and Brightness method and NADH fluorescence lifetime imaging and spectral imaging, to study aS oligomerization and fibrils formation in live cells.

It is clear from the literature that 14-3-3 proteins can be strongly linked to PD and PD related proteins: in particular, 14-3-3 η seemed the most promising among the 14-3-3 isoforms in term of aS interaction capability.

The reported interaction in cells and parkinsonian brains between aS and 14-3-3 η does not occur for recombinant proteins, suggesting that a modification to the proteins is needed for the binding. The interaction between the two proteins was studied during aS aggregation process *in vitro* and in a cellular environment. Moreover, rescue effects due to 14-3-3 η overexpression in aS aggregation cell models were studied, in order to obtain a deeper understanding of the involvement of this chaperone in PD molecular mechanism(s) related to aS.

Chapter 2

Materials and Methods

"Twenty years from now you will be more disappointed by the things that you didn't do than by the ones you did do. So throw off the bowlines. Sail away from the safe harbor. Catch the trade winds in your sails."

Mark Twain

2.1 Materials

2.1.1 Growth media

Luria Bertani (LB): 0.5% w/v yeast extract, 1% w/v Bacto Triptone, 8.56 mM NaCl, 0.1% NaOH 1N

LB-agar: 0.5% w/v yeast extract, 1% w/v Bacto Triptone, 8.56 mM NaCl, 0.1% NaOH 1N**,** 1.5% w/v agar

SOC: 0.5% w/v yeast extract, 2% w/v Bacto Triptone, 8.56 mM NaCl, 2.5 mM KCl, 10 mM $MgCl_2$, 20 mM glucose

HEK293 medium: DMEM (Dulbecco's Modified Eagle Medium, High Glucose, GlutMAZ, Pyurvate - Gibco -), 10% v/v Fetal Bovine Serum (FBS – Gibco -), 50 U/ml penicillin, 50 μg/ml streptomycin

SH-SY5Y medium: 50% DMEM (Dulbecco's Modified Eagle Medium, High Glucose, GlutMAZ, Pyurvate - Gibco -), 50% F12 (Nutrient Mixture F-12 – Gibco -) 10% v/v FBS, 50 U/ml penicillin, 50 μg/ml streptomycin

2.1.2 Solutions and reagents

PBS: 137 mM NaCl, 2.7 mM KCl, 4.3 mM Na_2HPO_4, 1.47 mM KH_2PO_4, pH 7.0

Osmotic shock buffer: 30 mM Tris, 2 mM EDTA, 40% sucrose

TBI: rubidium chloride 100 mM, manganese chloride 50 mM, potassium acetate 30 mM, calcium chloride 10 mM and glycerol 15% v/v, pH 5.8 adjusted with 0.2 M acetic acid, filtered 0.45 μm

TBII: calcium chloride 75 mM, rubidium chloride 10 mM, MOPS 10 mM, glycerol 15% v/, pH 6.5 adjusted with KOH, filtered 0.45 μm

Stacking gel (4%): acrylamide solution 4%, Tris-HCl 0.125 mM pH 6.8, SDS 0.1%, APS 0.1%, TEMED 0.1% (acrylamide solution is constituted by acrylamide: bis acrylamide ratio equal to 29:1)

Resolving gel (13%): acrylamide solution 13%, Tris-HCl 0.375 mM pH 8.8, SDS 0.1%, APS 0.1%, TEMED 0.008%

Running buffer: Tris-HCl 25 mM, glycine192 mM, SDS 0.1%, pH 8.3

Coomassie solution: Coomassie Brillant Blue R250 0.25% (w/v), ethanol 45 % (v/v), acetic acid 10% (v/v)

Destaining solution: isopropanol 10% v/v, acetic acid 10% v/v

Laemmli loading buffer 4X: Tris-HCl 50 mM pH 6.8, SDS 2%, DTT 100 mM, bromophenol blue 0.1%, glycerol 10%

Transfer buffer: 25 mM Tris-HCl, 192 mM glycine, 10% v/v methanol

Lysis buffer: 20 mM Tris-HCl pH 7.5, 150 mM NaCl, 1 mM EDTA, 1% v/v Triton X-100, 2.5 mM Na-pyrophosphate, 1 mM β-glycerophosphate, 1 mM $NaVO_4$

TTBS buffer: 50 mM Tris-HCl, 150 mM NaCl, 0.1% v/v Tween

2.1.3 Antibodies

Anti aS: mouse monoclonal antibody, detects aS, epitope maps at aS NTD (Syn204, Cell Signaling); WB dilution 1:2000, ICC dilution 1:100.

Anti 14-3-3 PAN: rabbit polyclonal antibody, detects all 14-3-3 isoforms (sc-692, Santa Cruz Biotechnology, Inc.); WB dilution 1:1000, ICC dilution 1:100

Anti 14-3-3η: rabbit polyclonal antibody against a region between amino acids 71-120 of human 14-3-3 η (ab28665, ABCAM); immuno-TEM dilution 1:100

Anti 14-3-3η: goat polyclonal antibody against a peptide mapping near the C-terminus of human 14-3-3η (sc-17287, Santa Cruz Biotechnology, Inc.); WB dilution 1:200

Anti β-galactosidase (LacZ): rabbit antibody against the enzyme β-galactosidase (A11132, Invitrogen); WB diluition 1:1000

Anti GADPH: mouse monoclonal antibody, detects Glyceraldehyde 3-phosphate dehydrogenase (GADPH) (MAB374, Millipore); WB dilution 1:2000

Anti-mouse + HRP: goat antibody conjugated with HRP, detects mouse IgG (A4416, Sigma); WB dilution 1:2000

Anti-rabbit + HRP: goat polyclonal antibody conjugated with HRP, detects rabbit IgG (DC03L – Mercl4Bioscience); WB dilution 1:16000

Anti-goat + HRP: rabbit polyclonal antibody conjugated with HRP, detects goat IgG (A5420, Sigma); WB dilution 1:7500

Anti-mouse + Alexa Fluor 488: goat antibody conjugated with AlexaFluor488, detects mouse IgG (A11029, Invitrogen); ICC dilution 1:100

Anti-rabbit + Alexa Fluor 568: goat antibody conjugated with AlexaFluor568, detects rabbit IgG (A11031, Invitrogen); ICC dilution 1:100

Anti-rabbit + 10 nm gold nanoparticles: goat antibody conjugated with 10 nm gold nanoparticles, detects rabbit IgG (G7402, Sigma); immune-TEM dilution 1:30

2.1.4 Optical microscopes

Widefield fluorescence microscope: Leica DM 5000B

Widefield fluorescence inverted microscope: Leica DMI 4000B

Cofocal microscope: Nikon Eclipse E6000

(at the Department of Biology, University of Padova, Italy)

Confocal microscope: Olympus FluoView1000 confocal laser scanning microscope, using an UPLSAPO 60 × water 1.2 NA objective

Multiphoton confocal microscope: Zeiss 710 confocal laser scanning microscope, coupled with a Ti:Sapphire laser (Spectra-Physics Mai Tai) and an ISS A320 FastFLIM

(at the Laboratory for Fluorescence Dynamics, University of California, Irvine - USA -)

2.2 Molecular biology

2.2.1 Plasmids for protein expression in mammalian cells

Protein	Plasmid	Resistance	Tag	Comments
14-3-3 proteins	pEBG-6P1	Ampicillin	GST-tag at C-terminus	Gift from Dr. D. Alessi (Univ. of Dundee, Scotland)
14-3-3η	pdsRED (Clonetech)	Ampicillin	Monomeric dsRED at C-terminus	Cloned in the lab
aS	pCDNA (Invitrogen)	Ampicillin	-	Previously available in the lab
aS	pEGFP-N1 (Clonetech)	Kanamicin	EGFP tag at C-terminus	Cloned in the lab

2.2.2 Plasmids for recombinant protein expression

Protein	Plasmid	Resistance	Tag	Comments
14-3-3η/γ	pQE50 (Qiagen)	Ampicillin	His-tag at C-terminus	Gift from Prof. H. L. Monaco (Univ. of Verona, Italy)

14-3-3 proteins	pET-28a+ (Novagen)	Kanamicin	-	Cloned in the lab
Wild type aS/C141 mutant	pET-28a+ (Novagen)	Kanamicin	-	Previously available in the lab

2.2.3 Competent cells

2.2.3.1 DH5α rubidium chloride competent cells

A single colony of DH5α *E. coli* strain was inoculated in 100 ml of LB broth. Cells were grown at 37 °C to an OD_{600nm} between 0.22 and 0.50. Cells were then chilled on ice for 20 minutes and pelleted at 4°C. The pellet was resuspended in 20 ml of pre-chilled TBI (see 2.1 Materials) and kept on ice for 5 minutes. Cells were centrifuged again, pellet resuspended in 2 ml of pre-chilled TBII and incubated 15 minutes in wet ice. Cells were aliquoted into microcentrifuge tubes, frozen in liquid nitrogen and stored at -80°C.

2.2.3.2 BL21(DE3) calcium chloride competent cells

A single colony was inoculated in 5 ml LB culture and cells were grown overnight at 37°C. The culture was re-inoculated in 100 ml of fresh media and grown at 37°C to an OD_{600nm} of 0.3. The culture was cooled in ice for 15 minutes. From this point, the protocol has to be carried out at 4°C and pre-chill buffers are needed.

Cells were harvested by centrifugation and pellet resuspended in ½ of initial volume with calcium chloride 0.1 M (typically 50ml) and kept in ice for 30 minutes. Cells were centrifuged again and the pellet was resuspended in a calcium chloride 0.1M and 25% glycerol solution in 1/50 of the initial volume. The competence starts after 1 hour of ice

incubation and increases with time until 24 hours. After 24 hours cells are stored at -80°C.

2.2.4 DH5α and BL21(DE3) cells transformation

Aliquots of 100 μl of competent cells were thawed on ice and transformed with about 50 ng of plasmidic DNA. Briefly, after plasmidic DNA addition cells were left in ice for 20 minutes and then subjected to heat shock at 42°C for 90 seconds.

Trasformed cells were then grown for 45 minutes at 37°C in SOC media. Finally, bacteria were plated on LB-agar petri dishes supplemented with the appropriate antibiotic for selection.

2.2.5 Plasmidic DNA purification

A single colony of DH5α transformed with the desired plasmid was grown overnight at 37°C in an appropriate volume (5 ml for mini-prep or 200 ml for maxi-prep) of LB media supplemented with 50 μg/ml ampicillin or 25 μg/ml kanamycin.

Bacteria were then pelleted and plasmidic DNA purification was performed using QIAprep Spin Kit (Qiagen) for mini-prep or PureLink HiPure Plasmid Filter Maxiprep Kit (Invitrogen), following the manufacturer instructions.

2.3 Biochemical methods

2.3.1 Recombinant alpha-synuclein expression and purification

WT aS and the C141 mutant were expressed in *E. coli* BL21(DE3) strain and grown to an OD_{600nm} of 0.3-0.4 and induced with 0.1 mM IPTG. After 5 hours, cells were collected by centrifugation and recombinant proteins recovered from the periplasm by osmotic shock using an osmotic shock buffer (Huang *et al.*, 2005). Subsequently, the periplasmic homogenate was boiled for 15 minutes and the soluble aS-containing fraction was subjected to a two-step (35% and 55%) ammonium sulphate precipitation. The pellet was resuspended, extensively dialyzed against 20 mM Tris-HCl pH 8.0, loaded into a 6 ml Resource Q column (Amersham Biosciences) and eluted with a 0-500 mM gradient of NaCl. Proteins were then dialyzed against water, lyophilized and stored at -20 °C.

aS purity and integrity after purification was checked by SDS-PAGE and reverse phase HPLC chromatography.

2.3.2 Recombinant 14-3-3 proteins expression and purification

14-3-3 proteins were expressed in *E. coli* in BL21(DE3) strains. Bacteria were grown at 37°C to an OD_{600nm} of 0.7-0.8, then induced with 0.5 mM IPTG and grown overnight.

PMSF 100mM and cocktail of protease inhibitor were added to the cells 1:100 (v/v) and cells were subjected to one French Press cycles (Constant Systems Ltd). After those, the cell homogenate was centrifugated and the supernatant loaded in a Ni^{2+}-affinity column and eluted with a 20-300 mM linear gradient of imidazole in 20 minutes. The elution peak was dialyzed against PBS, then incubated overnight at 22°C with thrombin protease (according to manufacturer's instructions, Amersham Biosciences) and loaded again in a Ni^{2+}-affinity column to separate the protein of interest from the cleaved His-tag. The flow-trough was collected, concentrated and loaded into a Superdex 200 column (GE Healthcare Life Sciences). The eluted protein was stored at 4°C with 3 mM DTT and 0.02% NaN_3 as

preservative or frozen in liquid nitrogen and stored at -80°C for long-term storage. Protein purity, integrity and dimerization were checked after purification and/or storage by SDS-PAGE and by size exclusion chromatography.

2.3.3 Recombinant proteins conjugation with fluorescent dyes

The aforementioned C141 mutant was used to obtain a fluorescently labeled aS. Labeling was performed adding a 5-fold molar excess of the reducing agent TCEP to C141 dissolved in 20 mM Tris buffer (pH 7.0). After 30 minutes of incubation, Oregon Green 488 maleimide (Molecular Probes, Invitrogen) was added to the protein at a 5:1 stoichiometric ratio and the reaction was left at 45 °C for 4 hours. The conjugated aS (aS-OG) was separated from the unreacted protein, fluorophore, and reducing agent by reverse phase HPLC cromatography.

14-3-3 η was mixed with a 20-fold molar excess of Oregon Green 488 isothiocyanate F_2FITC (Molecular Probe, Invitrogen) in PBS, 20 mM Sodium Bicarbonate pH 9.0. The solution containing the conjugated protein (14-3-3η-OG) was incubated for 5 hour at 25°C and then dialyzed overnight against PBS, 5 mM DTT to eliminate the fluorophore excess.

2.3.4 Protein aggregation assays

Aggregation experiments were performed at 20 μM aS for AFM analysis, and at 70 μM to follow the kinetic of the process; all aS solutions were ultra-filtered with a 100 kDa cut-off Millipore (Sartorius) filter to remove possible aggregates from the starting monomeric solution. In some of the experiments 14-3-3η was added to afford specific aS:14-3-3η stoichiometric ratios (please refer to the results section 4.2). For fluorescence polarization measurements (Section2.4.1), 1:100 of aS-OG or 1:25 of 14-3-3η-OG were added.

The aggregation experiments were carried out in PBS, supplemented with 0.05% (w/v) Sodium Azide and 5 mM DTT (when not stated differently), at 37°C and providing a constant agitation at 1000 rpm. The

sample volume was 200 µl and the aggregation was performed on a 96-well polycarbonate plates, in PCR vials or in 1.5 ml-volume vials.

2.3.5 Alpha-synuclein fibrils sonication

aS fibrils sonication can break fibrils into smaller fibrillar objects whose dimensions depends on the sonicator used, on the power and the length of the treatment and on the dimensions of the tip. For this reason, we believe that a characterization of the objects obtained after the sonication is needed, rather than a precise protocol for fibrils sonication that could be influenced by the factors above mentioned.

With this premise, we modulated the sonication protocol used and obtained seeds with different characteristics and check them by atomic force microscopy. The seeds characteristics are discussed in the Chapters 3 and 4.

2.3.6 Reverse-phase HPLC chromatography

Reverse-phase HPLC analyses were performed on aS to verify purity and to separate the unbound to the OG-bound aS after protein conjugation with the fluorophore.

The instrument used was 1100 Series HPLC system (Agilent Technologies), equipped with a diode array absorbance detector. The column connected to the HPLC was Jupiter 5µ C4 300 Å, 150 x 4.60 mm (Phenomenex), with a stationary phase constituted by hydrophobic chains that interact with the analyte.

aS was loaded into the column and eluted with a linear gradient of acetonitrile (0.085% trifluoroacetic acid) versus water (0.01% trifluoracetic acid) in 38 minutes, at a flow rate of 0.6 ml/min. aS's retention time in this conditions is about 18.1 minutes.

2.3.7 Sodium dodecyl sulphate polyacrylamide gel electrophoresis (SDS-PAGE)

SDS –PAGE allows the separation of proteins according to their size in polyacrilamyde gel in the presence of SDS and applying an electric field. SDS-PAGE was performed using stacking and resolving gels, prepared as described in the Materials section 2.1.

Before loading protein samples or cell lysates into the gel, samples were boiled about 10 minutes in the presence of Laemmli loading buffer. Samples were the loaded into the wells and a +100 V potential was applied; after the proteins enter the resolving part of the gel, the potential is increased to +150 V. The running buffer used was previously described (2.1 Materials) and the low molecular weight markers were used as reference in each gel (Precision Plus Protein dual extra standard, BioRad).

After running, gel was stained with Coomassie solution and then destained and stored in a 10% acetic acid solution.

Alternatively, proteins separated by SDS-PAGE were blotted on a PVDF membrane (Immobilin-P, Millipore), previously reactivated in methanol, applying a 100 V potential for 90 minutes in transfer buffer.

2.3.8 Western Blot analysis (WB)

2.3.8.1 Protein quantification for WB

Before loading cell lysates into SDS-PAGE wells, total soluble proteins quantification was performed to allow the loading of the same amount of proteins in each different well. Cells were harvested mechanically directly in the lysis buffer and kept on ice for 30 minutes. The lysates were centrifugated for 30 minutes at 15000 rpm at 4°C and supernatants collected. Total protein concentration was assessed via Pierce BCA Protein Assay Kit and a plate reader (Victor X3, Perkin Elmer).

2.3.8.2 Western Blot

After blotting the proteins on the membrane, it was saturated with 10% w/v milk in TTBS (blocking solution) for 30 minutes at room temperature. Then the membrane was incubated with the proper primary antibody diluted in the blocking solution for 1 hour at room temperature. After three TTBS washes, the membrane was probed with the secondary antibody diluted in the blocking solution, for 1 hour at room temperature. Finally, the membrane, washed three times with TTBS, was covered with ECL WB Detection reagents (GE Healthcare) and then exposed to an ECL Hyperfilm (GE Healthcare) for a period sufficient to detect the bands.

The film was developed with a developer solution and a fixer solution (GBX Kodak). Densitometric bands analysis was performed, when needed, using the plug-in of ImageJ properly designed for this purpose (http://rsbweb.nih.gov/ij/).

2.4 Biophysical methods

2.4.1 Proteins and DNA quantification

Proteins absorbance was measured at 280 nm using an UV-visible diode-array spectrophotometer (Agilent 8453) and proteins concentration was calculated using Lambert-Beer law:

$$c = \frac{A}{\varepsilon l}$$

where *c* is protein molar concentration, *A* is the measured absorbance at 280 nm, *l* is the cuvette light path (usually 1 cm) and ε is the protein molar extinction coefficient in $M^{-1}cm^{-1}$.

aS	ε [$M^{-1}cm^{-1}$]	Molecular Weight [Da]	Amino acids
aS WT	5960	14460.1	140
aS-C141	5960	14563.2	141

The absorbance of aS-OG and 14-3-3η-OG was measured at 496 nm with the same spectrophotometer and the concentration was calculated considering the molar extinction coefficient of the fluorophore (ε_{OG}= 81000 $M^{-1}cm^{-1}$) instead the one of the protein.

14-3-3 isoform	ε [$M^{-1}cm^{-1}$]	Molecular Weight [Da]	Amino acids
14-3-3 β	27515	28082.4	246
14-3-3 ε	29005	29173.9	255
14-3-3 γ	31985	28302.5	247
14-3-3 η	29005	28218.7	246
14-3-3 τ	27640	27764.2.	245
14-3-3 ζ	27515	27745.1	245
14-3-3 σ	26025	27774.0	248

The molar extinction coefficients ε shown in the two previous tables are related to all the proteins that were used in this thesis work; they were calculated starting from the aminoacidic sequence using ProtParam Tool (http://web.expasy.org/protparam/) and are in units $M^{-1}cm^{-1}$, at 280 nm in water.

Plasmidic DNA concentration was obtained measuring diluted DNA solution absorbance at 260 nm, where it presents its absorbance maximum. A 260nm-measured absorbance *A* of 1 corresponds to a double strand DNA concentration of 50 ng/μl. Therefore, plasmidic DNA concentration in the samples could be easily calculated as follows:

$$[\text{ds DNA}] = A_{260\ nm} \cdot 50\ \text{ng}/\mu\text{l} \cdot \text{diluition factor.}$$

Plasmidic DNA spectra can give information also on the purity of the DNA in term of protein contamination. The ratio between A_{260nm} and A_{280nm} should be around 1.8 in a pure double strand DNA preparation.

2.4.2 Fluorescence polarization

2.4.2.1 Fluorescence polarization experiments

Aggregation assays performed on 96-well plates as described in section 2.3.4 were monitored with Fluorescence polarization (FP) measurements at 535 nm, conducted at intervals of 6-10 hours via a plate reader (DTX 880 Multimode Detector, Beckham Coulter). Excitation wavelength was 490 nm.

2.4.2.2 Fluorescence polarization principles

Fluorescence polarization spectroscopy or anisotropy is a suitable tool to study protein aggregation. It was used for the study of aS aggregation kinetics in vitro for the first time by Luk and co-workers (Luk *et al.*, 2007) and has the big advantage of revealing not only protein large aggregates or fibrils but also oligomeric species.

The method requires fluorescent molecules in solution; therefore, the protein has to be labeled with a fluorescent dye. When

excited with a plane polarized light, the protein will emit light in the same polarized plane if it remains stationary throughout the excited state. On the contrary, the polarization of the emitted light will vary if the molecule rotates out of this plane during the excited state. Fluorescence polarization *P* and fluorescence anisotropy *r* are defined as:

$$P = \frac{I_{||} - I_{\perp}}{I_{||} + I_{\perp}}$$

$$r = \frac{I_{||} - I_{\perp}}{I_{||} + 2I_{\perp}}$$

where $I_{\parallel}$ is the parallel component of the polarized light, while $I_{\perp}$ is the perpendicular component of the polarized light.

Both *P* and *r* vary depending on the rotational motion of the molecules in solution, being a direct relationship between *r(t)* and Stoke's diffusion law:

$$r(t) = e^{-6Dt}$$

where *D* is the diffusion coefficient, which is related to the viscosity of the solution μ and on the dimensions of the objects (*d*=diameter):

$$D = \frac{kT}{2\pi\mu d^2}$$

The relationship between r and the diameter of the objects in solution allowed monitoring the increasing dimension of aS aggregates over time in the presence or absence of 14-3-3η.

2.4.3 Thioflavin T fluorescence assay

ThT fluorescence emission increases upon binding to β-sheets structures. Therefore, measuring ThT fluorescence intensity at different time points allowed monitoring the quantity of aS fibrils formed over time.

The assay were performed as described elsewhere (Le Vine, 1993) using a microfiltered (cut off 0.22 μm) 25 μM ThT solution in 25 mM

sodium phosphate (pH 7.0). Constant volume aliquots of protein samples were taken at regular intervals during aggregation assays and diluted into the ThT-containing buffer (final volume 100 µl). Fluorescence emission measurements were conducted on a fluorimeter (Ls50, Perkin Elmer), at 25°C using an excitation wavelength of 440 nm and recording the ThT fluorescence emission spectra between 450 and 600 nm. Emission maximum, at 480 nm, was used to quantify the amount of β-sheet enriched protein.

2.5 Cell biology

2.5.1 Cell culture

Human Embryonic Kidney 293 cells (HEK293) were chosen because they are easy to grow and transfect, while SH-SY5Y neuroblastoma cell line was used because SH-SY5Y cells are dopaminergic and considered a good model for PD.

HEK293 and SH-SY5Y cells were cultured in the proper growth medium at 37°C in 5% CO_2.

2.5.2 Cell transfection

pcDNA-aS and pEGFP-aS were used for HEK293 and SH-SY5Y transient transfections to obtain suitable models to study aS oligomerization and aggregation in fixed and live cells. HEK293 cells were plated between 50% and 70% confluency, depending on the experiments, and transfected using polyethylenimine (PEI) as transfection reagent, with a DNA:PEI ratio equal to 1:3 for both the aS expression plasmids used. SH-SY5Y cells were plated at about 60% confluency and transfected by Lipofectamine (Invitrogen) with a DNA:Lipofectamine ratio ranging from 1:3 to 1:5, depending on the experiment.

pEGFP-aS and pEBG14-3-3η plasmids were used for HEK293 transient co-transfections, performed in Optimum medium using (PEI) as transfection reagent (DNA-PEI ratio was 2:3), when cells were at a density of about $5*10^5$ cells/cm^2 (about 35% confluency). To assure that almost all the cells overexpressing aS-EGFP were also overexpressing 14-3-3η, the DNA amount ratio was always maintained 2:3.

HEK293 were also transfected with both pEGFP-aS and pdsRED-14-3-3η using Lipofectamine as transfection reagent to maximize the co-expression of the two proteins in advanced imaging experiments. Total DNA:Lipofectamine ratio was kept at 1:3.

When needed, aS seeds obtained as described in Section 2.3.5 and characterized as in 4.3, were added to the medium during transfection to

induce aS fibrils formation in cell cytoplasm and to obtain LB-like inclusions in this cell model. Cells were washed in DPBS (Gibco) and the media was changed after 3 hours for Lipofectamine transfected cells and after 12-24 hours for PEI transfected cells.

2.5.3 Immunocytochemistry

Cells were plated on poly-lysine (50 μg/ml solution of poly-L-lysine in milliQ H_2O) coated coverslips before transfection. At the desired time, cells were fixed with methanol at -20°C for 20 minutes, permeabilized with PBS with 0.1% Triton and blocked with PBS with 5% FBS (Blocking solution). Blocked cells were then stained with the suitable primary antibody properly diluted in the blocking solution. The counterstaining was done with Alexa Fluor antibodies diluted in blockin solution (see 2.1 Materials). Cells were also stained with Hoechst 33242 (Invitrogen), diluted in PBS or milliQ H_2O 1:10000 to visualize the nuclei.

Widefield images were collected using a fluorescence microscope (Leica DM5000B), while higher resolution fluorescence microscopy images were acquired with a confocal microscopy (Nikon Eclipse E6000). Excitation wavelength for aS-EGFP and Alexa Fluor 488 was 488 nm, while for Alexa Fluor 568 it was 568 nm; proper filters were chosen to maximize signal and minimize background.

2.5.4 Organelles staining

To obtain more information on the effects of aS overexpression and aggregation in live cells, staining of mitochondria and lysosomes was performed and confocal images were acquired simultaneously with the data acquired to perform N&B analysis (Section 2.7.1).

Lysosome detection was performed staining cells with LysoTracker Red (Invitrogen) to a final concentration 100 nM in culture media for 45 minutes at 37° in 5% CO_2. Tetramethylrhodamine ethyl ester perchlorate (TMRE) (Sigma) was used to reveal mitochondria. Cells were incubated

with TMRE in culture media solution at a final concentration of 500 nM, for 30 minutes at 37° in 5% CO_2.

Signal from lysosomes or mitochondria, stained respectively with LysoTracker and TMRE, were collected on a Olympus FluoView1000 using an excitation wavelength of 561 nm, with a laser power from 6% to 12%.

Filters were set to 505-525 nm for green channel (for N&B signal detection) and to 560-660 nm for the red channel (lysosomes or mitochondria). Several cells (at least 15) were imaged for each sample in at least 3 independent experiments (if not stated differently).

2.5.5 Time-lapse imaging for cell viability assays

To perform a viability assay after aS-EGFP overexpression in cells in different conditions, HEK293 cells were observed with an inverted fluorescence microscope (Leica DMI 4000B) every 12 hours after transfection for 3 times, maintaining the same experimental setup in the microscope. EGFP or aS-EGFP expressing cells were counted and compared to the total cells in the field to measure the viability of overexpressing cells over time. To assure significativity to these results at least five fields per culture were acquired and the experiments were repeated 3 times independently.

2.6 Atomic force and electron microscopy

2.6.1 Atomic force microscopy imaging

AFM imaging is a very useful tool to characterize aS aggregates: in this work it was used to precisely quantify aS fibrils and aggregates morphological features, i.e. length, diameters and curvature.

AFM imaging was performed in tapping mode with Ultrasharp NSC15/AlBS silicon probes having a nominal resonant frequency of 325 kHz (Mikromasch, Tallin, Estonia) on a NanoScope IIIa SFM system equipped with a Multimode head and a type-E piezoelectric scanner (Bruker, Mannheim, Germany). 10 µl of sample were deposited on freshly cleaved mica (RubyRed Mica Sheets, Electron Microscopy Sciences, Fort Washington, USA) and left to adsorb for 5 min at room temperature (~20 °C). The mica surface was then rinsed with ~500 µl of MilliQ H_2O (Millipore Simplicity) at the same temperature and dried with dry nitrogen.

In most experiments, the sample was diluted ~10 times with PBS then equilibrated at RT for 10' prior to deposition in an attempt to minimize overlap of individual α-syn aggregates. Multiple images from successive depositions were then pooled and digitalized to obtain statistically significant morphological measurements as outlined below. AFM imaging was performed in collaboration with Dr. M. Brucale, National Research Council (CNR), Rome, Italy.

2.6.2 Electron microscopy imaging

TEM images are generated by the interaction between the electrons beam and the ultrathin specimen that constitutes the samples. TEM can be used to study several different kinds of samples, i.e. fixed non-in vivo biological samples, and provides a resolution considerably higher than light microscopy and that is in the order of nanometers. Electron microscopy was used in this work to probe the characteristic of aS aggregates and to verify the presence of aS fibrils after inducing the aggregation in cell cytoplasm.

TEM samples were prepared by adsorbing a 15 µl aliquot taken from an aS aggregation batch onto a carbon-coated copper grid, then performing negative staining with a 0.05% uranyl acetate solution.

For immuno-TEM, grids were first incubated with a rabbit polyclonal primary antibody against 14-3-3η (ABCAM) previously diluted 1:200 in PBS, then washed in PBS and finally incubated with a gold-coupled secondary antibody against rabbit IgG. After a second washing step in PBS the grids were negatively stained, as described above.

For electron microscopy, HEK293 or SHSY5Y cells were transfected with aS and treated with seeds, cultured for 4 days, fixed overnight in 0.1 M sodium cacodylate buffer at pH 7.4 containing 2.5% glutaraldehyde; after processing, cells were embedded in LR White resin (Polysciences, Warrington, PA). Ultrathin sections were stained with uranyl acetate for investigation.

TEM pictures were taken on a Tecnai G2 12 Twin instrument (FEI Company, Hillsboro, OR).

2.6.3 Automatic fibrils recognition and measuring in AFM and TEM images

Diameters (and curvatures) of the amyloid aggregates were measured directly from the AFM images via a semi-automated tool (Aioanei, 2012) that automatically recognizes fibrils and interpolates their shape with a cubic B-spline function. The Z scale values of the individual pixels crossed by the B-spline in the AFM image are pooled to obtain the distributions of the apparent diameters. (Local curvature is reported as the reciprocal of the osculating circle radius at each pixel crossed by the B-spline function).

When recording AFM images to be measured with the fibrils recognition tool, special care was taken to obtain images in which the fibrils appeared well spread and isolated on the surface rather than overlapped and tangled. This analysis was performed in collaboration with Dr. M. Brucale, National Research Council (CNR), Rome, Italy.

2.7 Advanced fluorescence microscopy

Considering the limitation of conventional light microscopy techniques in the study of complex and dynamic biological system, we decided to go for newly developed fluorescence microscopy techniques that were set at the Laboratory for Fluorescence Dynamics (LFD), at the University of California, Irvine – USA (http://www.lfd.uci.edu/).

These methods are based on the study of different properties of fluorescence signals that are hidden in confocal images (if acquired properly), and that are usually not taken into account in conventional confocal microscopy assays, i.e. fluorescence intensity fluctuation analysis, fluorescence lifetime imaging or spectral imaging.

The analysis of all these data was performed using SimFCS software, developed by Prof. E. Gratton at LFD (http://www.lfd.uci.edu/globals/).

For all these experiments about $8.5 \cdot 10^5$ cells were plated in 35 mm dishes with a 14 mm microwell for imaging (MatTek, Ashland, MA, USA) coated with fibronectin (Invitrogen).

2.7.1 Number & Brightness and cross-Number & Brightness methods

2.7.1.1 Number & Brightness and cross-Number & Brightness principles

Number and Brightness (N&B) method is based on fluorescence fluctuation analysis and allows separating pixels with many dim molecules, from pixels with few bright molecules (Digman et al., 2008 (a)). The aggregation state of a protein is related to the first (average) and second moment (variance) of the fluorescence intensity distribution. Considering an average, a small variance corresponds to a large number of molecules that contribute to that average, while a large variance corresponds to few contributing molecules. The mathematical equations that describe the relationship between the average ⟨k⟩ and the variance σ^2 of the fluorescence intensity distribution and the apparent number of molecules N and the apparent brightness B for every pixel are:

$$N = \langle k \rangle^2 / \sigma^2$$

$$B = \sigma^2/\langle k \rangle$$

N and B values can be expressed in term of the number of particles (n) in the volume of excitation and the molecular brightness ε:

$$N = \varepsilon/(\varepsilon + 1)\, n$$

$$B = \varepsilon + 1$$

The N and B values pixel per pixel and their distribution were obtained using SimFCS software (www.lfd.uci.edu). One of the parameter that has to be calibrated to use the method is the S_{factor}, which is related to the characteristics of the microscope (Digman *et al.*, 2008 (a); Ossato *et al.*, 2010). The apparent brightness B of the molecules in cells is affected not only by the fluctuation due to fluorescence molecules movement, but also by photo bleaching and cell movements. To correct for these unwanted contributions a high pass filter algorithm (detrend filter) was applied to the stack of images. Detrend filter returns the average intensity at each pixel and deletes the fluctuations due to motion and photo bleaching that are slower than the particles fluctuation.

The oligomers size *S* was the calculated considering the B value for the monomeric protein and the different brightness values for the oligomeric species:

$$S = (B_{oligomers} - 1)/ (B_{monomers} - 1)$$

Considering the average N value we could estimate protein concentration in cell cytoplasm. N value calculated by SimFCS is the mean apparent number of molecules in the focal volume of the microscope. To calculate the real number of molecules the point spread function of the microscope has to be considered. The volume of the point spread function for a confocal microscope, that is about 0.2 femtoliter, can be used to calculate the mean concentration of protein in cells.

For a more detailed description of the method and the parameters see Digman *et al.*, 2008 (a) and Ossato et *al.*, 2010.

Cross-N&B method was applied for the study of proteins complexes formation in live cells (Digman et *al.*, 2009 (a)). It allows detecting the interaction between proteins fused with a fluorescent protein; localizing the position of the formed complex and determining the stoichiometric ratio between the two proteins in the complex. Cross-N&B is based on the idea that fluorescence fluctuations corresponding to two different fluorescent molecules are correlated only if the two interact. Information on the dynamic of the system can be obtained from the cross-correlation between the fluctuations of the signals coming from the two different fluorescent molecules.

To obtain these results cross-variance has to be calculated:

$$\sigma_{CC}^2 = \frac{\sum(G_i - \langle G \rangle)(R_i - \langle R \rangle)}{K}$$

where G_i ((or R_i) is the intensity of a pixel in the green channel, while ⟨G⟩ (or ⟨R⟩) is the average intensity over the *K* frames.

Cross-brightness B_{CC} can be easily derived from σ_{CC}^2 just normalizing this value with respect to the average intensity for both green and red channels (respectively $\langle k_G \rangle$ and $\langle k_R \rangle$):

$$B_{CC} = \frac{\sigma_{CC}^2}{\sqrt{\langle k_G \rangle \langle k_R \rangle}}$$

The B_{CC} plot was obtained plotting B_{CC} versus the brightness of the two channels B_1 and B_2, giving as result two different B_{CC} plots. The symmetry of these graphs reveals the information concerning the presence or the absence of cross-correlation, i.e. interaction. If the plot is asymmetric, it means that there is a positive cross-variance and that the two molecules interact. On the contrary, when the plot is centered on 0, it suggests that the fluctuations in the fluorescence are independent, as far as the two molecules.

From this analysis a stoichiometry map can be obtained: this contour plot displays the number of pixel in the image that shows each possible combination of brightness values in monomer brightness unit. This representation allows detecting the most populated region in term of a precise B_1 and B_2 couple, which corresponds to the prevalent

complex in that image, with a defined stoichiometric ratio. Detrend filter was applied also in this case.

For a more detailed treatment see Digman *et al.*, 2009 (a).

2.7.1.2 Number & Brightness and cross-Number & Brightness experiments

For N&B analysis, HEK293 or SH-SY5Y cells were transfected with 1 μg pEGFP-aS, or pEGF as control, using Lipofectamine (Invitrogen) as transfection reagent, with a DNA:Lipofectamine ratio = 1:5.

Confocal microscopy data were acquired with the Olympus FluoView1000 confocal laser scanning microscope, using an UPLSAPO 60 × water 1.2 NA objective.

N&B data were acquired using an excitation wavelength of 488 nm and laser power was set at 0.1% and 100 frames were acquired for each cell, with a pixel dwell time of 20 μs. The image size was 256×256 pixels and the 100 images of each stack were acquired in about 2 minutes. Imaging started after 24 hours from transfection and cells were observed at intervals for 24 hours.

The laser power and the scanning conditions were calibrated transfecting SH-SY5Y and HEK293 with EGFP and measuring the brightness value B for the nonaggregating monomeric EGFP. The S_{factor} obtained for the experiments described in Chapter 3 with this instrumentation was 1.32.

For cross-N&B analysis, HEK293 were transfected with 1 μg DNA for the single transfection of dsRED, EGFP, aS-EGFP and 14-3-3η-dsRED, or with 2 μg total DNA for the co-transfections (aS-EGFP and 14-3-3η-dsRED, aS-EGFP and dsRED, EGFP and 14-3-3η-dsRED). DNA:Lipoectamine ratio was 1:3. After 24 or 36 hours cells were observed using the Zeiss 710 confocal microscope.

Excitation wavelength for the green channel was 488 nm, while for the red channel it was 561 nm, with a laser power of 1% in both cases. Internal customized filters were chosen in two wavelength

intervals for the two channels, i.e. 490-550 nm for green and 610-661 nm for red, to avoid overlapping. Pixel dwell time was set at 12.61 μs and 100 images of 256×256 pixels, with a 50 nm pixel size, were acquired in about 1.5 minutes.

The laser power and the scanning conditions were calibrated transfecting HEK293 with EGFP and dsRED independently. The S_{factor} for each channel were calculated (1.46 for the green channel and 1.25 for the red one) as far as the brightness B_1 and B_2.

2.7.2 Raster image correlation spectroscopy (RICS) analysis and cross-RICS

2.7.1.1 RICS and cross-RICS principles

RICS is a technique used to study protein dynamic on time scales going from microseconds to milliseconds *in vitro* but also in live cells. It allows quantifying concentration and diffusion coefficient of fluorescent molecules and is based on the idea that the temporal information is hidden in the time structure of the scanning method (Digman et *al.*, 2005).

To obtain this kind of information from images, the 2D spatial autocorrelation function for each image in a stack acquired by a confocal laser scanning microscope is calculated as follows:

$$G(\xi,\psi) = \frac{\langle \delta i(x,y)\delta i(x+\xi,y+\psi)\rangle_{x,y}}{\langle i(x,y)\rangle_{x,y}\langle i(x,y)\rangle_{x,y}}$$

where $i(x,y)$ is the intensity of the image at each pixel, ξ and ψ are the spatial correlation shifts, $\delta i = i - \langle i \rangle$ and $\langle i(x,y)\rangle_{x,y}$ is the spatial average of the image.

The autocorrelation function is calculated for each image and then averaged. The result is fit with the equation that associates the correlation with the concentration and the diffusion coefficient of the molecules (in the easiest cases). The needed information are extrapolated from the fit.

For a more detailed protocol and mathematical treatment see Rossow et *al.*, 2010.

Cross-RICS method is based on the same idea, but it is applied to two different channels (Digman *et al.*, 2009 (b)). Cross-correlation function of a raster scan image for two images acquired in both channels simultaneously is calculated as follows:

$$G_{ccRICS}(\xi,\psi) = \frac{\langle I_1(x,y) I_2(x+\xi, y+\psi)\rangle_{x,y}}{\langle I_1(x,y)\rangle \langle I_2(x,y)\rangle}$$

where $I_1(x,y)$ and $I_2(x,y)$ are the intensities of the image at each pixel in the two different channels and ξ and ψ are the spatial correlation shifts.

Cross-correlation function in cross-RICS is different from 0 only when the fluctuations of the fluorescence in the two channels are correlated.

If the average of the cross-correlation over a stack of images is different from 0, it can be concluded that an interaction is occurring between molecules in green and red channels. The concentration and the diffusion coefficient of the complex can be inferred from the fit of the cross-correlation curve (termed cross-RICS map in the results section 4.8).

2.7.2.2 Cross-RICS experiments

For cross-RICS analysis, the same data acquired for cross-N&B were used (see 2.7.1.2).

2.7.3 Fluorescence lifetime imaging and phasor approach

2.7.3.1 Fluorescence lifetime imaging principles applied to autofluorescence in cells and tissues

Fluorescence lifetime microscopy (FLIM) provides an image based on the measurements of time-decay characteristics of a fluorescent sample. The fluorescence lifetime of the fluorophores rather than the fluorescence intensity is used to reconstruct a FLIM image.

Using confocal microscopes or multiphoton microscopes and applying this method to the study of cells and tissues can provide useful information on the identification and the spatial localization of intrinsic fluorescent probes, i.e. flavins, nicotinamide adenine dinucleotide (NADH), collagen.

However, FLIM analysis requires the fitting of the exponential decays that characterize fluorescence lifetime. The fits become more and more difficult to be done and interpreted with the increased complexity of the sample, i.e. cells and tissues, that is why a "fit-free" method to analyse FLIM data is needed.

2.7.3.2 Phasor approach to FLIM

Digman and collaborators in 2008 suggested that fluorescence lifetime data acquired in the time domain could be transformed into coordinates in the phasor space (Digman *et al.*, 2008 (b)).

FLIM data can be analysed by observing the pixel distribution in the phasor plot, rather than by fitting multiexponential lifetime decay in time domain.

Tha phasor transformations from time domain to the g and s components of the phasor plot are:

$$g_{i,j}(\omega) = \frac{\int_0^\infty I_{i,j}(t)\cos(\omega t)\,dt}{\int_0^\infty I_{i,j}(t)dt}$$

$$s_{i,j}(\omega) = \frac{\int_0^\infty I_{i,j}(t)\sin(\omega t)\,dt}{\int_0^\infty I_{i,j}(t)dt}$$

where i and j are the coordinates of a pixel in the image and ω the frequency ($\omega = 2\pi f$, with f = laser repetition rate, i.e. 80 MHz in these experiments). If the FLIM data are acquired in the frequency domain the phasor transformations are:

$$g_{i,j}(\omega) = m_{i,j}\,cos\varphi_{i,j}$$

$$s_{i,j}(\omega) = m_{i,j}\,sin\varphi_{i,j}$$

Where $m_{i,j}$ and $\varphi_{i,j}$ are the modulation and the phase of the emission with respect to the excitation.

Lifetime values can be expressed as a function of the modulation and the phase:

$$\tau_\varphi = \frac{1}{\omega}\tan(\varphi)$$

$$\tau_m = \frac{1}{\omega}\sqrt{\left(\frac{1}{m^2} - 1\right)}$$

All the possible lifetime decays can be mapped into the spatial representation constituted by the phasor plot.

The coordinates in the phasor plot for a single exponential decay $I(t) = Ae^{-t/\tau}$ are:

$$g(\omega) = \frac{1}{1 + (\omega\tau)^2}$$

$$s(\omega) = \frac{1}{1 + (\omega\tau)^2}$$

where τ is the lifetime of the decay and ω is the laser frequency.

All the single exponential decay lie on the semicircle of radius ½, going from point (0,0) to point (1,0). Point (1,0) is associated to a lifetime of 0, while point (0,0) corresponds to τ = ∞. All the combination of two single exponential must lie along the line joining the two lifetime points that are on the semicircle, while two molecules both characterized by a multiexponential decay are identified by two points inside the semicircle.

For a more detailed mathematical treatment and explanation of the method see Digman et al. 2008 (b).

This method was applied to the study of several different biological issues, allowing, for example, to determine the different metabolic states in germ cells (Stringari *et al.*, 2011) to distinguish different stem cells differentiation potential (Stringari *et al.*, 2012) or to study milliseconds spatiotemporal dynamics of FRET biosensors (Hinde et *al.*, 2013).

This method allowed us to study aS effects on cell metabolism looking at variation in NADH fluorescence lifetime in live cells and *in vitro*.

2.7.3.3 Phasor-FLIM experiments

Recombinant aS was obtained as previously described, suspended in sterile PBS pH 7.4 at a concentration of about 250 μM. A 250 μM NADH solution was prepared in PBS pH 7.4.

NADH solution was measured alone, mixed 1:1 with 1,000 unit/mL lactate dehydrogenase (LDH; Sigma), mixed 1:1 with the 250 μM aS solution, and after aggregating aS/NADH solution for one or two weeks at 37°C under agitation at 1000 rpm.

For phasor-FLIM analysis, HEK293 were plated as previously described and transfected with 2 μg of pcDNA-aS (Lipoectamine:DNA = 1:2.5) and observed after 36-48 hours .

Fluorescence lifetime imaging was performed using a Zeiss 710 coupled with a Ti:Sapphire laser (Spectra-Physics Mai Tai) and an ISS A320 FastFLIM. The acquisition settings were: image size of 256x256 pixels, pixel dwell time 25 μs/pixel and a 63X oil immersion objective. A dichroic filter (690 nm) separated the fluorescence signal from the laser light and a short-pass filter (610 nm) was placed in front of the photomultiplier (H7422P-40, Hamamatsu). The excitation wavelength for NADH was 740 nm.

FLIM calibration was obtained measuring the lifetime of fluorescein, which is known to be 4.04 ns. Data were acquired until more than 100 counts were collected in the brightest pixel of the image.

Every pixel in the FLIM image was transformed in a pixel in the phasor plot by SimFCS, as previously described. For the analysis of the average lifetime in each cell (whole cell or cell cytoplasm), the regions of interest in every frame were selected and the average g and s values were calculated.

2.7.4 Spectral imaging and spectral phasor

2.7.4.1 Spectral phasor principles

Spectral phasor idea is the same presented for phasor FLIM: the analysis and interpretation of spectral data can be complicated in certain

conditions. A possible solution is the use of phasor transformation to transform the spectral changes occurring at each pixel in a spectral image acquired as described below, into a phasor plot. The phasor plot shows the spectral properties of each pixel as a function of the coordinates of that pixel in a 360° circle.

This idea was first proposed by Fereidouni and co-workers (Fereidouni *et al.*, 2012) and spectral phasor transformations were adapted from the equations proposed in a previously published paper (Digman *et al.*, 2008 (b)).

The phasor transformations for the image *i* and for a discrete case were adapted as follows:

$$g_i(\lambda) = \frac{\sum_{\lambda=\lambda_s}^{\lambda_f} I(\lambda)\cos(n\omega\lambda)\Delta\lambda}{\sum_{\lambda=\lambda_s}^{\lambda_f} I(\lambda)\Delta\lambda}$$

$$s_i(\lambda) = \frac{\sum_{\lambda=\lambda_s}^{\lambda_f} I(\lambda)\sin(n\omega\lambda)\Delta\lambda}{\sum_{\lambda=\lambda_s}^{\lambda_f} I(\lambda)\Delta\lambda}$$

where λ_s and λ_f are the starting and final wavelengths of the spectrum, *n* the harmonic number and ω the frequency ($\omega = 2\pi f$, with f = (n·spectral channels)$^{-1}$).

The transformations can be applied to successive harmonic to obtain a better distribution of the pixels of the dataset.

2.7.4.2 Spectral phasor experiments

Spectral phasor experiments were performed on the very same sample solutions prepared for phasor-FLIM experiments (2.7.3.3).

Data acquisition was done on the Zeiss 710 using a 63×/1.4 Oil objective and exciting the sample at 740 nm. The images were acquired in the spectral mode of the microscope, using 32 channels with a 9.73 nm of bandwidth, going from 416.32 nm to 727.65 nm. Pixel dwell time was 177 ms, image size was 512×512 and each image was the result of an averaging of 2-4 acquisitions.

Data were acquired using Zeiss software and analysed using SimFCS.

2.8 Statistical analysis

2.8.1 Significativity and frequency count

The statistical analysis for immuno-TEM and on cell images, i.e. frequency counts, Student's test and ANOVA test, were performed using OrginPro8 (OriginLab).

The p value considered statistically significant was $p<0.05$, represented on the histograms with a single "*". When the p value was lower than 0.01, the graphical representation was "**", while "***" were drawn for $p<0.001$.

2.8.2 Mitochondria quantitative analysis

A tailored code (Matlab) for the quantitative analysis of mitochondria morphology and distribution in live cells was developed. After the selection of a threshold to eliminate the contribution due to the background of the TMRE stained mitochondria image, the distances among all pixels showing intensity above threshold were calculated to obtain a distribution representing the distance between pixels within mitochondria and among mitochondria, a parameter that could be associated to mitochondrial dimensions and distribution in the cell cytoplasm.

Chapter 3

Results.

Alpha-synuclein aggregation in PD cell models

"The moment one gives close attention to anything, even a blade of grass it becomes a mysterious, awesome, indescribably magnificent world in itself."

Henry Miller

In this chapter, results concerning the study of aS oligomerization and aggregation in cell models (HEK293 and SH-SY5Y lines) will be presented. aS oligomerization in live cells was observed using advanced fluorescence microscopy methods (Section 2.7.1 and 2.7.3), while larger aggregates formation was studied introducing recombinant aS fibrils fragments (seeds) in cell cytoplasm to trigger the aggregation, as it was proposed in the literature. Further characterization of the toxic effects induced by aS aggregation was performed. Specifically mitochondrial function, autophagic lysosomal pathway activation and cell metabolism, through NADH fluorescence imaging, were investigated.

3.1 Seeding alpha-synuclein aggregation in cells

The study of aS aggregation in cell models is very important in the determination of toxic effect(s) induced by this process. However, there are two main issues: (i) limited resolution of conventional microscopy techniques does not allow characterizing the early steps of the aggregation process and (ii) simple overexpression of aS does not lead to the formation of amyloid fibrils or larger LBs-like aggregates, characteristic of PD pathology.

To overcome the second problem, a new method was recently introduced to trigger aS aggregation in cell models (Luk *et al*., 2009; Danzer *et al.*, 2009; Waxman *et al*., 2010; Nonaka *et al*., 2010). The method is based on the use of fragments of recombinant aS fibrils, termed seeds, that are introduced in cells, along with the aS DNA plasmid, through a transfection reagent. aS seeds work as nucleation centers in the cytoplasm favoring the formation of aS fibrils formed by addition of overexpressed aS.

The seeds were obtained through sonication of recombinant aS fibrils, as described in section (Section 2.3.5), and were characterized by TEM and AFM to obtain information on their morphology and on their average dimensions (Figure 3.1). Varying the sonication conditions allowed producing seeds with different average length and diameters: the characterization of these objects will be discussed in a following section, because differences in their dimensions affect aS aggregation mainly *in vitro* (Section 3.2.3), while it is less evident in cells.

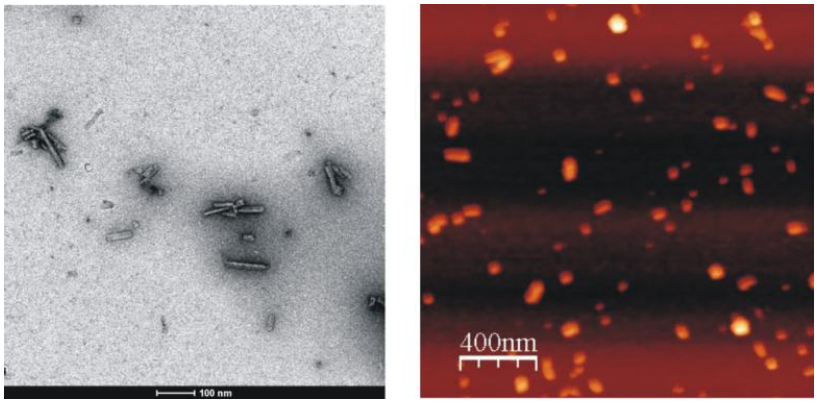

Figure 3.1 - Recombinant aS fibrils fragments, termed seeds, obtained as described in the Materials and Methods chapter (Section 2.3.5). Imaging was done by TEM (on the left) and AFM (on the right).

In Figure 3.2, the comparison between cells overexpressing aS and cells where aggregation is triggered by seeds are shown in fluorescence microscopy images (panel A) and details are shown in a confocal image of a single cell for two different samples (panel B).

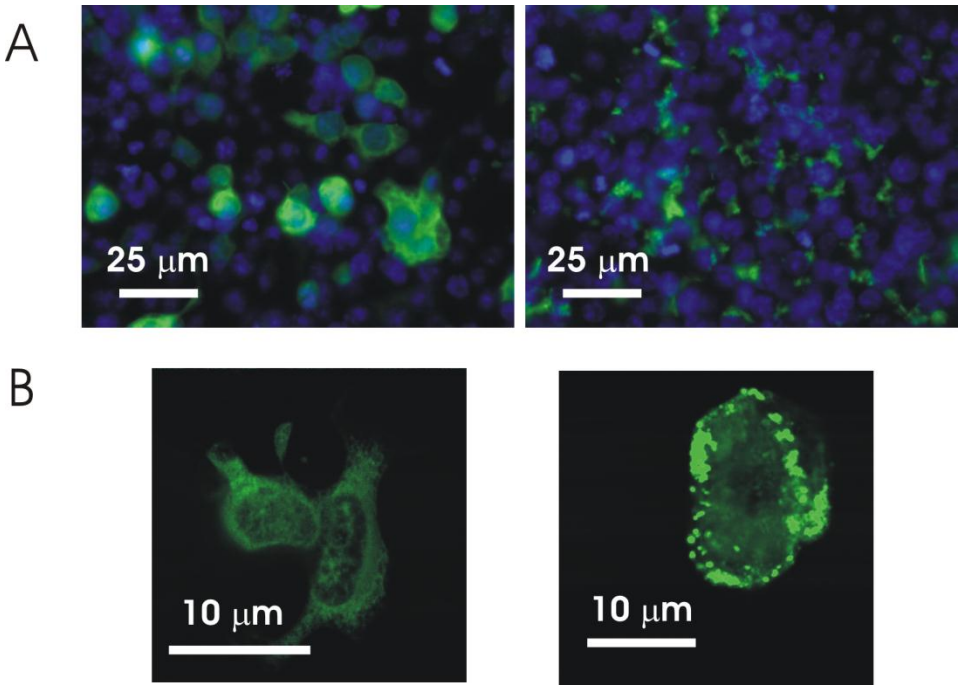

Figure 3.2 – A. Fluorescence microscopy images of cells overexpressing aS, on the left, and of cells showing aS aggregates because of aS overexpression and seeding (green – aS, DAPI – nuclei). B. Confocal fluorescence microscopy image for the same samples, on the left and on the right, highlighting the presence of aS inclusions in cells overexpressing aS and treated with seeds.

To verify the actual presence of aS fibrils in those cells positive for aS immunostaining, we fixed the cells with the methods required for TEM imaging that provide higher resolution. It can be clearly observed that cells treated with seeds and showing brighter spots in fluorescence microscopy images present aggregates, which resemble recombinant aS fibrils (Figure 3.3).

This method, as reported in the literature, allows obtaining LBs-like pathology in cellular models that can lead to a better understanding of the toxic mechanism(s) induced by aS pathology (Figure 3.2 and 3.3). We were able to obtain aS inclusions in an easy to grow and to transfect cell line, i.e. HEK293, as well as in SH-SY5Y cells, which are a dopaminergic line generally considered a more suitable as a PD cell model.

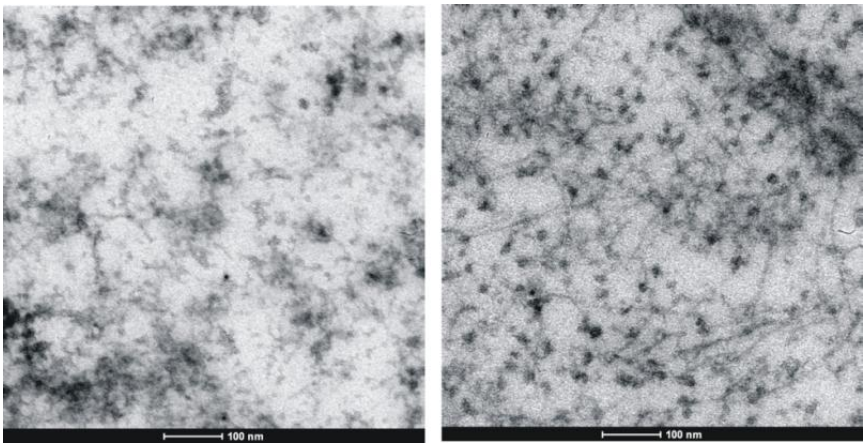

Figure 3.3 – TEM images of the cytoplasm of untransfected cells (on the left) and of the cytoplasm of cells overexpressing aS and treated with seeds (on the right), showing aS fibrils.

3.2 Cell viability in alpha-synuclein aggregation cell models

The study of the mechanism(s) of toxicity induced by aS aggregates is important for the understanding of the causes of neuronal death in PD. Moreover, the availability of validated cellular models for aS aggregation may be useful for the identification of molecules that could rescue aS induced toxicity.

To compare, the viability of cells overexpressing aS and cells overexpressing aS in which aggregation is triggered by seeds, we performed viability assays as described in the Section 2.5.5. The control used to evaluate the toxicity induced by the transfection reagents was EGFP overexpressing cells.

The histograms in Figure 3.4 show the percentage of cells overexpressing respectively EGFP, aS-EGFP and aS-EGFP with seeds treatment normalized for the control, at 12, 24 and 36 hours after the transfection of HEK293 cells.

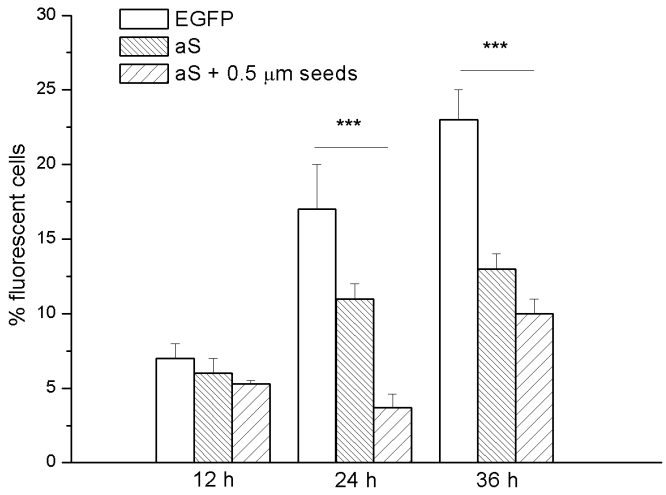

Figure 3.4 – Histograms showing the percentage of fluorescence cells after 12, 24 and 36 hours from transfection with EGFP, aS-EGFP and aS-EGFP plus seeds treatment. The percentage of fluorescent cells over time accounts for cell viability in the different cellular models for aS aggregation, compared to EGFP control.

It is clear that while the increase in the percentage of cells overexpressing EGFP is constant over time because of the continuous production of EGFP by cells that were transfected, the other two samples show a significant decrease in the amount of cells showing aS expression.

After 12 hours there is no difference between the three populations, but at 24 and 36 hours after transfection the aS-EGFP overexpressing cells are respectively about 65% and 57% of the control. This result indicates that the sole overexpression of aS is enough to exert a detectable toxic effect in cells. The introduction of aS seeds in cells cytoplasm triggers the aggregation and further increases the observed toxicity: at 24 hours the percentage of fluorescent cells is about 22% of the control. After 36 hours this value is considerably increased (43%) probably because the maximum peak of seeds induced toxicity is around 24 hours, while later the effect is mitigated by the continuous production of aS by the transfected cells that did not uptake seeds during the transfection. Another possibility is that part of the seeds starts to be degraded by cellular clearance mechanisms (Ebrahimi-Fakhari *et al.*, 2012) at 36 hours from transfection and therefore their toxicity is reduced.

In the literature it is reported that cell death in aS overexpressing cells and aS overexpressing cells plus seeding can be respectively ascribed to apoptosis in the first case, because of toxic mechanism(s) induced by aS oligomers and to necrosis in the second one, because of damage induced by larger aggregates (Nonaka et al., 2010; Nonaka and Hasegawa, 2011).

In Figure 3.4 it is shown an increase in the percentage of cells overexpressing aS-EGFP in the absence or presence of seeds treatment over time because of the competition between two mechanisms: the continuous expression of the aS by the transfected cells that increases the number of fluorescent cells and the concomitant toxic mechanism induced by aS overexpression and aS fibrils formation in cells that reduces the fluorescent cells in the sample.

3.3 N&B method to study alpha-synuclein oligomerization in live cells

The overexpression of aS and the induction of aggregation by seeding produces a cellular model that does allow the study of the latest stages in aS aggregation process. To study the early steps in the aggregation process we decided to turn to a new method, termed Number & Brightness Analysis, to detect possible aS oligomers after aS-EGFP overexpression in HEK293 and SH-SY5Y. The method is based on the analysis of the fluctuation of the fluorescence intensity signal (as described in section 2.7.1) and provides an average value of the apparent number of molecules N and the apparent brightness B of a stack of fluorescence microscopy images pixel per pixel. N can be directly related to the concentration of the protein in cell cytoplasm, while B is associated to the average dimension of the molecules in each pixel, i.e. it can be used to determine aS-EGFP aggregation state.

To evaluate the brightness B of monomeric EGFP, we overexpressed EGFP in SH-SY5Y cell line and acquire cell images in the conditions described in Materials and Methods section 2.7.1.2. After the estimation of the background contribution and the background correction, the B value solely due to monomeric EGFP in SH-SY5Y was calculated by averaging the B values obtained for EGFP in several different cells. In Figure 3.5 (panel A) the B values distribution for EGFP in a cell is represented. Fitting each cell histogram with a Gaussian curve we obtained a mean value and a standard deviation for B (15 cells):

$$B_{monomer}=1.18\pm0.16$$

Figure 3.5 (panel B) reports also the intensity map, the B color map e the N color map for a representative cell among those analyzed. B map provides information on the distribution of B values in the cells: for EGFP transfected cells the B color map shows a homogeneous blue color, representing the average value obtained for the monomeric EGFP. The N map on the contrary is more heterogeneous, indicating a heterogeneous distribution of the number of EGFP molecules in the cytoplasm. The intensity map and the N map are, as expected, in good agreement, since the intensity per pixel in this situation is due to the monomeric EGFP molecules.

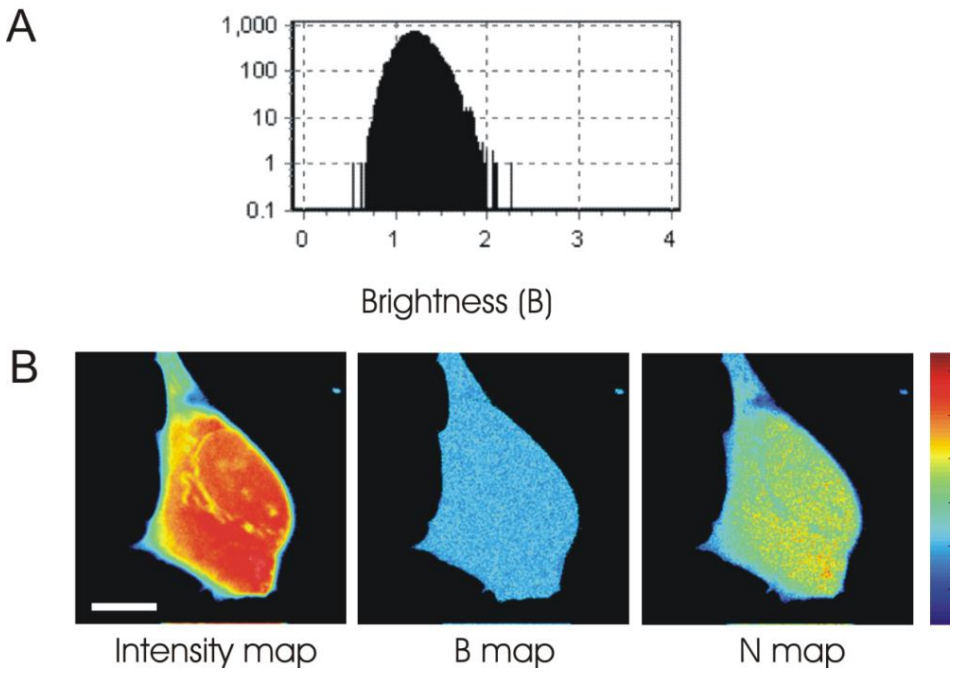

Figure 3.5 - A. Gaussian profile of the distribution of the brightness B values of EGFP overexpressed in SH-SY5Y cells is centered at B=1.18 and identifies the brightness of EGFP monomer under these imaging conditions.
B. Average intensity image of a cell overexpressing EGFP (Intensity map), B map and N map representing respectively the average brightness B and the average apparent number of molecules N per pixel. The maps show a homogeneous B distribution in the cell cytoplasm, as expected, while the N value distribution in the cell varies in good agreement with the Intensity map (color scale, a. u). White bar 10 μm.

After obtaining the B value for monomeric EGFP, which can be considered analogous to that of monomeric aS-EGFP, we analyzed the time dependence of the fluorescence properties of aS-EGFP transfected cells starting from 24 hours after aS-EGFP transfection: aS-EGFP aggregation state was evaluated at 24 hours, 36 hours and 48 hours after transfection. Interestingly, even at the first time point the sample presented a detectable level of heterogeneity in term of aS aggregation state.

A class of cells displayed a B distribution centered on approximately 1.18, which is the B value characteristic of the monomeric EGFP (Figure 3.6, panel A). From this result we hypothesized that the protein, at least in the conditions described here, is present also as monomer in the cytoplasm.

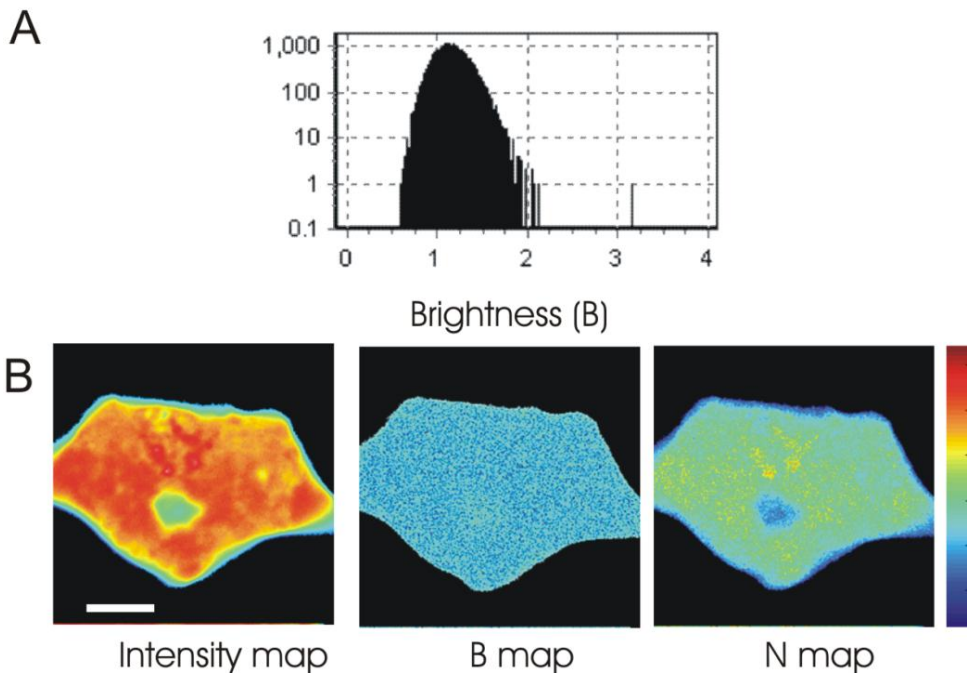

Figure 3.6 - A. Gaussian profile of the distribution of the brightness B of aS-EGFP overexpressed in SH-SY5Y cells is centered, as expected, at B=1.18 and identifies the brightness B of aS-EGFP in its monomeric form under these imaging conditions.
B. Average intensity image of a cell overexpressing aS-EGFP (Intensity map), B map and N map representing respectively the average brightness B and the average apparent number of molecules N per pixel. The maps show a homogeneous B distribution in the cell cytoplasm, meaning that aS-EGFP is monomeric in these conditions, while the N value distribution in the cell varies in good agreement with the Intensity map (color scale, a. u.). White bar 5 μm.

Next, we examined the conditions of cells 24 hours after the transfection and could identify in some cells by N&B analysis, pixels presenting not only a B value characteristic of the monomer, but also higher B values, compatible with aS oligomeric species.

Using $B_{monomer}$ value as reference, we were able to identify cells presenting oligomeric species from the brightness values. As can be seen in Figure 3.7 (panel A), the distribution of the brightness B for the representative cell transfected with aS-EGFP is broadened, meaning that for some pixels also higher B values compared to $B_{monomer}$ are calculated. This result indicates that at least some of the fluorescence in that pixel can be assigned to aS-EGFP oligomers.

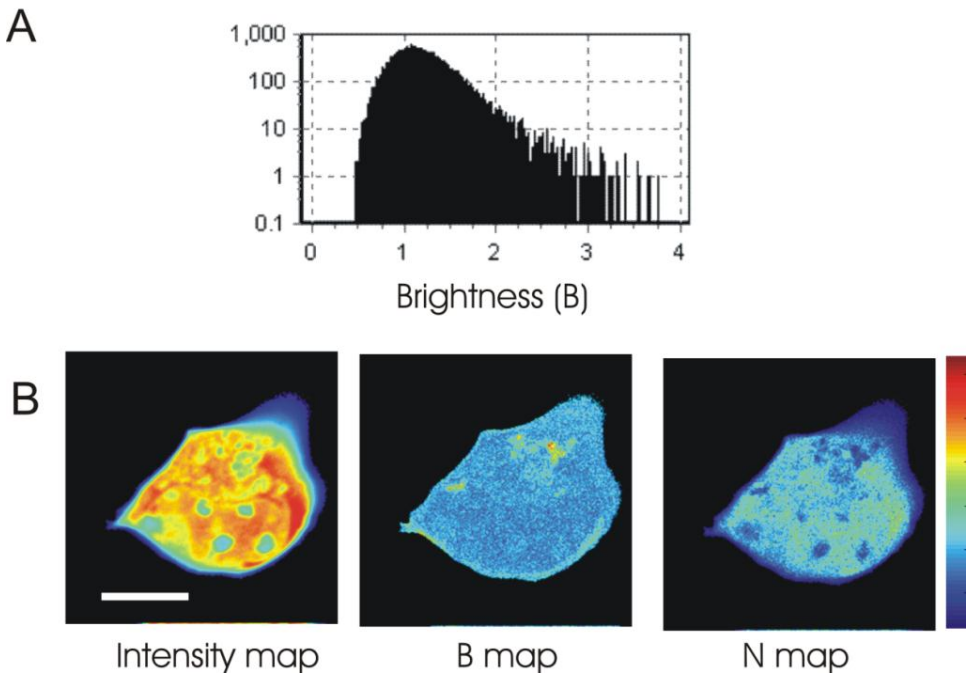

Figure 3.7 – A. Gaussian profile of the distribution of the brightness B values of aS-EGFP overexpressed in SH-SY5Y cells shows a large broadening due to the presence of a larger amount of aS-EGFP oligomers. The B value distributions for the different oligomeric species cannot be separated from the B distribution for monomeric aS-EGFP, however calculating a weighted average of the B values accounting for the oligomeric species we obtained about 1.95. This overall B value for the oligomers means that they are on average constituted by 6 aS-EGFP monomers.
B. Average intensity image (Intensity map), B map and N map representing respectively the average brightness B and the average apparent number of molecules N per pixel of a cell overexpressing aS-EGFP, corresponding to the Brightness distribution represented in panel B. The maps show a heterogeneous B value distribution in the cell cytoplasm, meaning that aS-EGFP formed oligomers. The N value distribution in the cell varies in good agreement with the Intensity map and where the B value is increased, the N value is lower than the average (color scale, a. u.). White bar 10 μm.

The distribution of brightness values for different cells were very different and not well separated from the Gaussian distribution centered on 1.18 representing the monomeric aS-EGFP. Moreover, it was not possible to separate the contribution of oligomers with different dimensions; accordingly, the standard deviation of the B values for the oligomeric species is 4-fold larger than the standard deviation of the B distribution of monomeric aS-EGFP. With this premise, we can only obtain an estimate of the mean brightness of the entire heterogeneous ensemble. Considering different cells and different experiments, we calculated a weighted average of the brightness of the entire ensemble of oligomeric species that is:

$$B = 1.98 \pm 0.65$$

The equation describing the relationship between the B values measured with N&B for a monomer and for oligomeric species and the aggregation size allowed us to calculate the mean dimension of the oligomers found in aS-EGFP transfected SH-SY5Y. On average, the oligomeric species are constituted by 6±4 aS monomers, which is in good agreement with a very recent estimate on aS early oligomers produced *in vitro* and observed with single molecules fluorescence techniques ($n \leq 10$) (Cremades *et al.*, 2012).

Imaging the cells at different time points after the transfection did not influence the percentage of pixels showing oligomeric species that were revealed: from about 8% to 30% in different cells.

We estimated the mean aS concentration in cell cytoplasm for different cells overexpressing aS-EGFP. Surprisingly, while the percentage of pixels showing oligomeric species in all analyzed cells is significantly variable, the mean concentration of aS calculated from the average N value in these cells showing oligomers is relatively stable (about 151±38 μM). Moreover, looking at all the cells, we found a reasonable value for the threshold concentration needed for the protein to form oligomers, which is about 80 μM. In those cells where a large part of pixels showed the presence of aS oligomers or a very high aS concentration, we could not observe a conversion of the oligomeric species into fibrillar structure, consistently with what is reported in the literature concerning aS aggregation in cell models (Roberti *et al.*, 2007; Klucken *et al.*, 2006)

These result suggests that both the B value, i.e. the average dimension of aS oligomers and the average percentage of pixels in cells presenting oligomers, are dependent not only on time, but also on other variables, such as concentration or activation of cellular clearance mechanism(s) that target aS oligomers.

Observing more carefully Figure 3.7 (panel B), it is clear that the distribution of the pixels containing aS oligomeric species is not homogeneous in cell cytoplasm, as if they were constrained in some cellular regions, sequestered or bound to cytoplasmic structures, i.e. organelles.

3.4 Alpha-synuclein oligomers are sequestered into lysosomes and can damage mitochondria

3.4.1 Alpha-synuclein oligomers sequestration by lysosomes

To verify if the confinement effect observed for the aS signal while looking at the B and the N maps of the cells presenting oligomers could be due to the presence of lysosomes sequestration, we stained aS-EGFP overexpressing cells and, as control, EGFP overexpressing cells with LysoTracker Red.

From the comparison the B map for aS-EGFP cells with the LysoTracker-stained lysosomes (Figure 3.8) it is clear that there is a partial overlap, suggesting that aS oligomers are enclosed into lysosomes, as shown in a mice model by Mak *et al.*, (2010) supporting the activation of ALP when the first toxic species form.

This result suggests that the presence of aS oligomers lead to the activation of the autophagic-lysosomal pathway (ALP) that is believed to be responsible for the clearance of misfolded aS (Ebrahimi-Fakhari *et al.*, 2012).

It should be mentioned that in lysosomes the pH value is around 5.0. This low pH can induce quenching of EGFP fluorescence (Patterson *et al.*, 1997) and consequentially influence the evaluation of both N and B values. However, the control performed on cells transfected with monomeric EGFP and stained with LysoTracker does not show any consistent variation in the brightness of the monomeric EGFP that colocalizes with lysosomes. Therefore, the pH quenching effect may induce (if any) only a negligible underestimate of the B values, surely not accounting for the higher brightness values assigned to the aS oligomeric species.

As can be seen in Figure 3.8, not all the pixels presenting oligomeric species are enclosed into lysosomes, accounting for a possibly progressive activation of the clearance system.

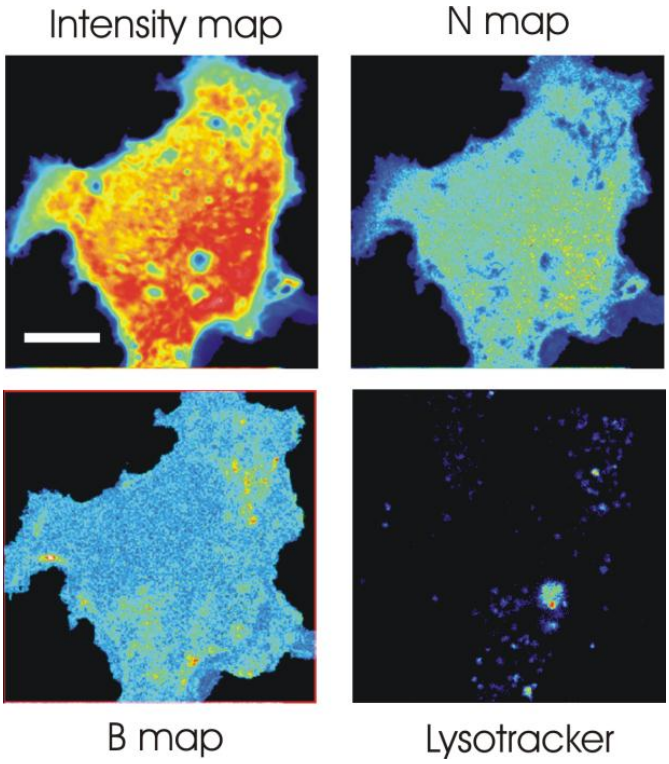

Figure 3.8 - Average intensity image (Intensity map), B map and N map of a cell overexpressing aS-EGFP and showing localized oligomeric species, in comparison with the same cell stained with Lysotracker. The correspondence between the pixels showing higher B values associated with the presence of oligomeric species and pixels positive to Lysotracker staining indicates that at least parts of the aS-EGFP oligomers are sequestered into the lysosomes after ALP activation (color scale, a. u.). White bar 10 μm.

3.4.2 Alpha-synuclein oligomers induce mitochondrial fragmentation

In 2011, Nakamura and co-workers proposed that one possible damaging mechanism that could be ascribed to aS is its direct interaction with mitochondrial membranes (Nakamura *et al.*, 2011). They showed that aS overexpression causes mitochondrial fission, but they could not verify the conformation that aS acquired while damaging mitochondria.

On these premises, the possibility of a direct interaction between aS oligomers and mitochondria was explored. To this aim, mitochondria were stained with a mitochondrial dye (TMRE) and to verify whether the presence of oligomers could be related to the mitochondrial fragmentation as previously proposed by Nakamura *et al.* (Nakamura *et al.*, 2011).

The comparison between mitochondria stained with TMRE in cells overexpressing EGFP or presenting aS-EGFP oligomers is shown in Figure 3.9 (Panel A and B). The difference in mitochondrial morphology and distribution is clear at glance, but a more precise quantification of these variations is also presented (Figure 3.9, panel C).

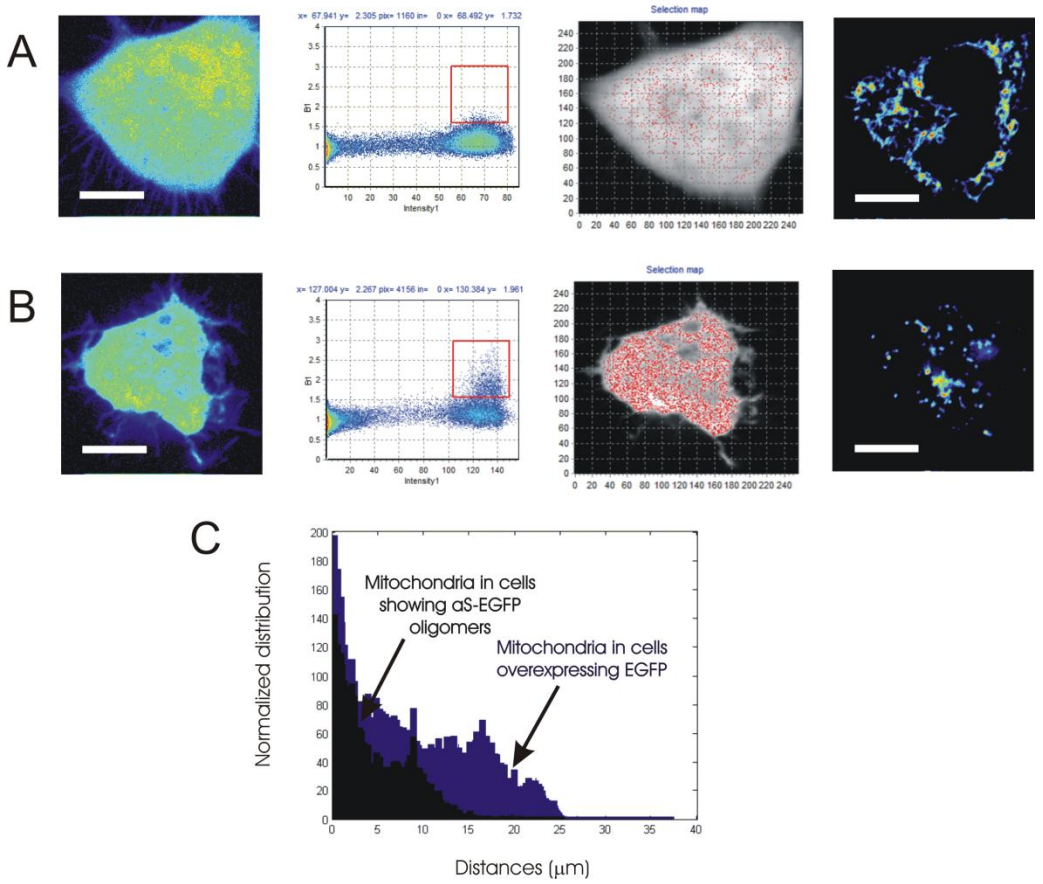

Figure 3.9 - A. Intensity map of a cell overexpressing EGFP (left panel), as control (color scale, a. u.). Corresponding distribution of B values per single pixel versus fluorescence intensity for the same cell (center panel), and associated Selection map where pixels selected with the red cursor in the B distribution are highlighted in red. On the right, TMRE staining for the same cell. White bar 10 μm.
B. Intensity map of a cell overexpressing aS-EGFP (left panel, color scale, a. u.). Corresponding distribution of B values per single pixel versus fluorescence intensity for the same cell (center panel), and associated Selection map where pixels selected with the red cursor in the B distribution are highlighted in red. The higher B values (red pixels in the Selection map) represent the oligomeric species present in this cell. On the right, TMRE staining for this cell. White bar 10 μm.
C. Distribution of distances among pixels positive to mitochondrial staining in the two cases presented in this figure at point A and B. The blue distribution represents the distances between pixels positive to mitochondrial staining in the cells overexpressing EGFP, while the black one shows the distances between pixels positive to mitochondrial staining in the cell overexpressing aS-EGFP and showing aS-EGFP oligomers. Both distributions are normalized by distribution area. The difference between the two distributions may account for mitochondrial fragmentation and alteration in mitochondria morphology and distribution in the cells cytoplasm of cells showing aS-EGFP oligomers, compared to the cells overexpressing EGFP cell. White bar 10 μm.

The distribution of distances between pixels positive to mitochondrial staining calculated as described in the Section 2.8.2 were plotted for cells overexpressing EGFP and cells overexpressing aS-EGFP and showing aS oligomers when analyzed by N&B method. The histograms visualize the information about the distribution of the mitochondria in the cell and their dimensions: when aS oligomers are present the organelles are smaller and less homogenously distributed in the cell cytoplasm, suggesting that they underwent to a fragmentation process. TMRE allows not only identifying mitochondria, but also to measure their membrane potentials using Nernst equation. In good agreement with what was published by Nakamura *et al.*, (2011) we could not highlight any difference in the mitochondrial potential based on this experiment.

3.5 NADH FLIM on alpha-synuclein aggregation cell models

Mitochondrial damages induced by aS overexpression suggested that also the NADH cell metabolism could be affected by the presence of aS oligomers and/or aggregates (Mayevski and Rogatsky, 2007). In particular, considering the higher NADH concentration in mitochondria it is plausible that an alteration in NADH fluorescence properties may occur as consequence of mitochondrial damages or alterations.

To test this hypothesis, NADH lifetime was studied in cells in which aS oligomers or aggregates were present. aS was overexpressed in HEK293 or aS was overexpressed and aggregation was triggered by seeds (aS+seeds) in the same cell line and the effects on NADH lifetime variation were analysed in comparison with a control (HEK293 cells transfected with the empty vector).

Considering the overlapping of NADH and EGFP fluorescence spectra, we could not use the pEGFP-aS plasmid used in cell viability and N&B experiments (sections 3.2 and 3.3) to overexpress aS. Therefore, a pCDNA-aS plasmid was chosen, to express wild type aS without any fluorescent tag, while seeding was performed as previously described (section 3.1).

The fit-free method applied to study NADH lifetime, termed phasor approach (Digman *et al.*, 2008 (b)), allowed a clear identification of free and bound NADH in terms of the differences of their lifetimes, pixel per pixel in the autofluorescence images (explained more in detail in section 2.7.3.2).

The phasor approach to FLIM produces a phasor plot where each pixel of a fluorescence image of a cell is represented in a point of coordinates (s,g) that corresponds to a precise lifetime of autofluorescence (at least in our case).

In Figure 3.10 (panel A) the autofluorescence intensities for empty vector, aS transfected HEK293 cells and aS transfected HEK293 cells plus seeding are shown and compared: it is clear that there are not differences in the intensities between the control and the cell models for aS aggregation.

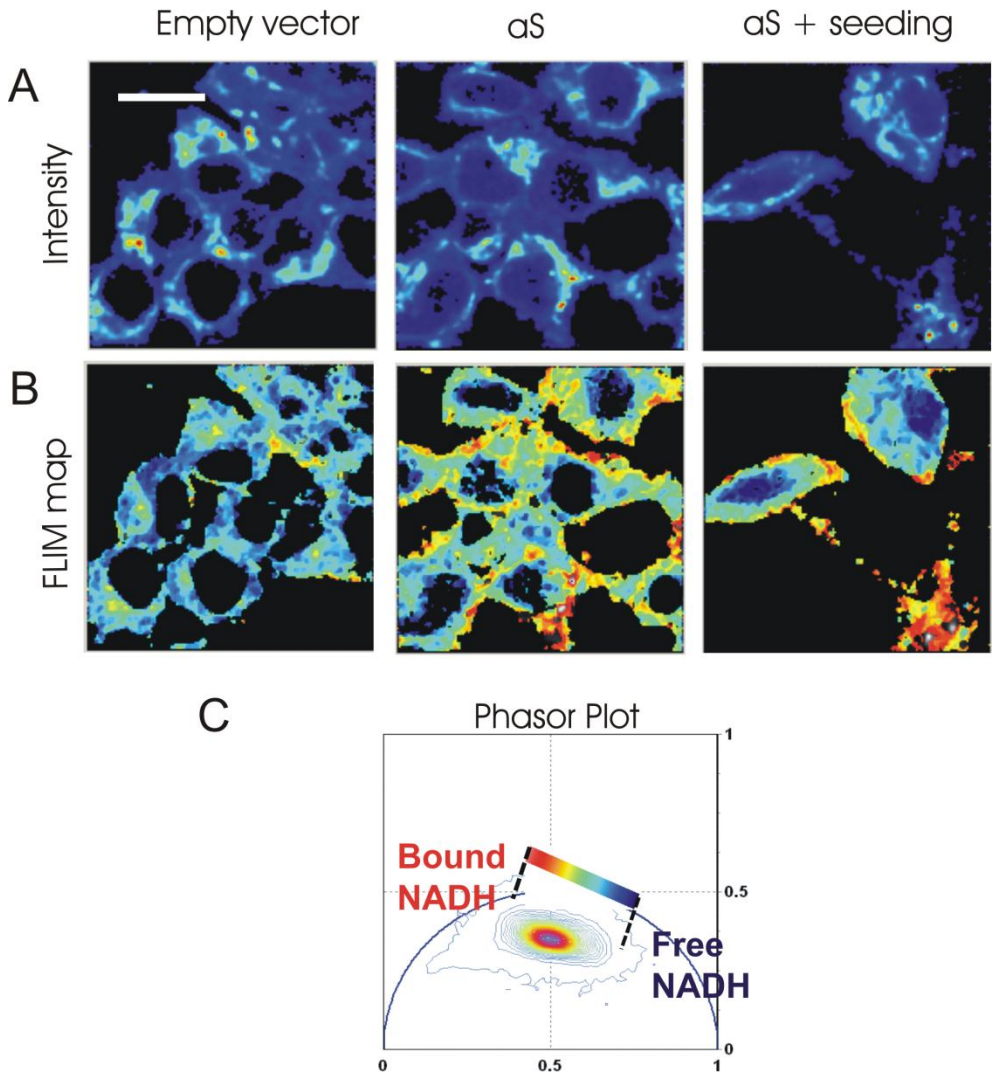

Figure 3.10 – A. Two-photon fluorescence intensity signal (color scale, a.u.) for HEK293 cells transfected with the empty vector (on the left), with aS (in the middle) and with aS plus seeding (on the right). White bar 30 μm.
B. FLIM maps corresponding to the previous reported fluorescence intensity signal for each sample, representing the fluorescence lifetime of each pixel in a color scale based on the phasor plot (C).
C. Phasor plot histogram represents the distribution of lifetimes in every pixel for 6 images for each sample. Color scale goes from blue, corresponding to the lifetime of free NADH, to red, corresponding to bound NADH lifetime.

On the contrary, as it is shown in the FLIM maps and in the correspondent Phasor plot (Figure 3.10 panel B and C respectively) there is an increase in the lifetime of NADH when aS is simply overexpressed or cells are additionally treated with seeds. The FLIM map shows in color scale pixels with different lifetimes (the longer in red, the shorter in blue), while the phasor plot presents a long tail corresponding to those pixels that have a very long NADH lifetime compared to the "normal" free or bound NADH lifetime. These spots

with longer lifetime are absent in the control, meaning that this effect is induced by aS oligomerization or fibrils formation. However, it is not known if this variation in NADH lifetime is due to a direct interaction of NADH molecules with aS aggregates or to an indirect effect due to aS aggregates induced toxicity, or both. Further experiments were performed to clarify this point (Section 3.6).

In Figure 3.11, microscopy images of zoomed-in cells in the two different aggregation conditions (aS overexpression and aS overexpression plus seeding) are presented and the correspondent phasor plot is shown. Here it seems that two different components for the pixels showing longer lifetime NADH are present (red and green). This result further supports the possibility of multiple mechanisms that induce NADH lifetime variation that will be investigated later.

Interestingly, it seems that the NADH species corresponding to an increased lifetime are mainly localized at the cellular membranes. A possible explanation for this localization is that this longer lifetime fluorescence is coming from NADH trapped into aggregates, which could be localized at the membranes, as previously observed by confocal microscopy for LBs-like inclusions (Figure 3.2, panel B).

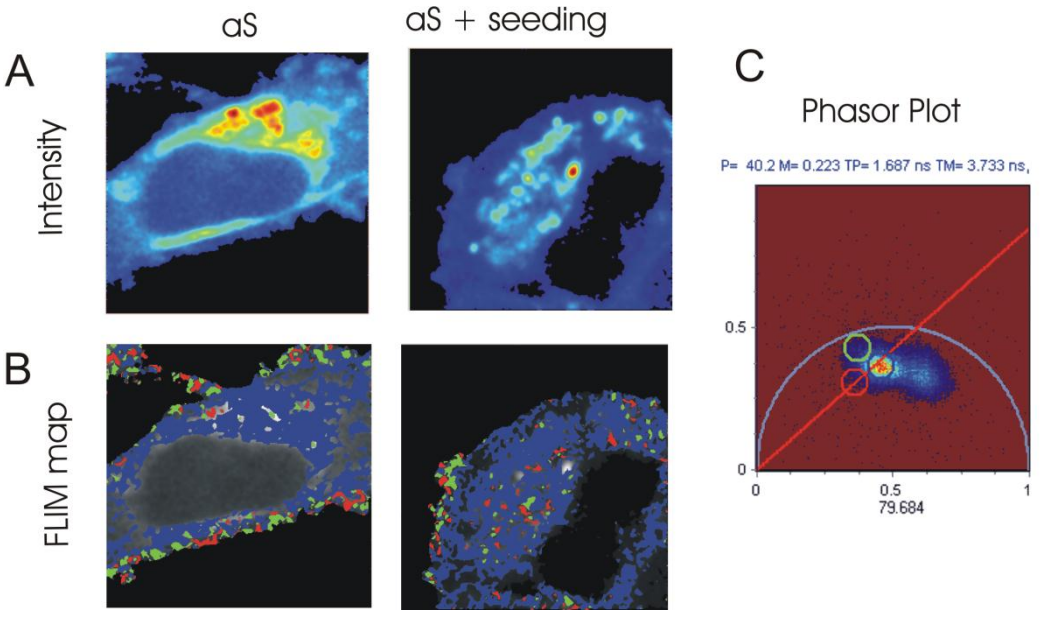

Figure 3.11 – A. Zoomed-in fluorescence intensity images of a region of cells overexpressing aS and overexpressing aS plus seeding. B. FLIM map corresponding to the phasor plot on the right (C), where the pixels selected with the green and the red cursors represent two different populations of NADH-bound species showing longer lifetimes and localized at the membranes: our interpretation suggests that this are the aS aggregates bound to NADH.

To quantitatively express the difference in the NADH lifetime between the three different samples, we calculated for every cell the average of the coordinates g and s of the phasor plot related to each pixel, which correspond to a specific lifetime, considering the whole cell or only the cell cytoplasm. Then we plotted g and s for cells overexpressing aS and for the control (Figure 3.12) for the whole cell or for the cell cytoplasm.

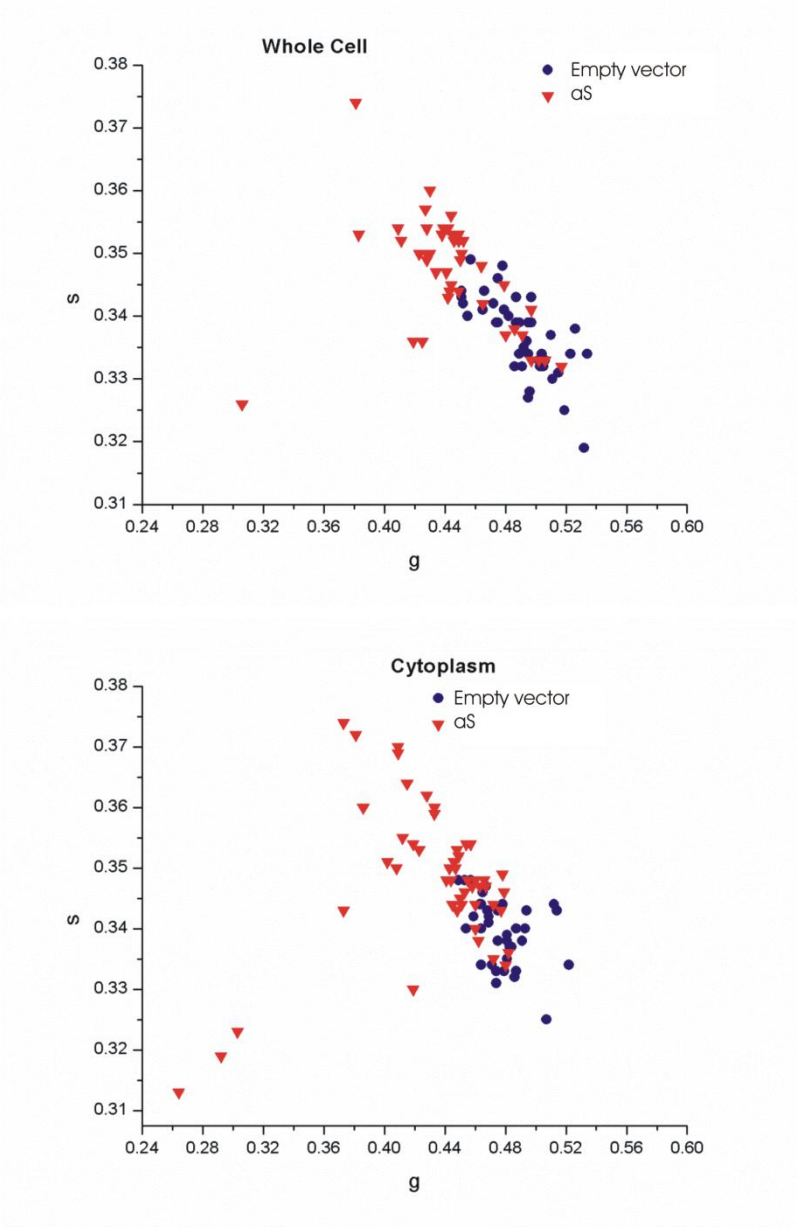

Figure 3.12 - Scatter plot of the phasor FLIM signature of each cell of a sample transfected with the empty vector and the other with aS. Each point represents the average phasor value in an individual cell of the two samples, being g and s the coordinates of each pixel in the phasor plot. In the first graph the average phasor value is calculated for the whole cell and in the second only for the cell cytoplasm.

In both cases, it is clear that two different populations in term of lifetimes are present, corresponding to aS overexpressing cells compared to the control. The non-complete separation is likely due to the contribution of those cells that are in the aS transfected cell ensemble, but that are not really transfected because of the transfection efficiency, which is about 30% for HEK293 transfected with pCDNA-aS.

The separation between the two populations is more evident when the mean lifetime is calculated only for the pixels placed in the cell cytoplasm, not for the whole cell. The NADH fluorescence signal in the cytoplasm comes mainly from mitochondrial NADH; therefore, the fact that variations in NADH are more evident in the cytoplasm suggests that the effects we are looking at may involve mitochondria and/or bound NADH.

Figure 3.13 shows the scatter plots for g and s values of aS overexpressing cells treated with seeds, compared to the control. In this second case the two populations are not clearly separated: this result can lead to few considerations. One explanation is that seeds lead to the formation of larger aggregates in cells, but they encompass a lower number of pixels compared to the oligomers, which are smaller, but in greater number. A second possible explanation is that seeds exacerbate a toxic situation that is present when aS is overexpressed, increasing toxicity as it was shown before (Section 3.2) and the consequent cell death in cells overexpressing aS; for this reason there is a reduction of the cells showing a longer NADH lifetime.

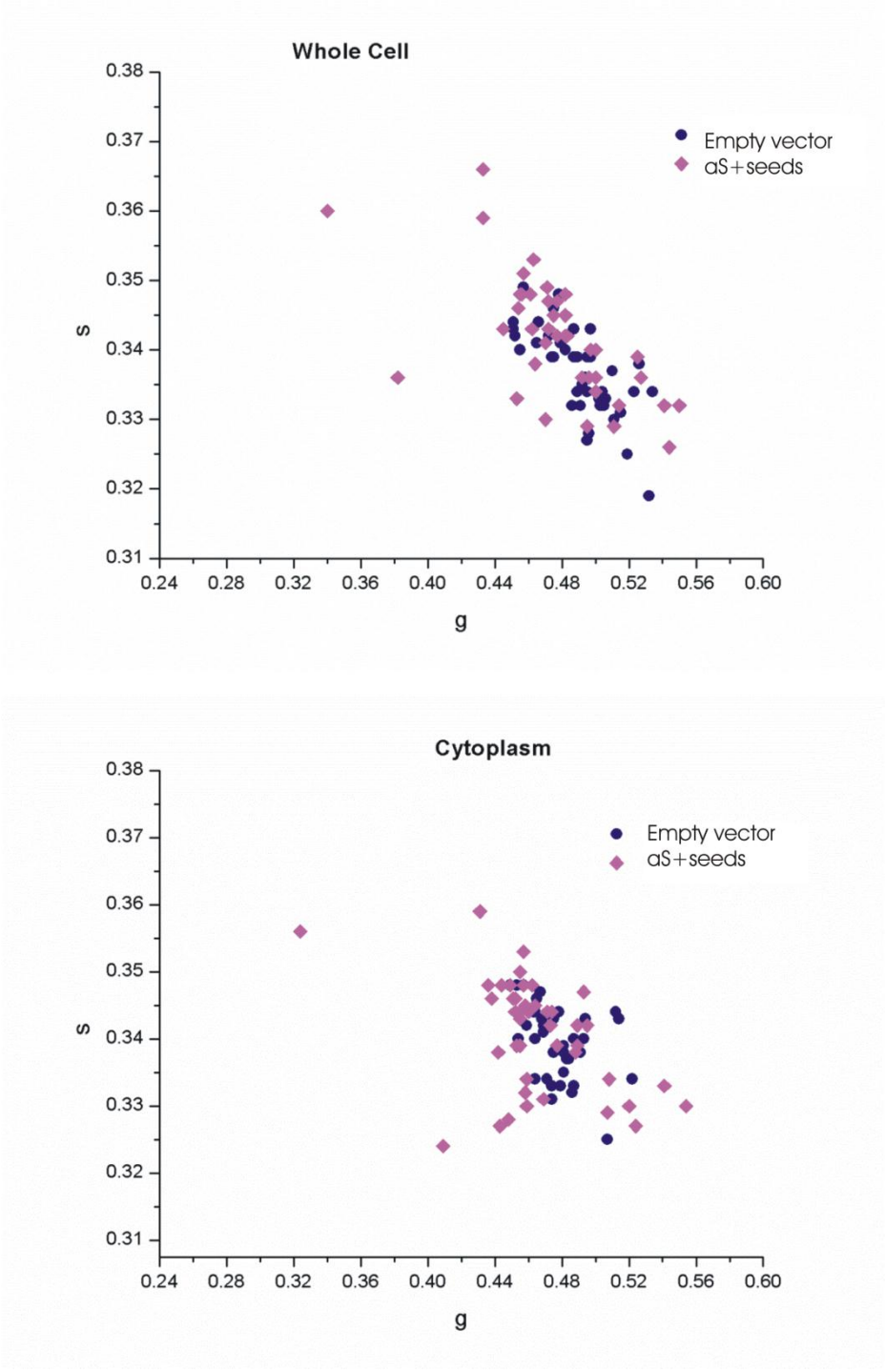

Figure 3.13 - Scatter plot of the phasor FLIM signature of each cell of a sample transfected with the empty vector and the other with aS and treated with seeds. Each point represents the average phasor value in an individual cell of the two samples, being g and s the coordinates of each pixel in the phasor plot. In the first graph the average phasor value is calculated for the whole cell and in the second only for the cell cytoplasm.

3.6 Lifetime and spectral characterization of NADH and alpha-synuclein aggregates *in vitro*

There are some different possible explanations for the longer autofluorescence lifetime induced by aS overexpression: (i) aS overexpression causes the variation of NADH lifetime in an indirect way, acting on other proteins or pathways; (ii) longer autofluorescence could be due to other autofluorescence sources in the cell (i.e. flavins, lipofuscins); (iii) aS oligomerization causes the sequestration of NADH by aS oligomers or larger aggregates, leading to an increase of NADH fluorescence lifetime that was also demonstrated for other NADH-oligomeric proteins complexes (Jameson *et al.*, 1989).

To rule out the second possibility, concerning other contributes to the detected fluorescence signal, we changed the excitation wavelength exploring other regions of the spectrum. This experiment allowed seeing if the contribution to the variation in autofluorescence lifetime was not due to NADH only, but to other autofluorescence sources whose excitation maximum corresponds to other wavelengths.

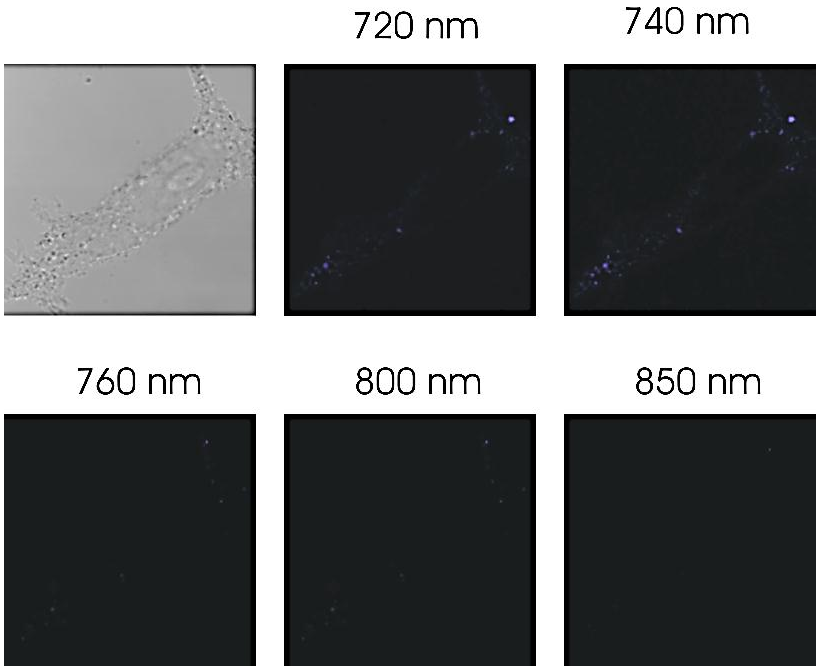

Figure 3.14 – Selected cell overexpressing aS and imaged in transmission and exciting at different wavelengths to verify the absence of contributes due to other sources of autofluorescence, i.e. flavins, lipofuscin.

As can be observed in Figure 3.14, exciting cell samples with different wavelength (720, 740, 760, 800 and 850 nm) does not show any increase in fluorescence signal, excluding the possibility of a strong contribution due to flavins or lipofuscins.

3.6.1 *In vitro* characterization of NADH lifetime variation in the presence of monomeric or aggregating alpha-synuclein

Considering the results shown in the previous paragraph, lifetime variations are mainly ascribable to NADH lifetime variation. To test if the longer lifetime was due to a direct interaction between NADH and aS, we performed some *in vitro* assays. NADH alone, NADH and aS, NADH and lactate dehydrogenase (LADH) and, finally, aS aggregated for one or two weeks in the presence of NADH were imaged, in the experimental conditions described at section 2.7.3.3.

FLIM analysis was performed for the different samples and the results are summarized in figure 3.15. NADH lifetime (red cursor in the image) and LADH-NADH lifetime (green cursor) are positioned in the phasor plot as expected and previously published (Stringari *et al.*, 2011) (Figure 3.15, panel A).

Surprisingly, also monomeric aS (pink cursor) induces a variation in NADH lifetime that is different from the one induced by aS aggregation (blue cursors) (Figure 3.15, panel B). To explain this variation we suggest that NADH could be sequestered into aS oligomeric species and amyloid fibrils, changing its fluorescence properties.

In both panel A and B, NADH lifetime distribution after its aggregation with recombinant aS is shown (blue cursor). In panel A, a two-week aggregation is shown, while in panel B indicates one-week aggregation. This difference could partially account for the distance between the two distributions in the phasor plot.

However, other aspects should be considered: (i) variation in the observed field that can lead to different amount of detected aggregates contributing to the signal; (ii) the heterogeneous distribution of aggregates

in solution that probably induce different variation in NADH fluorescence lifetime.

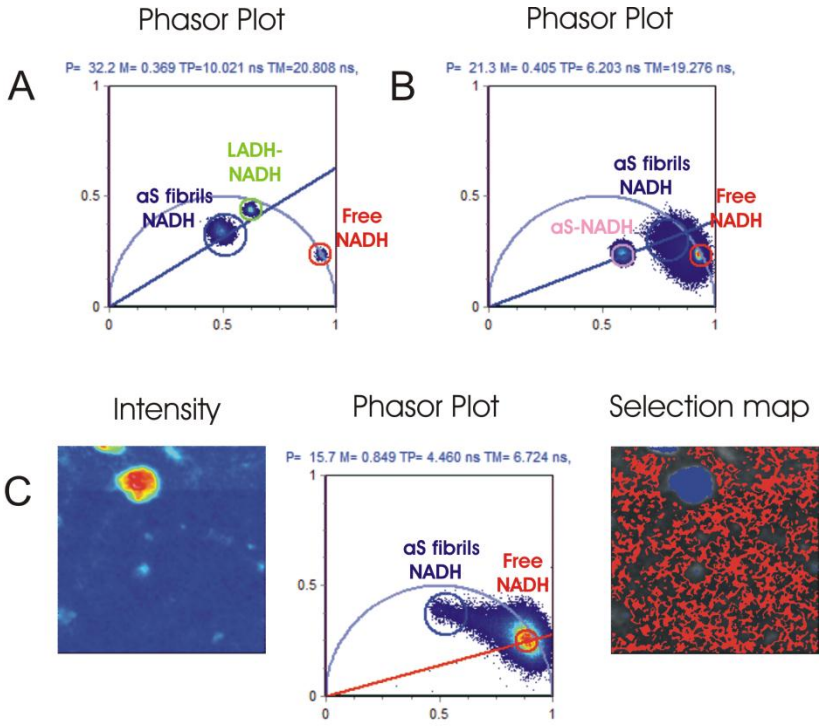

Figure 3.15 – A. In this phasor plot the position of the lifetimes corresponding to different NADH containing solution is represented: free-NADH and NADH bound to LADH as references, and aS aggregated in the presence of NADH for two weeks.
B. In this phasor plot the position of the lifetimes corresponding to other NADH containing solution is represented: free-NADH as reference, aS and NADH containing solution, and aS aggregated in the presence of NADH for one week.
C. In this panel, the NADH fluorescence intensity (color scale, a. u.) of aS aggregated in the presence of NADH solution is shown (on the left). The corresponding phasor plot is represented in the middle: it shows a broaden distribution accounting for species with different lifetimes, probably aS oligomers or aggregates that sequester NADH and change its fluorescence properties. In the selection map, on the right, the red pixels selected with the red cursor in the phasor plot represent the free NADH, while the blue pixels correspond to the large and bright object in the intensity map and show longer lifetimes.

Zooming in to further magnify the aggregates (Panel C) shows how the NADH containing species in solution present different lifetimes, going from the value corresponding to free NADH to the one that in panel B was assigned to aS fibrils. Using the blue cursor we highlighted the longer NADH lifetime objects, which correspond, in the intensity image on the right, to large brighter spots that we propose are aS fibrils.

NADH-aS aggregates morphology was assessed by AFM and their morphology resemble perfectly the one of canonical fibrils obtain aggregating aS alone; the results are shown in Figure 3.16.

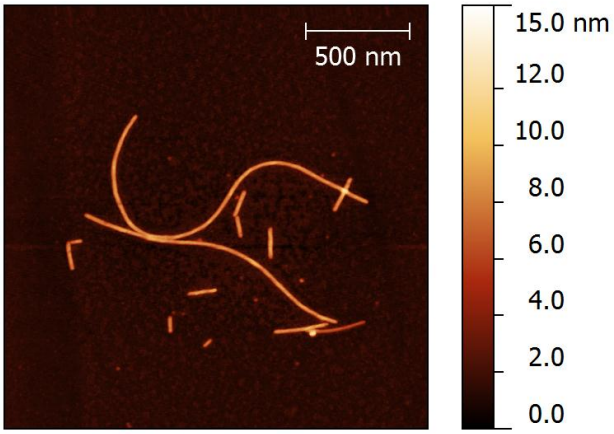

Figure 3.16 – AFM micrograph of aS fibrils obtained aggregating the recombinant protein with NADH for two weeks.

3.6.2 Spectral characterization of NADH fluorescence in the presence of monomeric or aggregating alpha-synuclein

To further characterize the differences in NADH properties in the presence of monomeric aS or when the protein is aggregates with NADH, we performed spectral phasor analysis on this sample.

Figure 3.17 reports the spectral phasor plot for free NADH (panel A) and for NADH in solution with aS (panel B). The position of the distribution in the spectral phasor plot allows the determination of the maximum of the spectra corresponding to each samples and the width of the Gaussian, assuming that the spectra could be fitted with that curve. For free NADH λ = 480.5 nm and Gaussian width is 46.2 nm, while for NADH in the presence of monomeric aS λ=481.5 nm with a width of 43.4 nm.

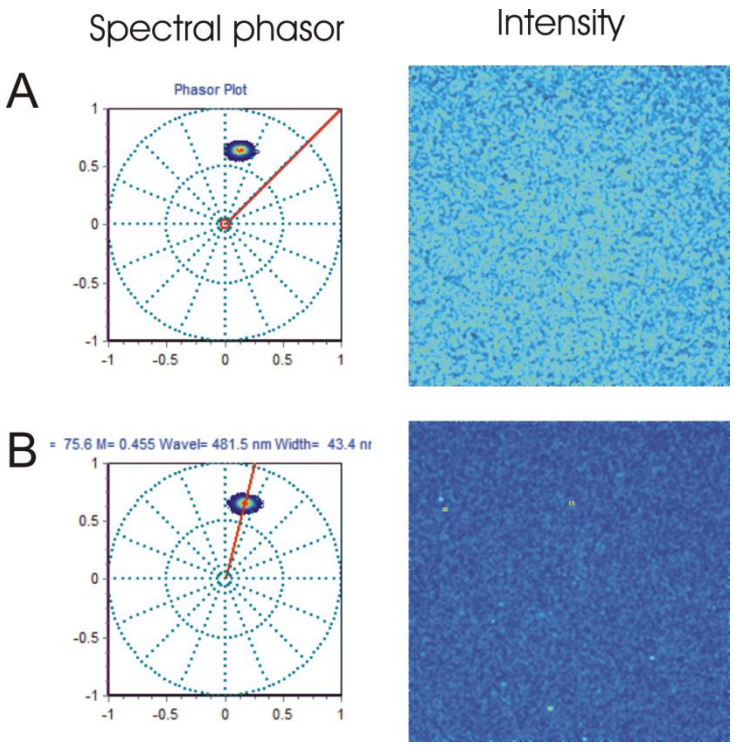

Figure 3.17 – Spectral phasor plot of NADH in solution (panel A) and to aS and NADH in solution (panel B), and correspondent fluorescence intensity. The 360° angle corresponds to the spectral range observed (from 416.32 nm to 727.65 nm) and the position of the pixels distribution in the spectral phasor plot corresponds to the maximum of the fluorescence spectra in each conditions when fit with a Gaussian profile.

In figure 3.18 is reported the same kind of analysis for the sample containing aS aggregated with NADH. In panel A the spectral phasor plots corresponds to all the pixels that constitute the image, while in panel B an intensity threshold was set to eliminate the pixels presenting lower signals. Using this method all the contributions due to free NADH that was still in solution with aS aggregates were eliminated and the distribution in the spectral phasor plot was sharper. This analysis allowed calculating the spectra maximum for NADH molecules that co-aggregated with aS: λ=476.6 with width 47.5 nm.

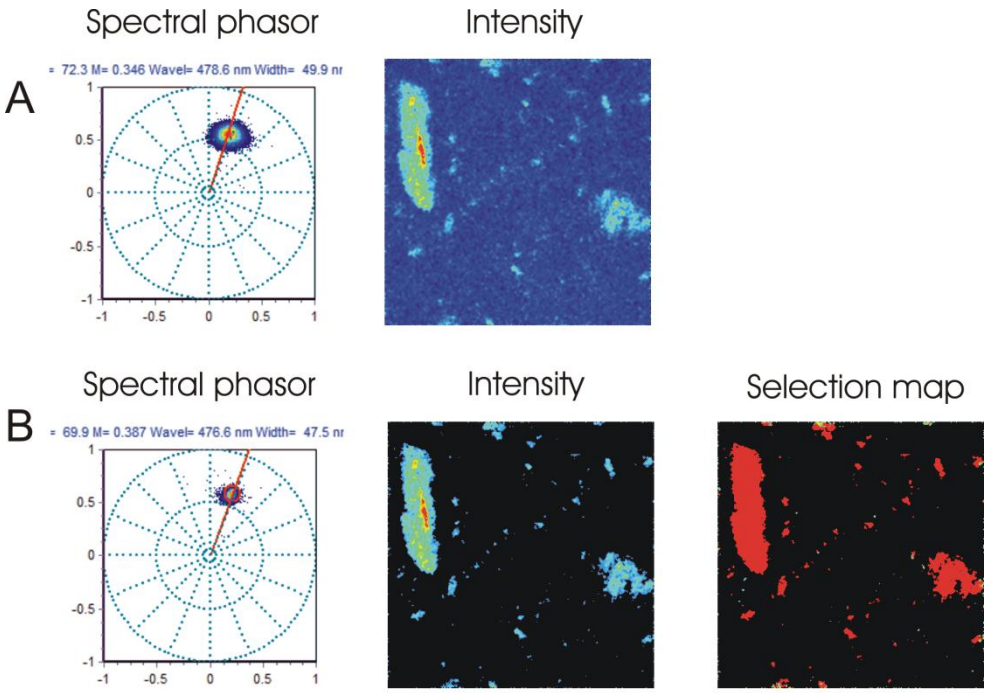

Figure 3.18 – Spectral phasor plot of NADH aggregated with aS for one week and correspondent fluorescence intensity (panel A). The 360° angle corresponds to the spectral range observed (from 416.32 nm to 727.65 nm) and the position of the pixels distribution in the spectral phasor plot corresponds to the maximum of the fluorescence spectra in each conditions when fit with a Gaussian profile. To obtain a less noisy pixel distribution in the spectral phasor a threshold was selected to eliminate the contribution due to free NADH. Spectral phasor of NADH aggregated with aS with a threshold (panel B), correspondent intensity and selection map (red cursor in the spectral phasor and red pixels in the selection map).

The shift of the spectra maximum toward smaller wavelengths compared to the free NADH is in good agreement with what is reported in the literature on the spectral variation of NADH bound to other proteins (Table 3.1).

	Free NADH	NADH-aS	NADH-aS aggregation	Free NADH*	Bound NADH*	Flavins*
λ (nm)	480.5	481.5	476.6	459	448	528
FWHM (nm)	46.2	43.4	47.5	91	91	77

Table 3.1- Summarizing table for NADH spectrum maximum obtained by spectral phasor analysis for free NADH, NADH-aS solution and aS aggregated in the presence of NADH, and reported in the literature (Palero *et al.*, 2011) for free NADH, bound NADH and flavins.

This consistent variation in term of spectral properties of NADH autofluorescence further supports the idea that NADH is bound to aS aggregates or fibrils and this binding strongly affects its fluorescence properties.

It is clear that monomeric aS, aS oligomerization and aS aggregation cause an increase in NADH fluorescence lifetime, compatible with the results that we obtained in aS cell models, and a shift in the maximum of fluorescence emission spectra *in vitro*.

This suggests that NADH autofluorescence properties could be used as label-free biomarker to observe aS aggregation progression *in vitro*, but also in cells and animal models.

3.7 Conclusions

These results show the characterization of aS aggregation in two different cells models. One allowed the characterization of aS oligomerization in live cells using confocal fluorescence fluctuation measurement and N&B analysis. These aS oligomers seem to be responsible for cellular toxicity and mitochondrial fragmentation. Moreover, they were found enclosed into lysosomes, suggesting the activation of ALP for oligomers clearance.

The other model here presented is devoted to the study of larger aS aggregates that resemble LBs and are obtained in cells triggering the aggregation with seeds.

In both cases a cell viability assay showed that aS oligomerization and aggregation induce cell death.

Considering the mitochondrial damage exerted by aS oligomers, the idea of an impairment of the cellular metabolism arose. To test this possibility, NADH fluorescence properties were characterized in the two cell models proposed for the study of aS aggregation and for aS aggregation *in vitro*, as control.

Interestingly, it has been shown that aS aggregation induces variations in NADH fluorescence lifetime and NADH spectral properties, suggesting that it could be used as a dye-free reporter for the study of aS aggregation *in vitro*, in cells and in vivo.

Chapter 4

Results.

Alpha-synuclein aggregation and 14-3-3 proteins

"Imagination is more important than knowledge. For knowledge is limited, whereas imagination embraces the entire world, stimulating progress, giving birth to evolution. It is, strictly speaking, a real factor in scientific research."

Albert Einstein

14-3-3 proteins effects on aS aggregation *in vitro* and in cell models were studied. In particular, recombinants aS aggregation assays were performed in the presence of 14-3-3 η isoform and the kinetic and the products of the process were studied using fluorescence spectroscopy, AFM and TEM. 14-3-3 η was then overexpressed in the previously presented aS aggregation cell models, to evaluate cell viability and aS aggregation in the presence of the chaperone, and aS/14-3-3 η interaction in a physiological environment.

4.1 Fluorescence polarization spectroscopy and Thioflavin T kinetics of alpha-synuclein aggregation process

Starting from the previously proposed interaction between aS and 14-3-3 η (Sato *et al.,* 2006), we purified both recombinant proteins from *E. coli* to performed *in vitro* assay on their putative interaction. The data published in the literature (Sato *et al.,* 2006) and NMR experiments performed in our laboratory in the past years showed that the two recombinant proteins do not bind to each other, suggesting that the verified in cell interaction occurs after structural or post-translational modification of one or both proteins. Our hypothesis was that it can happen during aS oligomerization or aggregation. To test this idea we evaluated the effect exerted by 14-3-3 η on the early steps of aS aggregation *in vitro*. To this aim we monitored the variation of the fluorescence polarization (FP) of an Oregon Green (OG) fluorescent probe covalently linked either to aS or to 14-3-3η at different time points in an aggregation assay, as proposed by Luk *et al.,* 2007. The time dependences of the FP values, of both aS and 14-3-3 η alone, were monitored in control experiments showing that aS forms oligomeric species and that 14-3-3 η has not propensity to aggregate (Figure 4.1, panel A).

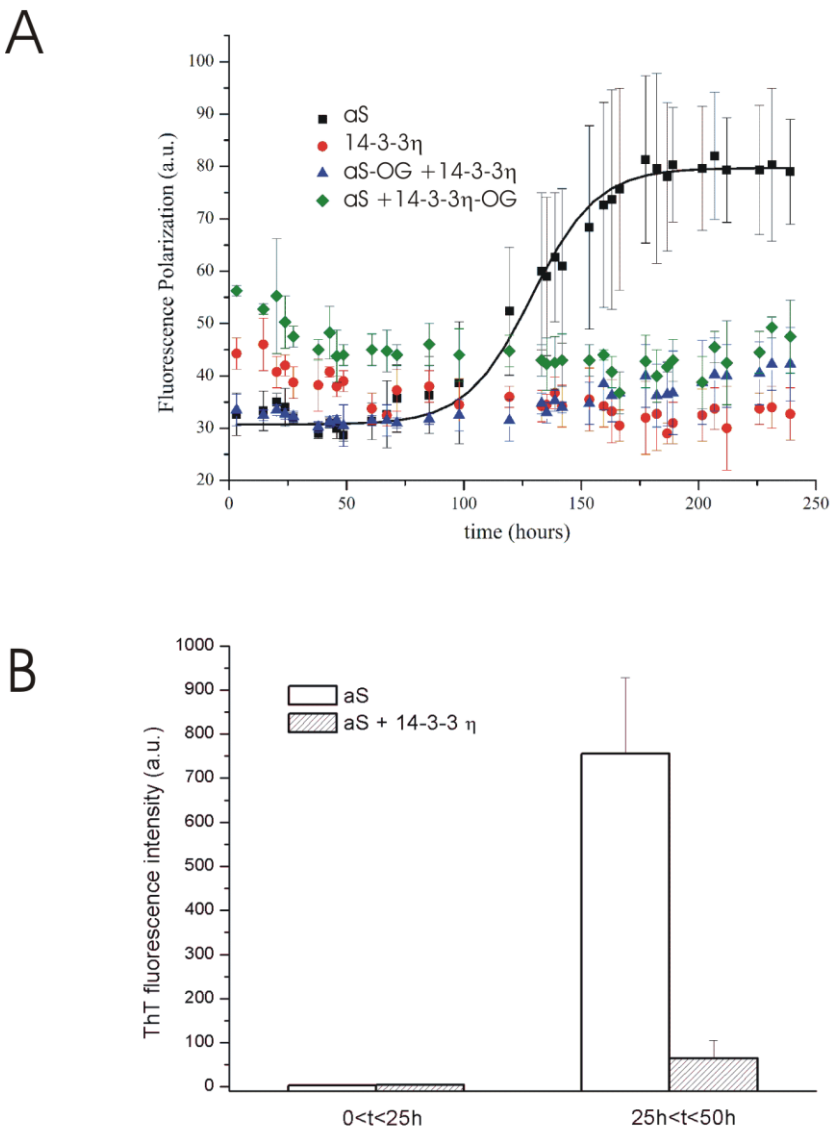

Figure 4.1 – A. Time course of aA aggregation process followed by FP of labeled aS 70 μM (black) and labeled 14-3-3 η 17.5 μM (red) as controls. FP of labeled aS 70 μM in presence of 17.5 μM 14-3-3 η (blue) and of aS 70 μM in the presence of 17.5 μM labeled 14-3-3 η (green). 14-3-3 η apparently inhibits aS fibrillization, while FP intensities increase with time when aS aggregates alone. FP values of aS monomers and 14-3-3 η dimers seem to be comparable within the errors.

However, we could not observe any significant increase in the FP value when aS aggregates in the presence of 14-3-3 η at 4:1 stoichiometric ratio. This result suggests that the 14-3-3 η hinders the formation of FP detectable aS oligomers. Identical results were obtained using either aS-OG or 14-3-3η-OG as fluorescent probes (Figure 4.1, panel A). The proceeding of the aggregation

process toward the formation of mature fibrils was monitored independently in a ThT assay. aS alone exhibited the expected behavior with the formation of ThT positive fibrils after 25 hours, whereas the addition of 14-3-3η (4:1 stoichiometric ratio aS/14-3-3η) resulted in a negligible increase in ThT fluorescence (Figure 4.1, panel B).

4.2 Alpha-synuclein and 14-3-3 η aggregation products and morphology

Based on these initial results, we decided to characterize not only the kinetic of the aggregation process, but also the aggregation products of aS:14-3-3 η by AFM. Previous studies indicated that aS and 14-3-3 proteins are capable of forming soluble 54-83 kDa complexes that were suggested to mediate dopamine-dependent neurotoxicity in cultured neurons (Xu *et al.*, 2002).

In our hypothesis, these complexes could go undetected because of their dimensions in the FP and ThT previous presented kinetic assays, but not in a fine characterization performed by AFM. aS alone leads to the well characterized mature fibrils, with the expected distribution of height values (Figure 4.2, top raw), while a 4:1 stoichiometric ratio of aS:14-3-3 η resulted in homogenous distribution of "curved objects" with a mean height of 2 nm and a morphology profoundly different from that of the mature fibrils (Figure 4.2, bottom raw). A detailed analysis of the AFM images allowed a precise characterization of the curved objects: by sampling different aS:14-3-3 η stoichiometric ratios, it was possible to correlate this parameter to both height and curvature of the end products. Incubation of aS with increasing amounts of 14-3-3η resulted in a shift toward a new population of curved objects significantly smaller in term of diameters than fibrils (Figure 4.2). In Figure 4.2 and Table 4.1 is reported the trend of both aS aggregates heights (middle column) and curvatures (right column) as a function of 14-3-3η relative concentration.

Moreover, this approach allowed to determine the aS:14-3-3η molar ratio of 30:1 as the minimal relative concentration of 14-3-3η required to achieve a detectable effect. These results were confirmed independently by TEM analysis, where the curved objects where compared to the canonical aS fibrils (Figure 4.3).

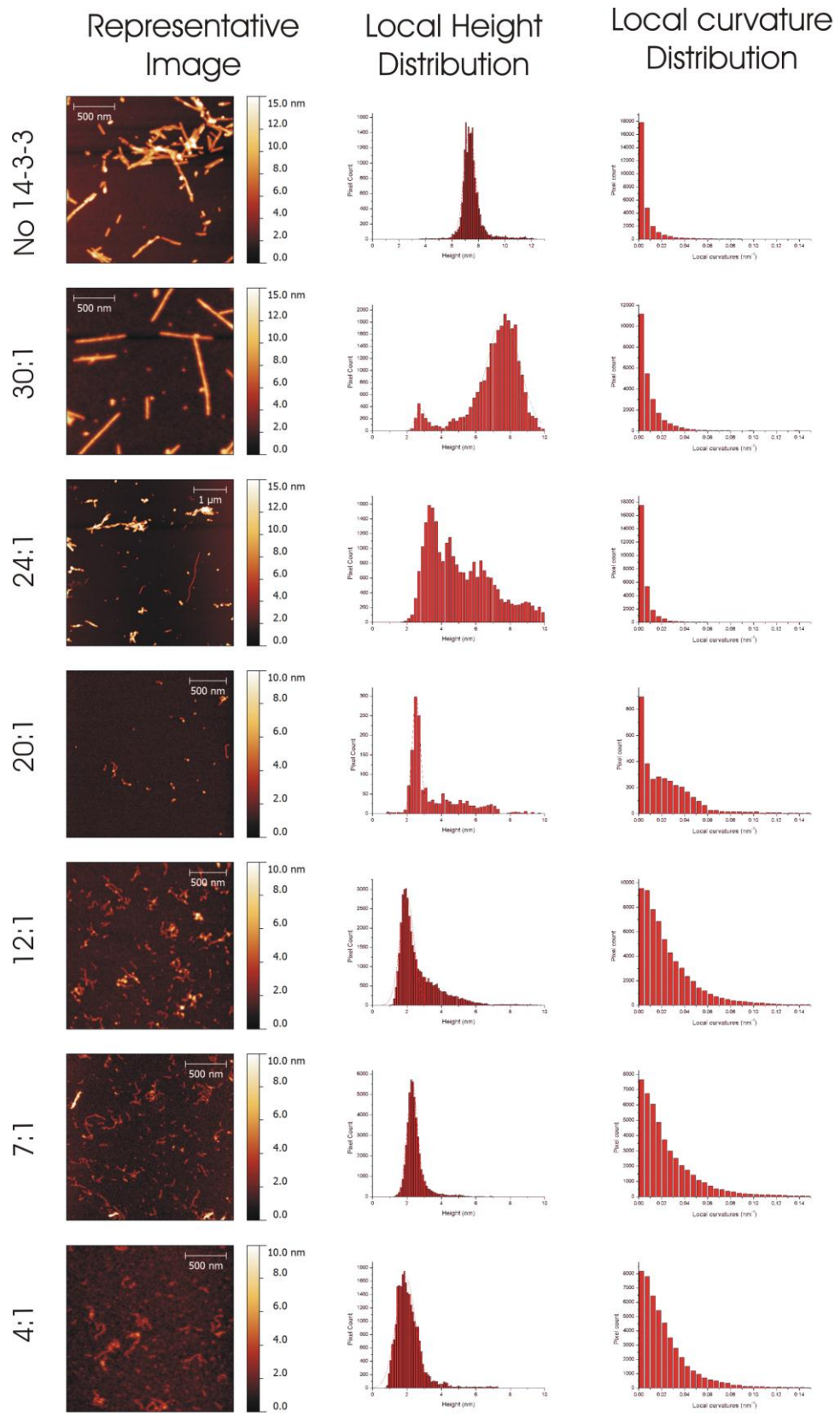

Figure 4.2 - AFM studies on morphology of aA aggregates, that are curved objects with smaller diameters compared to aS canonical fibrils in presence of 14-3-3 η with respect to different 14-3-3 η concentrations. Mean heights decrease with the increase of 14-3-3 η concentration, while mean curvatures of the curved objects increase with the chaperone concentration.

	No 14-3-3η	30:1	24:1	20:1	12:1	7:1	4:1
Heights (nm)	**7.3**	**2.8/7.6**	**-**	**2.5**	**2.0**	**2.3**	**1.9**
Standard deviation (nm)	**0.9**	**0.6/1.9**	**-**	**0.5**	**0.8**	**0.6**	**1.1**

Table 4.1 – Average heights estimated though a Gaussian fit of the distribution of heights derived from AFM images corresponding to the Figure 4.2. The values show the effects on aS fibrils heights as a function of 14-3-3 η relative concentration. The stoichiometric ratio aS: 14-3-3 η equal to 24:1 gave a distribution of heights to broaden to be fitted with a Gaussian, while the 30:1 showed a double peak, ascribed at least to two different species.

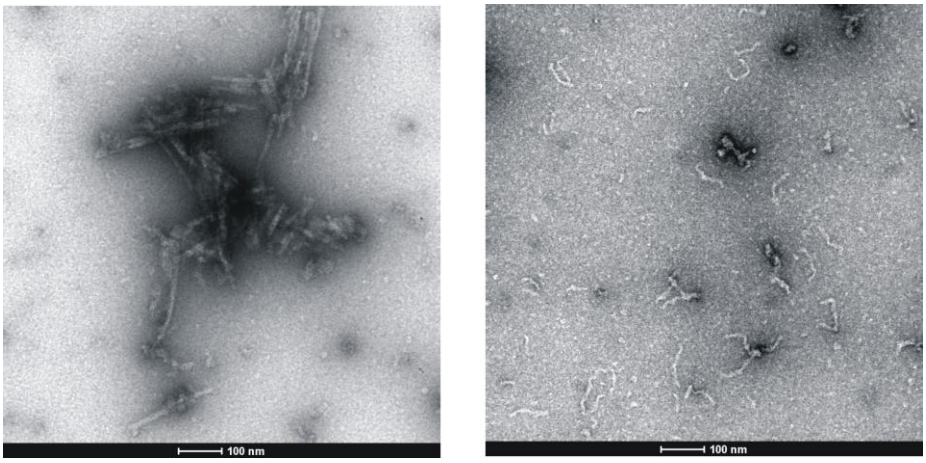

Figure 4.3 - TEM images of aS fibrils (on the left) and curved objects (on the right) obtained respectively aggregating aS alone or in the presence of 14-3-3 η (4:1 stechiometric ratio). The AFM results are confirmed by an independent technique.

We further characterized these curved objects using immunogold labeling. We asked whether the effect of 14-3-3 η on aS aggregation was due to a transient interaction or a stable binding between the two proteins. The observed homology between aS and 14-3-3 η did not result in cross reactivity of the 14-3-3's antibody toward aS. Instead, 14-3-3 η in solution could be efficiently detected by TEM using anti-14-3-3 η antibody and dimeric gold particles could be occasionally detected (Figure 4.4, panel A). As shown in figure 4.4, panel B, immunogold with anti-14-3-3 η of the aS:14-3-3 η aggregates revealed the highly specific placement of the gold nanoparticles on the curved objects, clearly indicating that the chaperone associates with aS to form novel oligomeric species.

To investigate the secondary structure of the curved aS aggregates, after ThT assays, we used circular dichroism (CD). However, no information on the

aS component could be obtained from the CD spectra being the signal from aS aggregates significantly weaker compared to the intensity of 14-3-3 η associated alpha-helical contribution. However, these data indicate that the 14-3-3 η within the curved aggregation product maintains its folding.

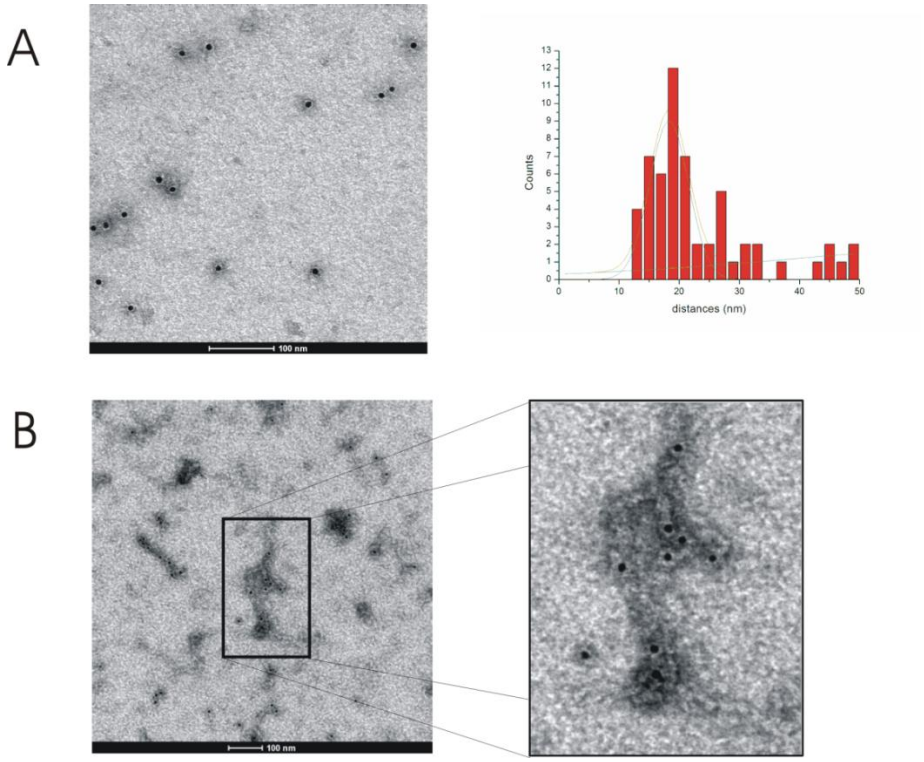

Figure 4.4 – A. Immuno-TEM images of 14-3-3 η dimers in solution, where the gold nanoparticles represent a 14-3-3 η molecule. The graph (on the right) shows the distances distribution in at least 10 images and highlight the presence of a peak corresponding to a plausible distance for a dimeric 14-3-3 molecule considering also the contribution due to the antibodies.
B. Curved objects obtained aggregating aS in the presence of 14-3-3 η (stoichiometric ratio 4:1) imaged by immuno-TEM: the gold nanoparticles representing the chaperone molecules are on the aggregates, suggesting the formation of a stable complex.

4.3 14-3-3 η effects on alpha-synuclein mature fibrils and seeding the aggregation with seeds in the presence of 14-3-3 η

As previously mentioned, there is a lack of evidence of an interaction between aS and 14-3-3 η *in vitro*. The interaction, at least from our experiments, seems to involve oligomeric aS during the aggregation process. To evaluate a further possible interaction between fibrillar aS and 14-3-3 η, this isoform was added to preformed mature fibrils and samples were studied by AFM. As shown in Figure 4.5, the addition of a 1:4 molar excess of 14-3-3 η to aS fibrils does not cause fibrils fragmentation or modify the morphology toward the curved object one, neither immediately nor after 72 hours of incubation. Therefore, we inferred that 14-3-3 η is not likely to interact with mature fibrils and aS aggregation process is not reverted by 14-3-3 η once the mature fibrils are already formed.

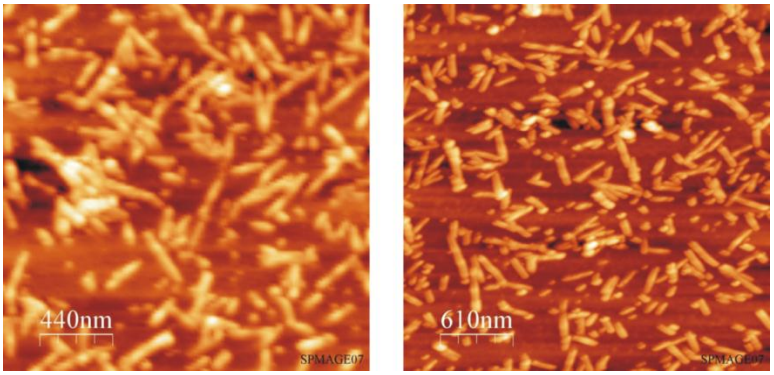

Figure 4.5 - AFM micrographs of aS mature fibrils incubated with a 1:4 molar excess of 14-3-3 η and observed immediately (on the right) or after 72 hours (on the left): no changes seem to occur because of the presence of the chaperone in aS fibrils characteristics.

To evaluate if the interaction may also occur at later stages of the aggregation process, we analyzed the process of fibril elongation in the presence of 14-3-3 η starting from preformed aS seeds (Wood *et al.*, 1999). The latter, are prepared by sonication of mature aS fibrils and act as nucleation centers for fibril growth (as reported in section 2.3.5 and discussed in chapter 3). Importantly, the sonication conditions affect the nature of the seeds obtained: AFM analysis allowed to classify seeds into two different types based on their

morphology, quantified as mean diameters: protofibrils fragments, with a diameter that is about 5 nm (type 1) and mature fibrils fragments, with an average diameter of 7 nm (type 2) (Figure 4.6).

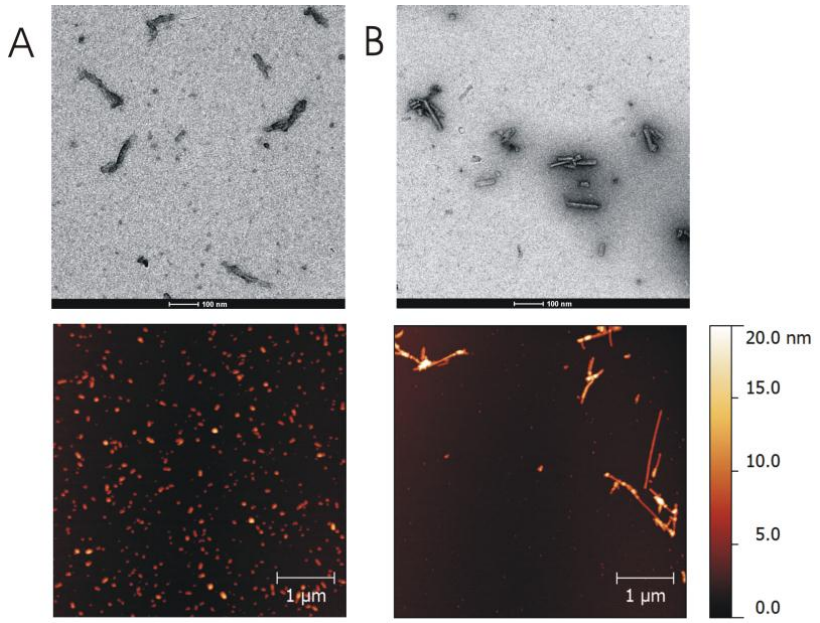

Figure 4.6 – A. Protofibrillar seeds (A) and fibrillar seeds (B) imaged by TEM (top) and AFM (bottom). The main different that is qualitatively evident from AFM images is the smaller length and diameters of the protofibrillar seeds compared to the fibrillar one. The quantification of this different was complicated by the presence of fragments of proteins due to the sonication that prevented the use of the available automatic recognition tool.

The impact of 14-3-3 η on aS aggregation was then analyzed in the presence of the different types of seeds. As showed by Giehm and co-workers, seeds act on the aggregation process by shortening the lag phase and increasing the slope of the rising part of the sigmoid growth of fibrils kinetic (Giehm *et al.*, 2011). Both protofibrillar and fibrillar seeds rapidly lead to the formation of µm long mature fibrils when added to aS aggregation assays, but the line shapes of the aggregation curves are different when 14-3-3 η is added to the mixture if we look at the obtained aggregation products.

In our experiments, protofibrillar seeds (type 1) were less effective in promoting aS aggregation if 14-3-3 η was present, suggesting that the chaperone can only hinder aS fibril elongation (Figure 4.7, panel A). On the contrary, fibrillar seeds (type 2) lead to the formation of mature fibrils comparable to the

one obtained in the absence of 14-3-3 η even in the presence of 14-3-3 η (Figure 4.7, panel B).

Furthermore, performing immuno-TEM experiments on these aggregates we found that 14-3-3 η molecules were sequestered by the aggregation products leading to fibrils that include 14-3-3η molecules (Figura 4.7, panel C). We calculated the gold nanoparticles distances distribution and could not observe the presence of dimeric 14-3-3 η (Figura 4.7, panel D). At this stage we cannot tell if this is either due to steric hindrance of the fibrils, which prevented the epitope-antibody recognition, or to the different, non-dimeric conformation of 14-3-3 η within the aggregates.

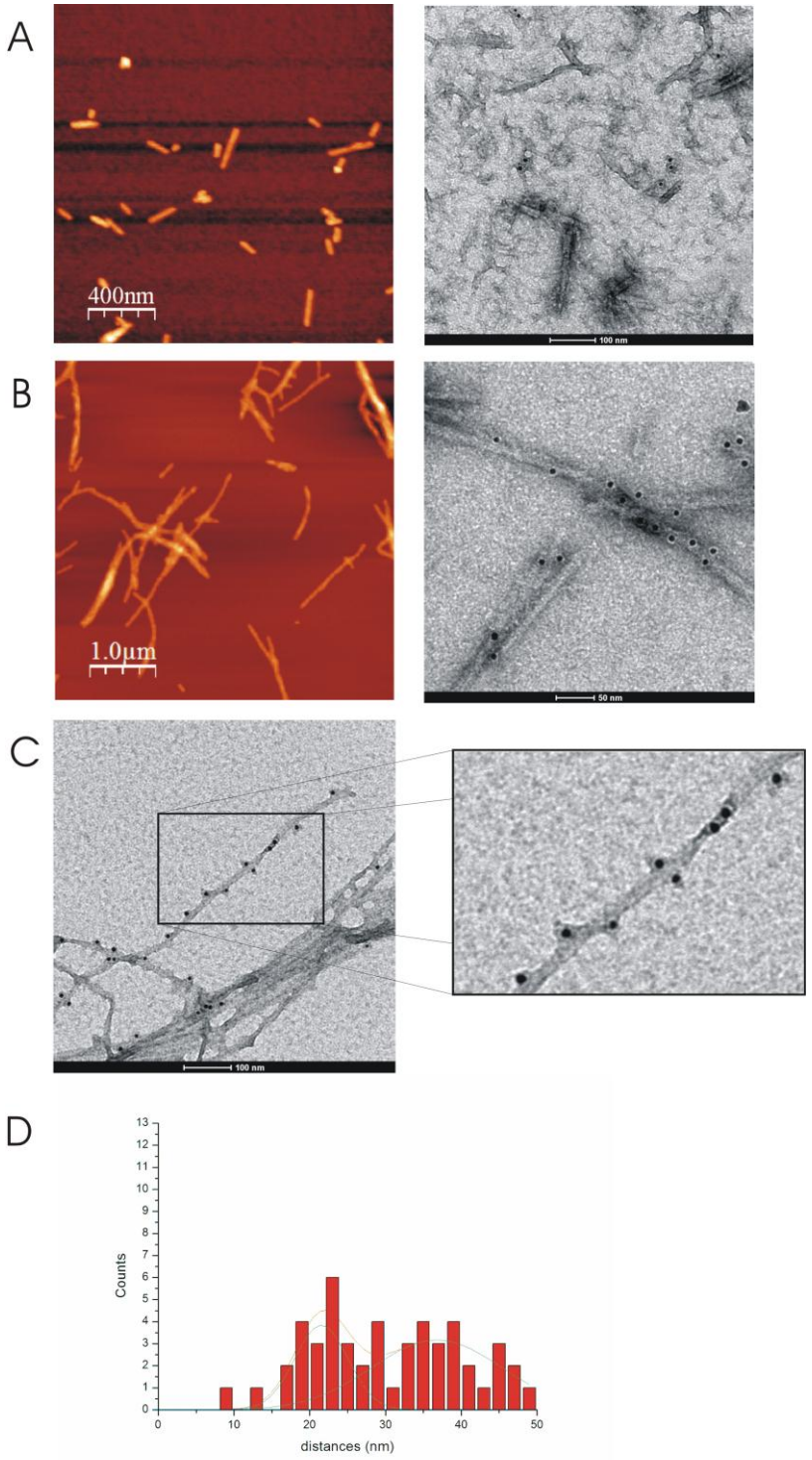

Figure 4.7 - AFM and immuno-TEM micrographs of aS aggregation products of an aS aggregation assay promoted by the presence of two types of seeds (type 1 -protofibrillar- in panel A and type 2 -fibrillar- in panel B) in the presence of 14-3-3 η (4:1 stechiometric ratio). While the presence of 14-3-3 η when aggregation is promoted by type 1 seeds hampers fibrils formation (panel A), type 2 seeds promote fibrils formation even in the presence of the chaperone-like protein. C. 14-3-3 η molecules represented by gold nanoparticles can be seen by immuno-TEM and remain trapped into the fibrils, but the nanoparticle distances distribution does not assess if 14-3-3 η is present as a dimer or as a monomer.

4.4 Specificity of η isoform effect on alpha-synuclein aggregation compared with the other 14-3-3 isoforms

Several studies propose the family of 14-3-3 proteins to be involved in PD because of their presence in LBs (Kawamoto *et al.*, 2002; Berg *et al.*, 2003; Umahara *et al.*, 2012), their capability of interacting with different PD related proteins (Li *et al.*, 2011; Sato *et al.*, 2006) and their ability to rescue toxicity in PD models (Yacoubian *et al.*, 2010; Slone *et al.*, 2011). However, several of the different isoforms were shown to be somehow involved at least in one of these processes, without giving any hints about the specificity of the involvement of the single isoform.

For this reason and to verify is the effect we are observing is specific for η isoform, we performed AFM imaging on the aS aggregation products in the presence of the other six 14-3-3 isoforms. A representative AFM image for each isoform, along with the heights distribution of the obtained aggregates, is reported in Figure 4.8, From the images and the diameters evaluations reporter in Table 4.2, it is clear that among the 14-3-3 proteins only η and τ induce the formation of curved objects instead of canonical fibrils. Moreover, γ isoform lead to the formation of objects whose average diamters corresponds to the one of protofibrils.

	No 14-3-3η	**β**	**γ**	**ε**	**η**	**ζ**	**σ**	**τ**
Heights (nm)	**7.3**	**7.3**	**4.7**	**7.6**	**2.5**	**7.5**	**7.8**	**2.5**
Standard deviation (nm)	**4.1**	**3.7**	**1.7**	**1.4**	**1.2**	**1.9**	**5.2**	**1.2**

Table 4.2 – Average heights of fibrils or curved objects obtained aggregating aS and the different 14-3-3 isoforms. The larger standard deviations compared to the one reported in Table 4.1 are due to the less consistent statistics.

The results reported here suggest that the effect exerted by 14-3-3 η is partially specific and dependent on specific structural features of this isoform. However, at this stage is difficult to speculate more on the observed specificity.

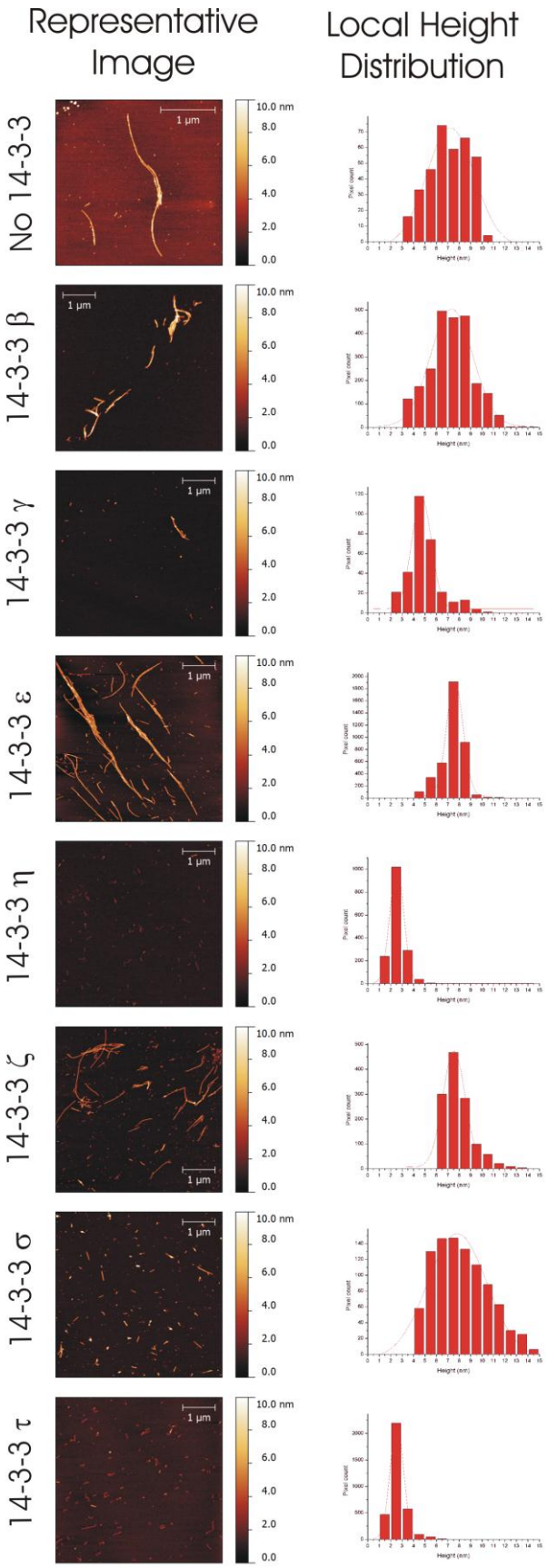

Figure 4.8 – Panel of AFM micrographs of aS aggregation products in the presence of different 14-3-3 isoforms and relative local heights distribution.

4.5 Effects of 14-3-3 η on alpha-synuclein aggregation in cells

To evaluate whether the effects of 14-3-3 η on aS aggregation *in vitro* can be extended to a cellular contest, aS was overexpressed in HEK293 cells. Since aS overexpression by itself does not lead to the formation of large inclusions, we also reproduced the aS aggregation cellular model that was described in Section 3.1, in which aS fibrils formation was triggered by the presence of seeds introduced in cells overexpressing aS. After obtaining two different aS aggregation models (one for the study of the early aggregation steps and the other for the study of LBs-like inclusions formation), we overexpressed 14-3-3 η to investigate the effect of the chaperone on aS cellular phenotypes or inclusions characteristics. To make sure that the majority of cells overexpressing aS-EGFP was co-transfected with 14-3-3 η, we tested different 14-3-3 η:aS-EGFP plasmid ratios using immunocytochemistry, and chose the one that lead us to have a very high level of coexpression (about 90% for a DNA ratio of 3:2).

Figure 4.9 shows confocal microscopy images of cells overexpressing aS-EGFP and 14-3-3η in the absence or in the presence of exogenous aS seeds. 14-3-3η co-localized with aS-EGFP in the cytoplasm, as expected, and could be also present in the aggregates formed after seeds triggering of aggregation (Figure 4.9, panel B). However, the limited resolution of confocal microscopy does not allow comparing the state of aS aggregation at the oligomeric level in the presence of 14-3-3 η with respect to cells where only aS-EGFP was overexpressed (Figure 3.2). Therefore, we cannot rule out an interaction between oligomeric aS and 14-3-3η using this method. Sato *et al.*, (2006) previously reported a strong interaction in HEK293 cells between the two proteins, using co-immunoprecipitation. However, co-immuniprecipitation cannot provide information on different possible aS oligomeric state. Further studies are needed to highlight the proposed interaction between aS oligomers and 14-3-3 η in cell models.

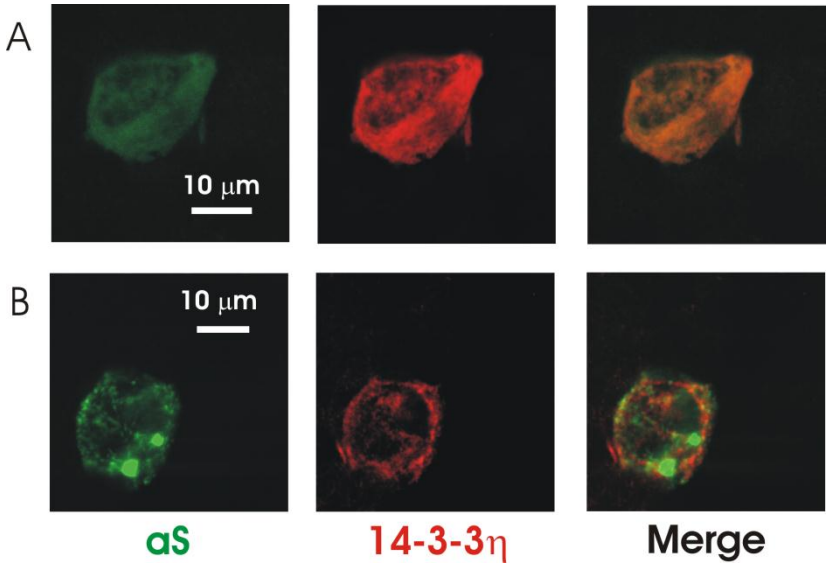

Figure 4.9 – A. HEK293 cells overexpressing aS-EGFP and 14-3-3 η and (B) overexpressing aS-EGFP and 14-3-3 η, and treated with seeds. 14-3-3 η was immunostained with polyclonal antibody against 14-3-3 proteins and a secondary antibody conjugated with Alexa Fluor 568). The green spots in panel B are aS aggregates, but a precise estimation of aggregates dimensions and amount is not feasible with conventional confocal microscopy techniques.

We next assessed whether 14-3-3 η overexpression is capable of preventing or reducing aS fibrils formation. As shown in figure 4.9, panel B, overexpression of 14-3-3 η does not lead to a rescue of aggregation when aS was overexpressed in the presence of exogenous seeds. The latter result seems to be in good agreement with TEM experiments of aS fibrils formed in the presence of seeds and 14-3-3 η *in vitro*. One possibility is that seeds are too efficient in recruiting other building blocks on the growing fibers to be affected by the chaperone-like activity of 14-3-3 η. We could hypothesize that it can be trapped in within aS-EGFP aggregates, as reported above for recombinant 14-3-3 η in seeds promoted aS fibrillation *in vitro* (Figure 4.7). The resolution limit of confocal microscopy, which is about 200-300 nm at this excitation wavelength, does not allow a fine morphological or dimensional comparison of aS-EGFP aggregates in the presence or absence of 14-3-3 η, that we know from AFM measurement are between 2 and 8 nm in diameter and hundreds of nm in length.

4.6 14-3-3 η effects on alpha-synuclein toxicity in cell models

Considering that the effect 14-3-3 η on the formation and on the dimensions of aS aggregates was difficult to quantify in cells and having in hand a robust cellular assay to monitor the toxicity of oligomeric and fibrillar aS, we next explored the effects of 14-3-3 η overexpression on aS-EGFP aggregation-mediated cellular toxicity.

We used a very easily approachable readout, i.e. the quantification of cell survival in the presence of 14-3-3 η, compared to control (EGFP transfected cells), after 12, 24 and 36 hours after aS-EGFP transfection, or aS-EGFP transfection and seeding (Figure 4.10).

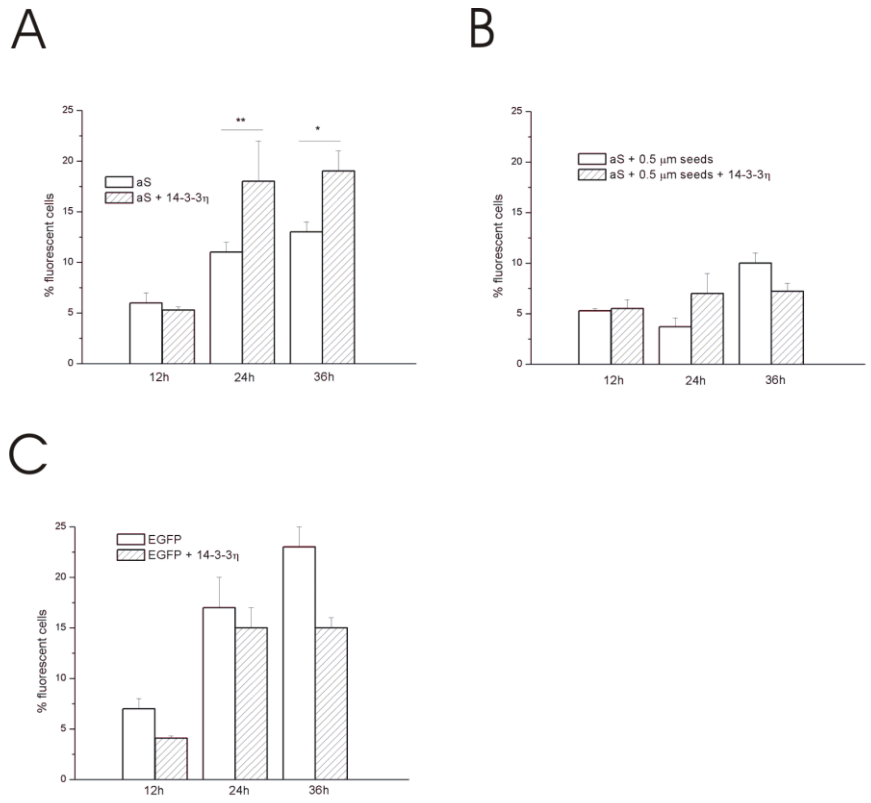

Figure 4.10 – Histograms representing the rescue due to 14-3-3 η overexpression in cells overexpressing aA (A) or overexpressing aA plus seeding (B), and EGFP, as control (C). Fluorescent cells, overexpressing aA-EGFP or EGFP, were counted after 12, 24 and 36 hours from transfection to evaluate cell viability in the presence or in the absence of 14-3-3 η overexpression. After 24 and 36 hours 14-3-3 η overexpression rescues aS toxicity; the rescue takes also place when seeds are present, but only after 24 hours. In the control there is no rescue due to 14-3-3 η overexpression.

We observed that overexpression of 14-3-3 η rescued aS mediated toxicity in cells overexpressing aS-EGFP, at 24 and 36 hours (Figure 4.10, panel A) (respectively p=0.002 and p=0.02 when tested with Student's test). On the

contrary, upon addition of seeds at the time of transfection, a statistically significant rescue effect was not detected neither at 24 hours nor at 36 hours (Figure 4.10, panel B). As expected, the EGFP transfected cells, used as control, showed no rescue due to the overexpression of 14-3-3 η (Figure 4.10, panel C).

4.7 14-3-3 η sequestration by fibrils in alpha-synuclein aggregation cell model

In a recent paper (Olzscha *et al.*, 2011), it was proposed that one possible toxic mechanism for amyloidogenic chimeric proteins could be related to their ability of sequestering essential proteins from cells cytoplasm during aggregation. aS aggregation triggered by seeds *in vitro* leads to the formation of aS fibrils also in the presence of 14-3-3 η molecules, which were sequestered into the aggregates, suggesting that also in this case a similar mechanism to the one proposed in the paper could occur.

To verify this hypothesis we overexpressed aS, 14-3-3 η and treated cells with seeds and checked the amount of soluble 14-3-3 η in the cell cytoplasm by Western Blot. As control, we used cells not treated with seeds.

Since 14-3-3 η plasmid encoded for the protein fused with GST, it runs in the SDS page at a higher molecular weight compared with the endogenous 14-3-3 proteins. Therefore, we were able to distinguish overexpressed 14-3-3 η from the endogenous 14-3-3 proteins when using an antibody against all the different 14-3-3 isoforms. As it is shown in figure 4.11, it is clear that when cells overexpressing aS are treated with seeds, a decrease in the amount of overexpressed 14-3-3 η is shown by Western Blot analysis. This result could mean that 14-3-3 η molecules are sequestered during aS aggregation by fibrils not only *in vitro*, but also in HEK293 cells.

In a parallel experiment the enzyme β-galactosidase (LacZ gene) was overexpressed along with aS (with or without seeds treatment), to verify the specificity of the sequestration in this experimental conditions. Unfortunately, probably because of the molecular crowding in the cell cytoplasm induced by proteins overexpression, we found that the same sequestration occurs also for this protein that is totally PD non-associated and not of our interest. The same result was obtained overexpressing EGFP or the PD related protein LRRK2.

For this reason this assay could not be used to verify overexpressed 14-3-3 η sequestration in cellular model in a specific manner.

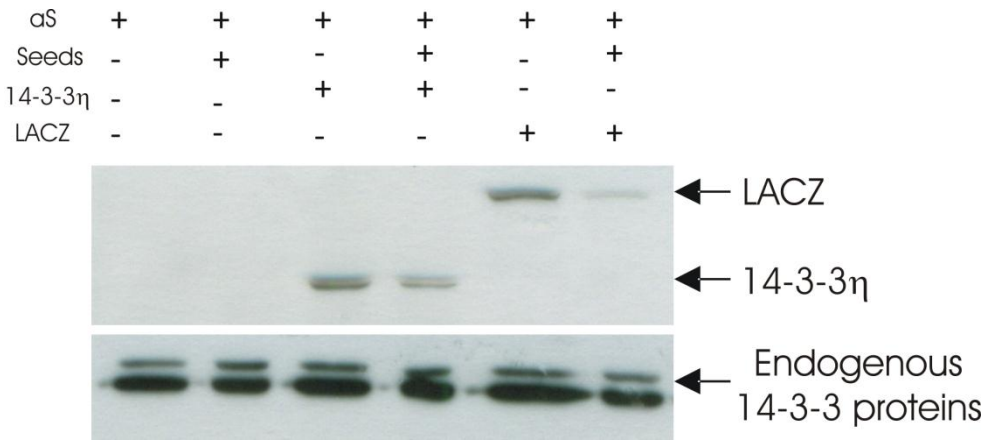

Figure 4.11 – Western blot against LacZ and 14-3-3 η in cells overexpressing aS and LacZ or 14-3-3 η, or treated also with seeds. In cells treated with seeds a decrease in the soluble fraction of both LacZ and 14-3-3 η can be seen, meaning probably that overexpression lead to molecular crowding that induces an aspecific protein sequestration.

Therefore, we decided to look at the sequestration of endogenous 14-3-3 η by Western Blot using a specific antibody against this isoform. We first checked the specificity of the antibody for this isoform using the recombinant 14-3-3 proteins and the presence of the η isoform in a detectable amount in HEK293 cell line.

Then seeds in different concentration (0.1, 0.25, 0.5 and 0.75 μm) were used to trigger the aggregation in cells overexpressing aS. The idea was to see if different concentration of seeds could lead to an increased aggregation and to an increased sequestration of 14-3-3 η.

Looking at the amount of 14-3-3 η in the cell cytoplasm in the different samples, compared to the control and to cells overexpressing aS, we found that 14-3-3 η expression in HEK293 was increased in cells only overexpressing aS.

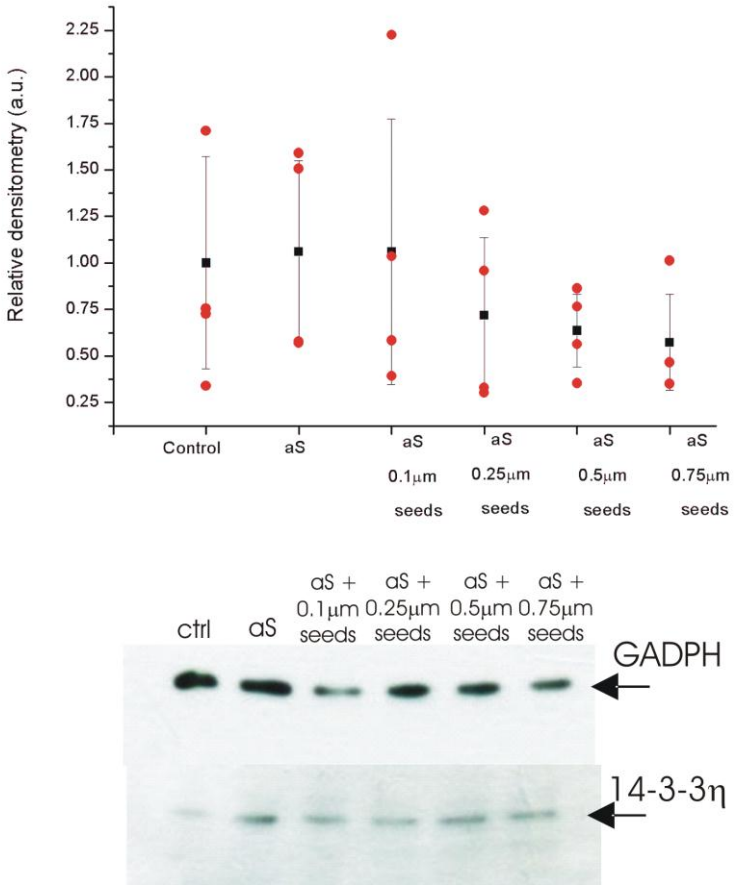

Figure 4.12 - Relative densitometry graph and western blot representing the expression level of endogenous 14-3-3 η with respect to GADPH, for cells overexpressing aS or/and treated with different amount of seeds. The variability in the results is probably due to the experimental conditions and to the method, but still a trend showing a decrease in soluble 14-3-3 η present in cell cytoplasm can be seen as a function of the amount of seeds used for the treatment.

This result is in good agreement with some experiments published recently on 14-3-3 proteins regulation in an A53T mice model (Kurz *et al.*, 2012).

When also seeds are introduced, the trend of densitometry analysis shown in figure 4.12 suggests that there is a decrease in 14-3-3 η amount present in the cell cytoplasm with respect to the increased concentration of seeds. However, repeating the experiment several times (n=4), it turned out that the decrease is not statistically significant, as it is clear from the histogram in figure 4.12 and was evaluated by Student's test. The reason has to be found in the variability of the method used to detect 14-3-3 η amount in this experiment. Moreover, there are probably two competing mechanisms in the induced

variation of 14-3-3 η expression in these cell models for aS aggregation. The first one is the up-regulation of 14-3-3 η due to aS overexpression, while the second one is the sequestration of chaperone molecules into the aggregates.

4.8 14-3-3 η and alpha-synuclein interaction in cell models

Sato and co-workers proposed that aS and 14-3-3 η can interact in cell models but not *in vitro* because of modification(s) that do not occur to recombinant proteins (Sato *et al.*, 2006). They proved the interaction by co-immunoprecipitation but not in live cells.

For this reason and to verify the interaction of the two proteins in our cellular model we overexpressed aS-EGFP and 14-3-3 η-dsRED in HEK293. We used cross-RICS to point out the presence of a complex constituted by the two proteins and cross-N&B method to evaluate its stoichiometry.

A representative image of cells transfected with both aS-EGFP and 14-3-3η-dsRED is shown in Figure 4.13, panel A. To perform RICS analysis we needed a more zoomed-in image to reach the 50 nm pixel size necessary to obtain significant information of the interaction between the two proteins (Figure 4.13, panel B).

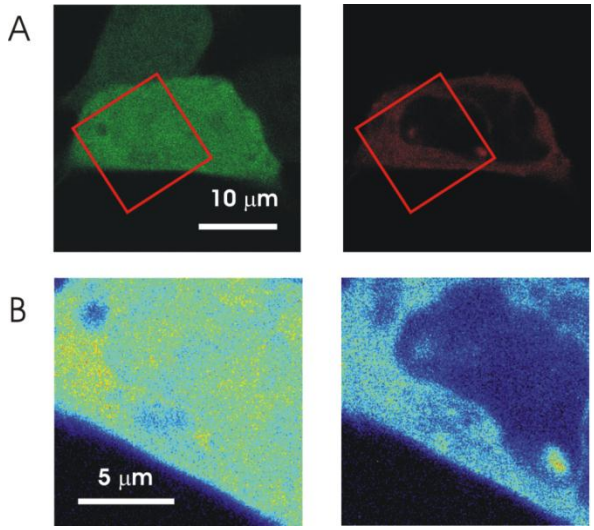

Figure 4.13 – A. Confocal images of HEK293 representative cell overexpressing aS-EGFP and 14-3-3 η-dsRED.
B. Particular of the cell presented in the panel B, on which cross-RICS and cross-N&B analysis were performed (color scale, a. u.).

Cross-RICS map of aS-EGFP and 14-3-3η-dsRED is shown in Figure 4.14 (panel A), where the colored peak in the center of the image represents the presence of an interaction between the two proteins. On the contrary, the cross-RICS map of EGFP and dsRED calculated as a control is completely flat, meaning that no interaction occurs in this model between the two (Figure 4.14,

panel B). This result was also found for the other controls we performed, i.e. co-expression of aS-EGFP and dsRED and co-expression of EGFP and 14-3-3η-dsRED.

In Figure 4.14, panel C, we reported a tridimensional representation of the RICS map corresponding to the one shown in panel A and the associated 3D fit. Fitting this curve leaded to the estimation of the diffusion coefficient D for the complex constituted by aS and 14-3-3 η. Repeating this estimation for different cells (n=10) in 3 different experiments allowed the calculation of the average diffusion coefficient of the complex that is D=0.47±0.05 $\mu m^2/s$.

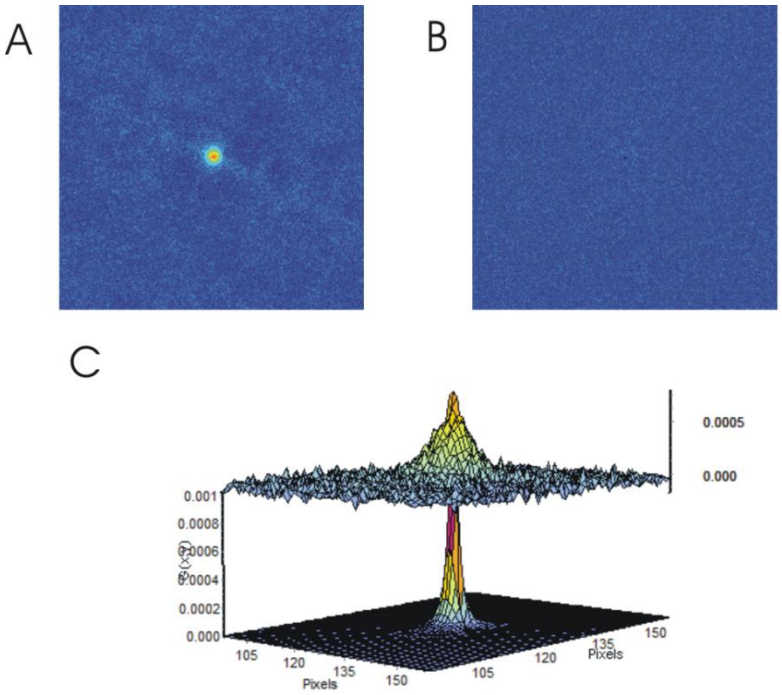

Figure 4.14 –Representative cross-RICS maps of a cell overexpressing both aS-EGFP and 14-3-3 η-dsRED (A) or both EGFP and dsRED (B). The presence of the peak in the first map, whose tridimensional representation is reported in panel C, means that an interaction occurs. The fit of the 3D plot gives information about the diffusion process of the aS/14-3-3 η complex.

Interestingly the diffusion coefficients around this value usually account for membrane bound proteins or very large complexes.

Since aS membrane binding propensity is very well known (Davidson *et al*., 1998; Bartels *et al*., 2010), a possible explanation is that the interaction occurs only between membrane bound aS, which acquires an alpha-helical structure, and 14-3-3 η in the cytoplasm. Another possibility is that a large macromolecule is formed in the cytoplasm, because 14-3-3 η molecules (and 14-

3-3 proteins in general) are able to bind more than one protein. In this situation all the non-fluorescent proteins go undetected and therefore we are not able to asses, only from analysis, which hypothesis is the correct one.

However, further analyses on these data were performed to obtain more information on the stoichiometry of the formed complex and on its localization.

Cross-N&B method was used and cross-Brightness B_{CC} was calculated for cells that showed an interaction between aS and 14-3-3 η, when RICS analysis was performed.

Panel A in Figure 4.15 shows B_1-B_2 plot that presents all the possible brightnesses found in the image for the two different channels (and therefore for the two different proteins), corrected with a detrend filter that removes the contribution to the fluctuation due to slow movements. The red cursor position in the plot corresponds to the brightnesses of the monomeric EGFP and monomeric dsRED previously calibrated with the same method used for single channel N&B analysis (B_{EGFP}=1.51±0.09 and B_{RFP}=1.19±0.08). In the selection map (Panel A, on the left), pixels corresponding to those brightnesses are shown in the sample cell.

However, B_1-B_2 plot does not give any hints about the formation of complexes: to obtain this information we calculated the B_{CC} maps (Figure 4.15 panel B) for the chosen representative cell versus B_1 or B_2. B_{CC} map is slightly asymmetric, showing positive cross-variance and suggesting that at least in some regions the two proteins form complexes with a defined stoichiometric ratio.

The red cursors allowed selecting the points with a positive cross-correlation in the BCC map to show which are the pixels giving this signal in the selection map (Figure 4.15, panel B, on the right). As it is clear, most of the pixels showing positive cross brightness, which are the one presenting aS/14-3-3η complexes, are located at the cellular membrane. This result suggests that the interaction in the cellular environment can occur mainly at the membranes, where aS acquires an alpha-helical conformation that may promote the binding between the two proteins. The purification of 14-3-3 η from synaptic membranes from rat brain (Martin *et al.*, 1994) and aS association to membranes at the presynaptic terminal reported in the literature further support this possibility.

Plotting aS-EGFP brightness and 14-3-3 η-dsRED brightness in unit of monomer brightness lead to the construction of the stoichiometry map shown in Figure 4.16. Channel 1 axis shows the B value for aS, while channel 2 axis report the 14-3-3 η brightness; in the z axis, each color represent the number of pixels that shows that pair of B values (color scale from light blue – few pixels- to red -many pixels-). The most populated region is the one corresponding to the maximum of the peak, which is located in position (0.99, 1. 58) for this cell. Averaging on several different cells (n>10) in 3 different experiments lead to the evaluation of the average stoichiometric ratio for the complex formed by the two proteins, that is 14-3-3 η:aS =(1.5±0.3):(0.9±0.1). 14-3-3h is tipically dimeric, therefore we suggest that the interaction occurs between this dimer and aS monomer at the cellular membrane. The reason why the estimation for the number of 14-3-3 η monomers constituting the complex is lower than two is probably due to the presence of endogenous 14-3-3 η molecules that can contribute to the formation of the complex but are completely undetectable by cross-N&B analysis.

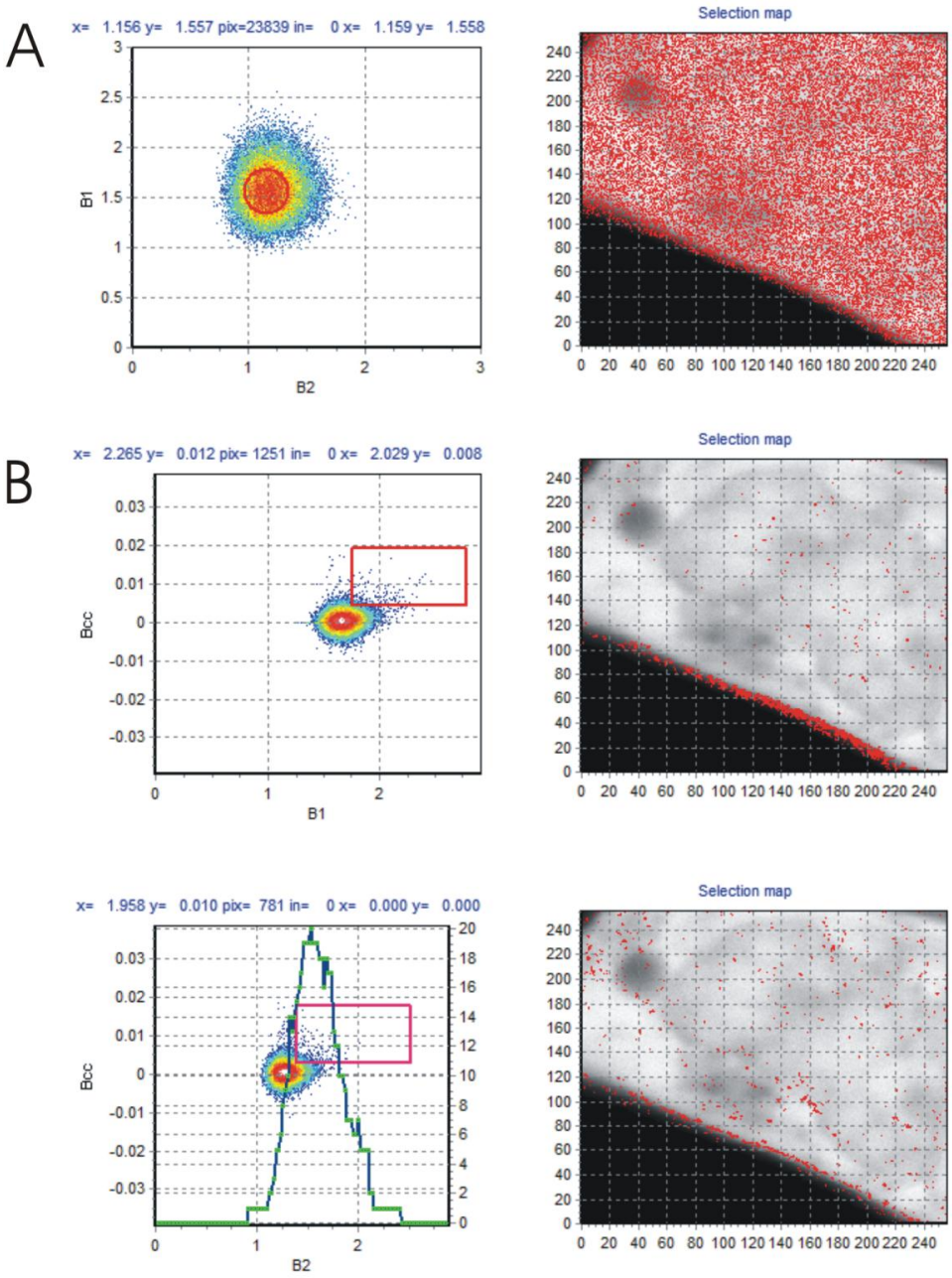

Figure 4.15 – A. B_1-B_2 map for a cell overexpressing both aS-EGFP and 14-3-3 η-dsRED. In the selection map on the right the pixels in red are the pixels corresponding to the aS and 14-3-3 η monomers selected through the cursor in the B_1-B_2 map.
B. B_{CC} versus B_1 and B_2 maps. In the selection maps on the right the pixels in red are the pixels corresponding to the aS and 14-3-3 η complexes selected through the rectangular cursors in the asymmetric part of the relative B_{CC} map. The localization clearly indicates that the complexes are mainly stacked at the plasma membrane.

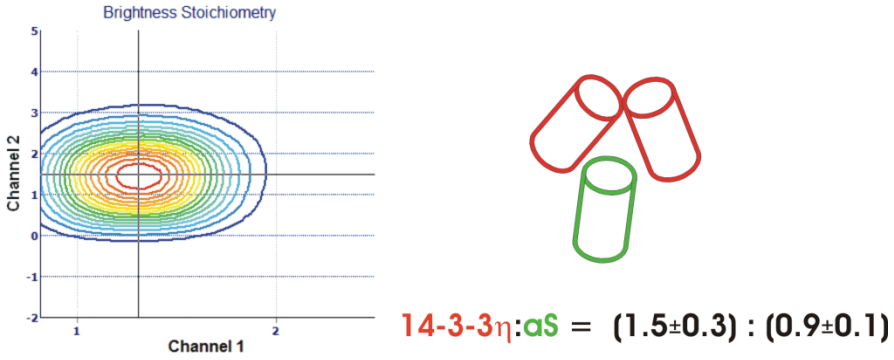

Figure 4.16 – Stoichiometry map of the complexes detected by N&B method in cells overexpressing aS-EGFP and 14-3-3 η-dsRED. The map shows that a complex constituted by 2 molecules of 14-3-3 η (a dimer) and a single aS molecule is present in these cells.

4.9 Conclusions

The results presented in this chapter show how 14-3-3 η is able to interfere with aS aggregation process *in vitro*, probably interacting with aS oligomeric species, and leads to the formation of curved aggregates. These objects cannot be seen with the techniques available to us in cells overexpressing the two proteins.

However, 14-3-3 η overexpression in cells overexpressing aS leads to a rescue of the aS induced toxicity. We demonstrated that 14-3-3 η can interact with aS in live cells, mainly at the plasma membrane, and probably this is associated to the reduced cell death that we observed.

The presence of 14-3-3 h in aS aggregation assays triggered by seeds does not lead to any variation in the end products of the aggregation and amyloid fibrils that form in this case can sequester 14-3-3 η molecules. Overexpressing 14-3-3 h in cells in which aggregation is triggered by seeds does not cause any rescue in the induced toxicity and can lead to the sequestration of the molecular chaperone, too.

Chapter 5

Discussion

“Remember to look up at the stars and not down at your feet. Try to make sense of what you see and wonder about what makes the universe exist. Be curious. And however difficult life may seem, there is always something you can do and succeed at.
It matters that you don't just give up.”

Stephen Hawking

The results presented in this thesis are summarized in the schema below, which will be use as line of reasoning in the discussion.

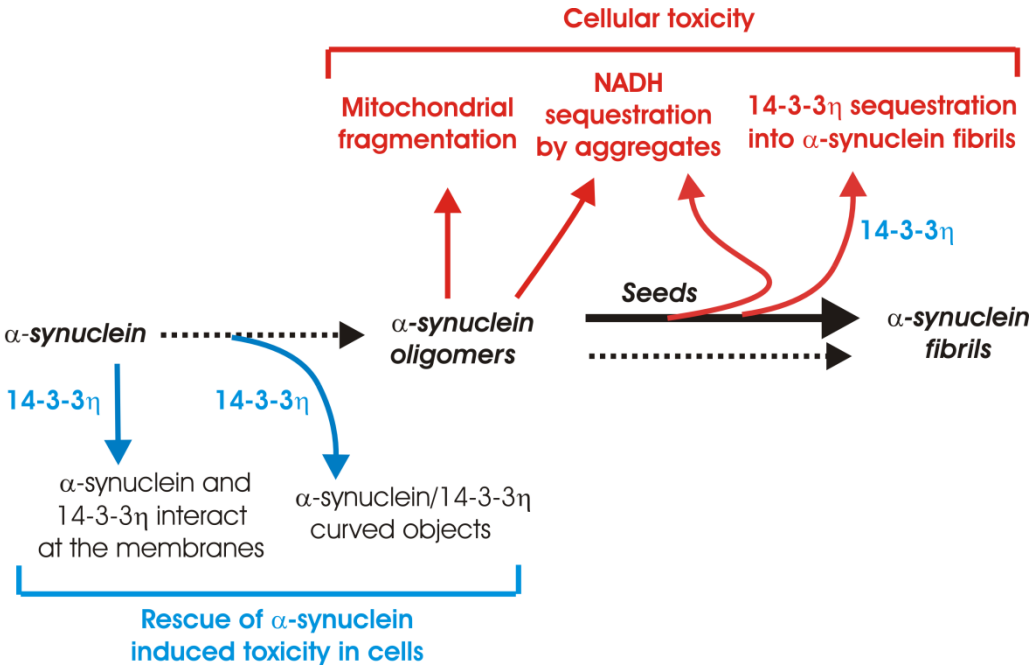

Schema 1.1 – aS oligomers were found in SH-SY5Y and HEK293 cells overexpressing aS: they induce cellular toxicity probably damaging mitochondrial membrane and inducing mitochondria fragmentation. We showed that aS oligomerization, but also the presence of aS fibrils or inclusions in cell cytoplasm, can affect NADH metabolism. This observation was done looking at the variation in the fluorescence properties (lifetime and emission spectrum maximum) of NADH in aS aggregation cell models and *in vitro*.
aS aggregated in the presence of 14-3-3 η lead to the formation of off-pathway aggregates, i.e. curved objects, that contain both the proteins and whose morphological characteristics depends on the amount of 14-3-3 η in the aggregation assay. Overexpressing the two proteins in HEK293 cells, we could not observe the formation of these complexes, but we measured a stable interaction between aS and 14-3-3 η that seems to occur at the membranes. Very interestingly, 14-3-3 η overexpression reduces cell death induced by aS overexpression.
The use of seeds to promote aS aggregation *in vitro* lead to a faster formation of aS fibrils, while in cells it cause the assembly of aS fibrils and inclusions in cell cytoplasm and an increased cellular toxicity. 14-3-3 η presence in the aS aggregation assay *in vitro* does not hamper aS fibrils formation if seeds are present and 14-3-3 η molecules are sequestered into amyloid fibrils. This sequestration occurs also in cells model, if aggregation is triggered by seeds. Considering the multiple cellular pathways in which 14-3-3 h is involved, this evidence supports the idea of an increase of the toxic effects ascribed to aS aggregation, due to the lowered level of functional and available 14-3-3 η in cell cytoplasm.

5.1 Alpha-synuclein aggregation in cell models

The two cellular models used to study aS aggregation in cells were chosen to characterize two different aspects of the aggregation process: the early stages when aS assemblies into oligomeric species, and the latest part of the process, i. e. the formation of LBs-like inclusions. To study of aS oligomerization the protein was just overexpressed and the process was analysed by monitoring the fluorescence fluctuation of the EGFP fused with the proteins (N&B method). This method provides information on the concentration and on the average dimensions of aS oligomers. In both SH-SY5Y and HEK293 cell lines aS overexpression lead to the formation of a heterogeneous ensemble of oligomeric species when the protein reached at least the average concentration of 80 μM. aS oligomers are constituted by about 6±4 monomers, that is in good agreement with the most recent results on aS aggregation intermediate dimensions obtained by Cremades and co-workers *in vitro* (Cremades *et al.*, 2012). Moreover, aS oligomeric species were partially sequestered into lysosomes, suggesting that ALP activation may be induced by these potentially toxic species. The presence of aS oligomeric species in lysosomes in this cellular model is in good agreement with the previously published work by Mak *et al.*, (2010) reporting the same mechanism active in a mice model. The idea that ALP starts to deal with oligomers that are potentially toxic was previously reported also by other groups (reviewed in Ebrahimi-Fakhari *et al.*, 2012).

A viability assay performed for this model, compared to EGFP transfected cells, showed that aS overexpression *per se* induce cell death. Therefore, we tried to identify a possible toxic mechanism of action for aS oligomers.

Looking at mitochondria, we found that mitochondrial morphology and distribution in cells showing aS oligomeric species were altered. Mitochondrial fragmentation was probably due to the interaction between oligomeric aS and mitochondrial membranes as previously proposed but not experimentally proved in cells, by Nakamura *et al.*, 2011.

The chance of observing aS oligomeric species in live cells is important because it allows the association of new or previously proposed toxic

mechanism(s) to aS oligomers, as we did for mitochondria. An issue remains open on the exact definition of the oligomeric aS. Among the several oligomers described in the literature, there are the oligomeric species found when aggregating aS *in vitro*, the oligomers that are found in the cells in pathological conditions and among those the oligomers that induce toxic effects and may be relevant to neurons death in parkinsonian brains. The oligomers we identified in our cell model are only one of the possible oligomeric species that aS can form; however, we believe that they are relevant considering their formation in a cellular milieu in live cells without any further treatment after aS overexpression.

N&B method of revealing aS oligomeric species could be used to test the effectiveness of compounds able to interfere with aS aggregation process and toxicity. The study of aS oligomers in a cellular environment is important also for the characterization of the species and the mechanism(s) responsible for PD spread. It is clear from the published results (Desplats *et al.*, 2009; Luk *et al.*, 2012) that there is a transfer of aS from unhealthy to healthy cells, but it has to be underlined the importance of the transmission not only of the misfolded material, but also of the associated structural information that probably causes the propagation of the aggregation process. N&B method, associated to particle tracking fluorescence techniques (Digman and Gratton, 2011) could be used to track the oligomers and the information that they carry, to develop possible therapeutic strategies based on the interference with the spreading mechanism.

The second model provided a way to study LBs-like pathology in the cellular environment: simple aS overexpression does not lead to the formation of aS fibrils or large inclusions, whose assembly has to be triggered by the introduction, along with aS DNA during the transfection, of recombinant aS fibrils fragments in the cellular cytoplasm. This idea was first proposed by Luk *et al.*, (2009) and the method allows the characterization of the final steps of the aggregation process. The same cell viability assay proposed for the cellular model discussed above showed that cell death under these conditions is even increased, probably as a result of multiple cell death mechanisms activated by aS overexpression and seeds introduction. The two of them could induce both aS fibrils formation, as shown by the data presented here and previously by other

groups (Luk *et al*., 2009; Danzer *et al.*, 2009; Waxman *et al*., 2010), and oligomerization, mainly in those cells where seeds uptake is limited, but probably in all cells in which aS is overexpressed and a threshold concentration needed for self-assembly is reached. This results in a combined effect due to aS oligomers and larger aggregates that induce respectively apoptosis and necrosis (Nonaka *et al*., 2010).

Considering the damages to mitochondria observed in the presence of aS oligomers in live cells, we hypothesized that NADH metabolism could be impaired in those cells. To quantify the differences in NADH metabolism in these two cell models compared with a control, we measured the variation of NADH fluorescence lifetime in live cells using the phasor fluorescence lifetime imaging method.

Since NADH fluorescence emission spectrum partially overlaps with EGFP emission spectra, we moved to a plasmid overexpressing wild type aS without any tag. In both cell models, the one for the study of aS oligomerization and the one for the study of inclusions formation, NADH fluorescence lifetime was changed compared to the control. Average NADH lifetime in cells with aS oligomers or fibrils was consistently different from the average NADH lifetime of the control. This difference was more consistent when the average NADH lifetime was determined in cell cytoplasm, rather than in the whole cell, suggesting that variation in NADH characteristics are likely ascribed to mitochondrial NADH.

In the images fluorescence spots characterized by very long lifetime were present in cells in these two cellular models, suggesting that the observed changes in NADH fluorescence properties may be due to a sequestration of NADH molecules by aS aggregates, as previously proved for other proteins oligomers (Jameson *et al.*, 1989). To verify this idea, we measured fluorescence lifetime of aS aggregated in the presence of NADH *in vitro* and compared the results with free NADH, NADH bound to lactate dehydrogenase and NADH in solution with monomeric recombinant aS. Interestingly, fluorescence lifetime of NADH and aggregated aS show a variation toward larger values compatible with those measured in aS cell models; moreover, it seems that also monomeric aS induce a variation in NADH fluorescence lifetime, maybe through binding.

However, the variations of the NADH lifetime associated aS binding do not depend in a linear way from the dimensions of the species binding NADH and it is difficult to exactly correlate the dimension of the aggregates and the NADH lifetime values.

Spectral phasor method allowed characterizing also the NADH fluorescence properties variation in term of emission spectrum maximum. The maximum for NADH spectrum when it was in the aggregates moved towards shorter wavelengths of about 4 nm with respect to free NADH in solution (from 480.5 nm to 476.6 nm). This result is in good agreement with the estimation of the variation between free and bound NADH emission spectrum maxima (Palero *et al.*, 2011). Moreover, this variation toward shorter wavelengths was reported for NADH spectra obtained from brain slices of mice model for Alzheimer disease, compared with NADH in solution (Büchner *et al.*, 2002). The agreement between our data and the data published by Büchner *et al.*, (2002) further underlines the importance of these findings not only in PD frame, but also as a general hints concerning NADH metabolism impairment in other neurodegenerative disorders.

The possibility of using an intrinsic fluorescence source, i.e. NADH, to monitor aS oligomers and aggregates presence in cell models represents a new dye-free method to study this mechanism and the related toxicity. More importantly, the characterization of NADH fluorescence lifetime and spectra for the detection of aS aggregation could be applied also to animal models and in vivo, providing a new avenue of investigation through a useful and precise endogenous biomarker for the process.

5.2 Alpha-synuclein and 14-3-3 η *in vitro* and in cell models

The results presented in Chapter 4 show how 14-3-3 η isoform, belonging to the 14-3-3 chaperone-like protein family, can interact with PD related protein aS.

14-3-3 η can interact with aS during aS aggregation *in vitro*, rerouting the process and leading to the formation of curved objects that are completely different in term of morphology from aS fibrils. Curved objects formed in the presence of the chaperone are due to a stable interaction between 14-3-3 η and aS. Previous studies in our lab and published results (Sato *et al.*, 2006), lead to the conclusion that the interaction between monomeric aS and dimeric 14-3-3 η *in vitro* does not occur. For this reason and considering the stable interaction that occurs during aS aggregation, we suggest that one of the possible aS species interacting with 14-3-3 η are misfolded aS forms or aS oligomers.

The curved objects show characteristics that are strongly dependent on the amount of 14-3-3 η present in the aggregation assay. Moreover, they share some similarities in term of morphology with the aggregates formed by aS in the presence of other chaperones, as Hsp70 (Luk *et al.*, 2008).

Interestingly, these aS/14-3-3 η aggregates are curved objects similar what was previously observed in aggregates obtained from Alzheimer β-peptide aggregation, which forms fibrils and is linked to Alzheimer's disease etiopathogenesis, in the presence of the protein serum amyloid P component (Janciauskiene *et al.*, 1995).

This evidence suggests that some of these chaperones, but also others (Bandopadhyay and de Belleroche, 2010) could act in a similar manner trying to interfere with aS aggregation process, and that this mechanism could be generalized to other amyloid fibrils forming proteins.

In the case of 14-3-3 proteins, it seems from our data that the effect is exerted specifically by η and τ isoforms, while γ just partially interfere with the aggregation leading to the formation of objects with heights comparable to the one of aS protofibrils. The rationale of isoform specificity in effecting aS aggregation has to be searched with the structural differences among 14-3-3 isoforms, in term of exposed hydrophobic patches and charged residues that

could mediate the interaction. However, considering the high sequence identity among the 14-3-3 proteins, the primary structure by itself could not account for their different propensity to interact with aS during the aggregation process. A more detailed comparative analysis of the ternary structure should be considered, taking into account also the great structural plasticity of aS and the further complexity deriving from the evolving quaternary structure of aS during the aggregation and in cellular environment.

Accordingly, we could not observe the curved objects we found *in vitro* when we transfect 14-3-3 η in cells overexpressing aS; however, we could identify a stable complex formed by aS monomer and 14-3-3 η dimer, mainly localized at the plasma membrane. Therefore, it could be that the interaction occurs between a structured aS, which acquires an alpha-helical conformation when bound to the membrane (Davidson *et al*., 1998; Bartels *et al*., 2010), and dimeric 14-3-3 η, which was also found associated to presynaptic membranes (Martin *et al.*, 1994). This idea was also proposed for other 14-3-3 binding partners (Shikano *et al.*, 2006).

Another interesting idea that we could not verify is that the interaction between the two occurs when aS is phosphorylated at serine 87 and/or 129 (Paleologou *et al*., 2010; Paleologou *et al*., 2008), given the propensity of 14-3-3 proteins to bind phosphorylated motifs in their binding partners (Yang *et al.*, 2006). The proved interaction is in good agreement with the findings of Xu et al., (2002), that observed the presence of 14-3-3η/aS complexes of 54-83 kDa in human primary neurons transfected with aS.

The difficulties in the interpretation of the possible types of interaction between aS and 14-3-3 proteins suggest the need of detailed studies about the mechanism(s) of interactions based on the available tertiary structure of the two proteins.

The overexpression of 14-3-3 η in cells overexpressing aS induces a rescue in aS induced toxicity. This data, together with the fact that the two proteins interact in cells, suggests that the chaperone can be involved in maintaining aS in a non-toxic form, maybe preventing the conversion to aggregation-prone species. This idea is interestingly supported by the fact that in A53T transgenic mice models 14-3-3 η was upregulated in the striatum (Kurz et

al., 2011), as if upregulation is the cellular response for maintaining aS in a non-toxic form.

To further investigate aS and 14-3-3 η interaction and the ability of the chaperone of rescuing aS induced toxicity, we performed aggregation assays *in vitro* triggering aS aggregation with seeds in the presence of 14-3-3 η.

14-3-3 η was not able to interfere with fibrils formation process and the end products of the aggregation were mature fibrils containing 14-3-3 η molecules. This result, together with the fact the beyond a detectable threshold stoiochiometric ratio 14-3-3 η is not able to reroute aS aggregation process toward the formation of curved objects, suggests that chaperone is limited in its effects by the amount of aS present in the aggregation assay. When aS amount is too high, 14-3-3 η cannot deal with workload anymore and it is sequestered into the aggregates and fibrils. From the available immune-TEM data it is difficult to evaluate whether the 14-3-3 η molecules in the fibrils maintain their folded and dimeric state or not.

However, the sequestration of an essential protein for several cellular functions could be considered an additional toxic mechanism to be ascribed to aS aggregates, as suggested and proved in principle by Olzscha *et al.*, (2011) for other chimeric amyloidogenic proteins. This idea could also be inferred from data published by Volpicelli-Daley *et al.*, (2011): they show how synaptic proteins level in neurons cytoplasm is lowered in neurons treated with preformed fibrils and displaying aS aggregates.

The facts that 14-3-3 proteins colocalizes with aS in A53T transgenic mice models (Shirakashi *et al.*, 2006) and that 14-3-3 proteins can be found in LBs in parkinsonian brains (Kawamoto *et al.*, 2002; Berg *et al.*, 2003; Umahara *et al.*, 2012) further support this idea.

Moreover, as previously mentioned, 14-3-3 η upregulation observed in A53T mice models (Kurz *et al.*, 2011) could be seen as a cellular response also to the sequestration of 14-3-3 η molecules by aS and the consequent reduced amount of molecular chaperone available in the cell cytoplasm.

To prove the sequestration of 14-3-3 η by aS aggreagates in cells we overexpressed the protein in cells in which overexpressed aS aggregation was

triggered by seeds. In good agreement with what we found *in vitro*, we could not measure a reduction in aS aggregates dimensions. However, we cannot conclude that no effects are exerted by 14-3-3 η on aS fibrils in this model, because of the limited resolution of the confocal microscope compared to aS fibrils dimensions (200-300 nm of resolution versus fibrils with a diameter of about 7-10 nm and lengths of hundreds of nm or a few μm).

Moreover, 14-3-3 η overexpression in this cellular model did not rescue aS aggregation induced toxicity, as it did in the other cell model.

Measuring the amount of 14-3-3 η in the cytoplasm of cells where aS aggregation is triggered by seeds, compared to cells where aS is only overexpressed, we found a reduction of the chaperone protein in solution. However, this reduction was also true for another overexpressed protein, the enzyme β-galactosidase, totally unrelated to PD. This suggests that the overexpression *per se* may lead to a certain degree of sequestration in a non-specific manner, probably due to molecular crowding.

For this reason, we evaluated the variation in the amount of endogenous soluble 14-3-3 η in a cell model exposed to increasing amounts of seeds used to trigger the aggregation. The results show a high variability, but the trend suggests a decrease in the soluble 14-3-3 η present in these cells, compared to the untreated control.

The large dispersion in these data is probably due to the intrinsic variability of both the amount of overexpressed aS and the amount of up taken seeds. A further source of variability resides on the densitometry method used to evaluate the protein amount in the Western Blot.

However, the variability could also be intrinsic: 14-3-3 η could be upregulated at the level of the messenger RNA in response to the presence of aggregation prone aS, as seen in the A53T mice models (Kurz *et al.*, 2011), determining an increase in the expressed protein. On the contrary, a decrease could be due to sequestration, determining the presence of two competing mechanisms acting on the detectable amount of 14-3-3 η present in the cell cytoplasm. It will be interesting to study the amount of 14-3-3 η messenger RNA, compared to a control, to test this latter hypothesis.

All together these results suggest that 14-3-3 η is able to interfere with aS aggregation process until the amount of aS is not too high or the aggregation has proceeded too much; in that case, the protein is sequestered by aS aggregates, further increasing the aS related toxicity. Considering the broad range of functions that are ascribed to 14-3-3 proteins, further work is needed to understand if these chaperones could be used to conceive any therapeutic strategy to prevent aS aggregation or toxicity (Zhao *et al.*, 2011).

Bibliography

Abeliovich, A., Schmitz, Y., Fariñas, I., Choi-Lundberg, D., Ho, W. H., Castillo, P. E., Shinsky, N., Verdugo, J. M., Armanini, M., Ryan, A., Hynes, M., Phillips, H., Sulzer, D., Rosenthal, A. (2000). Mice lacking alpha-synuclein display functional deficits in the nigrostriatal dopamine system. Neuron *25*, 239-252.

Aioanei, D. (2012). Lazy Shortest Path Computation in DynamicGraphs. Computer Science *13*, 113-117.

Aitken, A. (2006). 14-3-3 proteins: A historic overview. Semin. Cancer Biol. *16*, 162-172.

Allison, J. R., Varnai, P., Dobson, C. M., Vendruscolo, M. (2009). Determination of the free energy landscape of alpha-synuclein using spin label nuclear magnetic resonance measurements. J. Am. Chem. Soc. 131, 18314-18326.

Alvarez-Erviti, L., Seow, Y., Schapira, A. H., Gardiner, C., Sargent, I. L., Wood, M. J., Cooper, J. M. (2011). Lysosomal dysfunction increases exosome-mediated alpha-synuclein release and transmission. Neurobiol. Dis. *42*, 360-367.

Apetri, M. M., Maiti, N. C., Zagorski, M. G., Carey, P. R., Anderson, V. E. (2006). Secondary structure of alpha-synuclein oligomers: characterization by raman and atomic force microscopy. J. Mol. Biol. *355*, 63-71.

Auluck, P. K., Caraveo, G., Lindquist, S. (2010). α-Synuclein: membrane interactions and toxicity in Parkinson's disease. Annu. Rev. Cell. Dev. Biol. *26*, 211-233.

Bandopadhyay, R., de Belleroche, J. (2010). Pathogenesis of Parkinson's disease: emerging role of molecular chaperones. Trends Mol. Med. *16*, 27-36.

Bartels, T., Choi, J. G., Selkoe, D. J. (2011). α-Synuclein occurs physiologically as a helically folded tetramer that resists aggregation. Nature *477*, 107-110.

Bartels, T., Ahlstrom, L. S., Leftin, A., Kamp, F., Haass, C., Brown, M. F., Beyer, K. (2010). The N-terminus of the intrinsically disordered protein α-synuclein triggers membrane binding and helix folding. Biophys J. *99*, 2116-2124.

Baxter, H. C., Liu, W. G., Forster, J. L., Aitken, A., Fraser, J. R. (2002). Immunolocalisation of 14-3-3 isoforms in normal and scrapie-infected murine brain. Neuroscience 109, 5-14.

Berg, D., Holzmann, C., Riess, O. (2003). 14-3-3 proteins in the nervous system. Nat. Rev. Neurosci. *4*, 752-762.

Berman, S. B., Hastings, T. G. (1999) Dopamine oxidation alters mitochondrial respiration and induces permeability transition in brain mitochondria: implications for Parkinson's disease. J. Neurochem. *73*, 1127-1137.

Bertoncini, C. W., Jung, Y. S., Fernandez, C. O., Hoyer, W., Griesinger, C., Jovin, T. M., Zweckstetter, M. (2005). Release of long-range tertiary interactions potentiates aggregation of natively unstructured alpha-synuclein. Proc. Natl. Acad. Sci. USA *102*, 1430-1435.

Bhak, G., Lee, J. H., Hahn, J. S., Paik, S. R. (2009). Granular assembly of alpha-synuclein leading to the accelerated amyloid fibril formation with shear stress. PLoS One 4(1):e4177.

Bisaglia, M., Tessari, I., Pinato, L., Bellanda, M., Giraudo, S., Fasano, M., Bergantino, E., Bubacco, L., Mammi, S. (2005) A topological model of the interaction between alpha-synuclein and sodium dodecyl sulfate micelles. Biochemistry *44*, 329–339.

Bisaglia, M., Tessari, I., Mammi, S., Bubacco, L. (2009). Interaction between alpha-synuclein and metal ions, still looking for a role in the pathogenesis of Parkinson's disease. Neuromolecular Med. *11*, 239-251.

Bonifati, V., Rizzu, P., van Baren, M. J., Schaap, O., Breedveld, G. J., Krieger, E., Dekker, M. C., Squitieri, F., Ibanez, P., Joosse, M., van Dongen, J. W., Vanacore, N., van Swieten, J. C., Brice, A., Meco, G., van Duijn, C. M., Oostra, B. A., Heutink, P. (2003). Mutations in the DJ-1 gene associated with autosomal recessive early-onset parkinsonism. Science *299*, 256-259.

Bortolus, M., Tombolato, F., Tessari, I., Bisaglia, M., Mammi, S., Bubacco, L., Ferrarini, A., Maniero, A. L. (2008). Broken helix in vesicle and micelle-bound alpha-synuclein: insights from site-directed spin labeling-EPR experiments and MD simulations. J. Am. Chem. Soc. *130*, 6690-6691.

Braak, H., Del Tredici, K., Rüb, U., de Vos, R. A., Jansen Steur, E. N., Braak E. (2003). Staging of brain pathology related to sporadic Parkinson's disease. Neruobiol. Aging *24*, 197-211.

Braak, H., de Vos, R. A., Bohl, J., Del Tredici, K. (2006). Gastric alpha-synuclein immunoreactive inclusions in Meissner's and Auerbach's plexuses in cases staged for Parkinson's disease-related brain pathology. Neurosci. Lett. *396*, 67-72.

Bridges, D., Moorhead, G. B. (2005). 14-3-3 proteins: a number of functions for a numbered protein. Sci. STKE (296):re10.

Büchner, M., Huber, R., Sturchler-Pierrat, C., Staufenbiel, M., Riepe, M. W. (2002). Impaired hypoxic tolerance and altered protein binding of NADH in presymptomatic APP23 transgenic mice. Neuroscience *114*, 285-289.

Burré, J., Sharma, M., Tsetsenis, T., Buchman, V., Etherton, M. R., Südhof, T. C. (2010). Alpha-synuclein promotes SNARE-complex assembly in vivo and in vitro. Science *329*, 1663-1667.

Bussell R. Jr., Ramlall, T.F., Eliezer, D. (2005). Helix periodicity, topology, and dynamics of membrane-associated alpha-synuclein. Protein Sci. *14*, 862–872.

Bussell, R. Jr., Eliezer, D. (2004). Effects of Parkinson's disease-linked mutations on the structure of lipid-associated alpha-synuclein. Biochemistry *43*, 4810-4818.

Bustos, D. M., Iglesias, A. A. (2006). Intrinsic disorder is a key characteristic in partners that bind 14-3-3 proteins. Proteins *63*, 35-42.

Butterfield, S. M., Lashuel, H. A. (2010). Amyloidogenic protein-membrane interactions: mechanistic insight from model systems. Angew. Chem. Int. Ed. Engl. *49*, 5628-5654.

Chandra, S. , Chen, X., Rizo, J., Jahn, R., Südhof, T.C. (2003) A broken alpha-helix in folded alpha-synuclein. J. Biol. Chem. *278*, 15313–15318.

Chartier-Harlin, M. C., Kachergus, J., Roumier, C., Mouroux, V., Douay, X., Lincoln, S., Levecque, C., Larvor, L., Andrieux, J., Hulihan, M., Waucquier, N., Defebvre, L., Amouyel, P., Farrer, M., Destée, A. (2004). Alpha-synuclein locus duplication as a cause of familial Parkinson's disease. Lancet *364*, 1167-1169.

Chen, M., Margittai, M., Chen, J., Langen, R. (2007). Investigation of alpha-synuclein fibril structure by site-directed spin labeling. J. Biol. Chem. *282*, 24970-24979.

Choi, W., Zibaee, S., Jakes, R., Serpell, L. C., Davletov, B., Crowther, R. A., Goedert, M. (2004). Mutation E46K increases phospholipid binding and assembly into filaments of human alpha-synuclein. FEBS Lett. *576*, 363-368.

Clayton, D. F., George, J. M. (1998). The synucleins: a family of proteins involved in synaptic function, plasticity, neurodegeneration and disease. Trends Neurosci. *21*, 249-254.

Colla, E., Jensen, P. H., Pletnikova, O., Troncoso, J. C., Glabe, C., Lee, M. K. (2012). Accumulation of toxic α-synuclein oligomer within endoplasmic reticulum occurs in α-synucleinopathy in vivo. J. Neurosci. *32*, 3301-3305.

Comellas, G., Lemkau, L. R., Nieuwkoop, A. J., Kloepper, K. D., Ladror, D. T., Ebisu, R., Woods, W. S., Lipton, A. S., George, J. M., Rienstra, C. M. (2011). Structured regions of α-synuclein fibrils include the early-onset Parkinson's disease mutation sites. J. Mol. Biol. *411*, 881-895.

Conway, K. A., Harper, J. D., Lansbury, P. T. (1998). Accelerated in vitro fibril formation by a mutant alpha-synuclein linked to early-onset Parkinson disease. Nat. Med. 4, 1318-1320.

Conway, K. A., Lee, S. J., Rochet, J. C., Ding, T. T., Williamson, R. E., Lansbury, P. T. Jr. (2000). Acceleration of oligomerization, not fibrillization, is a shared property of both alpha-synuclein mutations linked to early-onset Parkinson's disease: implications for pathogenesis and therapy. Proc. Natl. Acad. Sci. USA *97*, 571-576.

Cremades, N., Cohen, S. I., Deas, E., Abramov, A. Y., Chen, A. Y., Orte, A., Sandal, M., Clarke, R. W., Dunne, P., Aprile, F. A., Bertoncini, C. W., Wood, N. W., Knowles, T. P., Dobson, C. M., Klenerman, D. (2012). Direct observation of the interconversion of normal and toxic forms of α-synuclein. Cell *149*, 1048-1059.

Danzer KM, Krebs SK, Wolff M, Birk G, Hengerer B. (2009). Seeding induced by alpha-synuclein oligomers provides evidence for spreading of alpha-synuclein pathology. J. Neurochem. *111*, 192-203.

Dauer, W., Przedborski, S. (2003). Parkinson's disease: mechanisms and models. Neuron *39*, 889-909.

Davidson, W.S., Jonas, A., Clayton, D.F., George, J.M. (1998). Stabilization of alpha-synuclein secondary structure upon binding to synthetic membranes. J. Biol. Chem. *273*, 9443–9449.

de Lau, L. M., Breteler, M. M. (2006). Epidemiology of Parkinson's disease. Lancet Neurol *5*, 525-535.

Dedmon, M. M., Lindorff-Larsen, K., Christodoulou, J., Vendruscolo, M., Dobson, C. M. (2005). Mapping long-range interactions in alpha-synuclein using spin-label NMR and ensemble molecular dynamics simulations. J. Am. Chem. Soc. *127*, 476-477.

Dedmon, M. M., Christodoulou, J., Wilson, M. R., Dobson, C. M. (2005). Heat shock protein 70 inhibits alpha-synuclein fibril formation via preferential binding to prefibrillar species. J. Biol. Chem. *280*, 14733-14740.

Der-Sarkissian, A., Jao, C. C., Chen, J., Langen, R. (2003). Structural organization of alpha-synuclein fibrils studied by site-directed spin labeling. J. Biol. Chem. *278*, 37530-37535.

Desplats, P., Lee, H. J., Bae, E. J., Patrick, C., Rockenstein, E., Crews, L., Spencer, B., Masliah, E., Lee, S. J. (2009). Inclusion formation and neuronal cell death through neuron-to-neuron transmission of alpha-synuclein. Proc. Natl. Acad. Sci. USA *106*, 13010-13015.

Di Fonzo, A., Chien, H. F., Socal, M., Giraudo, S., Tassorelli, C., Iliceto, G., Fabbrini, G., Marconi, R., Fincati, E., Abbruzzese, G., Marini, P., Squitieri, F., Horstink, M. W., Montagna, P., Libera, A. D., Stocchi, F., Goldwurm, S., Ferreira, J. J., Meco, G., Martignoni, E., Lopiano, L., Jardim, L. B., Oostra, B. A., Barbosa, E. R.; Italian Parkinson Genetics Network, Bonifati, V. (2007). ATP13A2 missense mutations in juvenile parkinsonism and young onset Parkinson disease. Neurology *68*, 1557-1562.

Dickson, D. W., Fujishiro, H., Orr, C., DelleDonne. A., Josephs, K. A., Frigerio, R., Burnett, M., Parisi, J. E., Klos, K. J., Ahlskog, J. E. (2009). Neuropathology of non-motor features of Parkinson disease. Parkinsonism Relat. Disord. *15*, S1-S5.

Digman, M. A., Dalal, R., Horwitz, A. F., Gratton, E. (2008) (a). Mapping the number of molecules and brightness in the laser scanning microscope. Biophys. J. *94*, 2320-2332.

Digman, M. A., Brown, C. M., Sengupta, P., Wiseman, P. W., Horwitz, A. R., Gratton, E. (2005). Measuring fast dynamics in solutions and cells with a laser scanning microscope. Biophys J. *89*, 1317-1327.

Digman, M. A., Caiolfa, V. R., Zamai, M., Gratton, E. (2008) (b). The phasor approach to fluorescence lifetime imaging analysis. Biophys J. *94*, L14-L16.

Digman, M. A., Gratton, E. (2011). Lessons in fluctuation correlation spectroscopy. Annu. Rev. Phys. Chem. *62*, 645-668.

Digman, M. A., Wiseman, P. W., Choi, C., Horwitz, A. R., Gratton, E. (2009) (a). Stoichiometry of molecular complexes at adhesions in living cells. Proc. Natl. Acad. Sci. USA 106, 2170-2175.

Digman, M. A., Wiseman, P. W., Horwitz, A. R., Gratton, E. (2009) (b). Detecting protein complexes in living cells from laser scanning confocal image sequences by the cross correlation raster image spectroscopy method. Biophys. J. *96*, 707-716.

Dzamko, N., Deak, M., Hentati, F., Reith, A. D., Prescott, A. R., Alessi, D. R., Nichols, R. J. (2010). Inhibition of LRRK2 kinase activity leads to dephosphorylation of Ser(910)/Ser(935), disruption of 14-3-3 binding and altered cytoplasmic localization. Biochem. J. *430*, 405-413.

Dobson, C. M. (1999). Protein Misfolding, Evolution and Disease. Trends Biochem. Sci. *24*, 329-332.

Ebrahimi-Fakhari, D., Wahlster, L., McLean, P. J. (2012). Protein degradation pathways in Parkinson's disease: curse or blessing. Acta Neuropathol. *124*, 153-172.

Ebrahimi-Fakhari, D., Wahlster, L., McLean, P. J. (2011). Molecular Chaperones in Parkinson's Disease - Present and Future. J. Parkinsons Dis. *1*, 299-320.

El-Agnaf, O. M., Paleologou, K. E., Greer, B., Abogrein, A. M., King, J. E., Salem, S. A., Fullwood, N. J., Benson, F. E., Hewitt, R., Ford, K. J., Martin, F. L., Harriott, P., Cookson, M. R., Allsop, D. (2004). A strategy for designing inhibitors of alpha-synuclein aggregation and toxicity as a novel treatment for Parkinson's disease and related disorders. FASEB J. *18*, 1315-1317.

Fauvet, B., Mbefo, M. K., Fares, M. B., Desobry, C., Michael, S., Ardah, M. T., Tsika, E., Coune, P., Prudent, M., Lion, N. , Eliezer, D., Moore, D. J., Schneider, B., Aebischer, P., El-Agnaf, O. M., Masliah, E., Lashuel, H. A. (2012). α-Synuclein in central nervous system and from erythrocytes, mammalian cells, and Escherichia coli exists predominantly as disordered monomer, J. Biol. Chem. *287*, 15345-15364.

Feng, L. R., Federoff, H. J., Vicini, S., Maguire-Zeiss, K. A. (2010). Alpha-synuclein mediates alterations in membrane conductance: a potential role for alpha-synuclein oligomers in cell vulnerability. Eur. J. Neurosci. *32*, 10-7.

Fereidouni, F., Bader, A. N., Gerritsen, H. C. (2012). Spectral phasor analysis allows rapid and reliable unmixing of fluorescence microscopy spectral images. Opt. Express. *20*, 12729-12741.

Ferreon, A.C.M., Gambin, Y., Lemke, E.A., Deniz, A.A. (2009). Interplay of alpha-synuclein binding and conformational switching probed by single-molecule fluorescence. Proc. Natl. Acad. Sci. USA *106*, 5645-5650.

Foote, M., Zhou, Y. (2012). 14-3-3 proteins in neurological disorders. Int. J. Biochem. Mol. Biol. 3, 152-164.

Fredenburg, R. A., Rospigliosi, C., Meray, R. K., Kessler, J. C., Lashuel, H. A., Eliezer, D., Lansbury, P. T. Jr. (2007). The impact of the E46K mutation on the properties of alpha-synuclein in its monomeric and oligomeric states. Biochemistry *46*, 7107-7118.

Freundt, E. C., Maynard, N., Clancy, E. K., Roy, S., Bousset, L., Sourigues, Y., Covert, M., Melki, R., Kirkegaard, K., Brahic, M. (2012). Neuron-to-neuron transmission of α-synuclein fibrils through axonal transport. Ann. Neurol. *72*, 517-524.

Fuchs, J., Tichopad, A., Golub, Y., Munz, M., Schweitzer, K. J., Wolf, B., Berg, D., Mueller, J. C., Gasser, T. (2008). Genetic variability in the SNCA gene influences alpha-synuclein levels in the blood and brain. FASEB J. *22*, 1327-1334.

Fujiwara, H., Hasegawa, M., Dohmae, N., Kawashima, A., Masliah, E., Goldberg, M. S., Shen, J., Takio, K., Iwatsubo, T. (2002). alpha-Synuclein is phosphorylated in synucleinopathy lesions. Nat. Cell. Biol. *4*, 160-164.

Funayama, M., Hasegawa, K., Ohta, E., Kawashima, N., Komiyama, M., Kowa, H., Tsuji, S., Obata, F. (2002). An LRRK2 mutation as a cause for the parkinsonism in the original PARK8 family. Ann. Neurol. *57*, 918-921.

Gardino, A. K., Smerdon, S. J., Yaffe, M. B. (2006). Structural determinants of 14-3-3 binding specificities and regulation of subcellular localization of 14-3-3-ligand complexes: a comparison of the X-ray crystal structures of all human 14-3-3 isoforms. Semin. Cancer Biol. *16*, 173-182.

Gasser, T., Hardy, J., Mizuno, Y. (2011). Milestones in PD genetics. Mov Disord. 26, 1042-1048.

Georgieva, E.R., Ramlall, T.F., Borbat, P.P., Freed, J.H., Eliezer, D. (2010). The lipid-binding domain of wild type and mutant alpha-synuclein: compactness and interconversion between the broken and extended helix forms, J. Biol. Chem. *285*, 28261–28274.

Giasson, B. I., Murray, I. V., Trojanowski, J. Q., Lee, V. M. (2001). A hydrophobic stretch of 12 amino acid residues in the middle of alpha-synuclein is essential for filament assembly. J. Biol. Chem. *276*, 2380-2386.

Giehm L, Svergun DI, Otzen DE, Vestergaard B. (2011) (b). Low-resolution structure of a vesicle disrupting α-synuclein oligomer that accumulates during fibrillation. Proc. Natl. Acad. Sci. USA *108*, 3246-3251.

Giehm, L., Lorenzen, N., Otzen, D. E. (2011). Assays for α-synuclein aggregation. Methods *53*, 295-305.

Goedert, M., Spillantini, M. G., Del Tredici, K., Braak, H. (2012). 100 years of Lewy pathology. Nat. Rev. Neurol. *9*, 13-24.

Gosavi, N., Lee, H. J., Lee, J. S., Patel, S., Lee, S. J. (2002). Golgi fragmentation occurs in the cells with prefibrillar alpha-synuclein aggregates and precedes the formation of fibrillar inclusion. J. Biol. Chem. 277, 48984-48992.

Gousset, K., Schiff, E., Langevin, C., Marijanovic, Z., Caputo, A., Browman, D. T., Chenouard, N., de Chaumont, F., Martino, A., Enninga, J., Olivo-Marin, J. C., Männel, D., Zurzolo, C. (2009). Prions hijack tunnelling nanotubes for intercellular spread. Nat. Cell Biol. *11*, 328-336.

Hansen, C., Angot, E., Bergström, A. L., Steiner, J. A., Pieri, L., Paul, G., Outeiro, T. F., Melki, R., Kallunki, P., Fog, K., Li, J. Y., Brundin, P. (2011). α-Synuclein propagates from mouse brain to grafted dopaminergic neurons and seeds aggregation in cultured human cells. J. Clin. Invest. *121*, 715-725.

Hardy, J. (2010). Genetic analysis of pathways to Parkinson disease. Neuron *68*, 201-206.

Hearps, A. C., Pryor, M. J., Kuusisto, H. V., Rawlinson, S. M., Piller, S. C., Jans, D. A. (2007). The biarsenical dye Lumio exhibits a reduced ability to specifically detect tetracysteine-containing proteins within live cells. J. Fluoresc. *17*, 593-597.

Heise, H., Hoyer, W., Becker, S., Andronesi, O. C,, Riedel, D., Baldus, M. (2005). Molecular-level secondary structure, polymorphism, and dynamics of full-length alpha-synuclein fibrils studied by solid-state NMR. Proc. Natl. Acad. Sci. USA *102*, 15871-15876.

Hinde, E., Digman, M. A., Hahn, K. M., Gratton, E. (2012). Millisecond spatiotemporal dynamics of FRET biosensors by the pair correlation function and the phasor approach to FLIM. Proc. Natl. Acad. Sci. USA *110*, 135-140.

Hoyer, W., Antony, T., Cherny, D., Heim, G., Jovin, T. M., Subramaniam, V. (2002). Dependence of alpha-synuclein aggregate morphology on solution conditions. J. Mol. Biol. *322*, 383-393.

Huang, C., Ren, G., Zhou, H., Wang, C. C. (2005). A new method for purification of recombinant human alpha-synuclein in Escherichia coli. Protein. Expr. Purif. *42*, 173–177.

Jameson, D. M., Thomas, V., Zhou, D. M. (1989). Time-resolved fluorescence studies on NADH bound to mitochondrial malate dehydrogenase. Biochim Biophys Acta. *994*, 187-190.

Janciauskiene, S., García de Frutos, P., Carlemalm, E., Dahlbäck, B., Eriksson, S. (1995). Inhibition of Alzheimer beta-peptide fibril formation by serum amyloid P component. J. Biol. Chem. *270*, 26041-26044.

Jankovic, J., (2008). Parkinson's disease: clinical features and diagnosis. J. Neurol. Neurosurg. Psychiatry *79*, 368-376.

Jao, C.C., Der-Sarkissian, A., Chen, J., Langen, R. (2004). Structure of membrane-bound alpha-synuclein studied by site-directed spin labeling. Proc. Natl. Acad. Sci. USA *101*, 8331–8336.

Jao, C.C., Hegde, B.G., Chen, J., Haworth, I.S., Langen, R. (2008) Structure of membrane-bound alpha-synuclein from site-directed spin labeling and computational refinement. Proc. Natl. Acad. Sci. USA. *105*, 19666–19671.

Jo, E., Fuller, N., Rand, R. P., St George-Hyslop, P., Fraser, P. E. (2002). Defective membrane interactions of familial Parkinson's disease mutant A30P alpha-synuclein. J. Mol. Biol. *315*, 799-807.

Kaminski Schierle, G. S., Bertoncini, C. W., Chan, F. T., van der Goot, A. T., Schwedler, S., Skepper, J., Schlachter, S., van Ham, T., Esposito, A., Kumita, J. R., Nollen, E. A., Dobson, C. M., Kaminski, C. F. (2001). A FRET sensor for non-invasive imaging of amyloid formation in vivo. Chemphyschem *12*, 673-680.

Kawamoto, Y., Akiguchi, I., Nakamura, S., Honjyo, Y., Shibasaki, H., Budka, H. (2002). 14-3-3 proteins in Lewy bodies in Parkinson disease and diffuse Lewy body disease brains. J Neuropathol. Exp. Neurol. *61*, 245-253.

Kaylor, J., Bodner, N., Edridge, S., Yamin, G., Hong, D. P., Fink, A. L. (2005). Characterization of oligomeric intermediates in alpha-synuclein fibrillation: FRET studies of Y125W/Y133F/Y136F alpha-synuclein. J. Mol. Biol. *353*, 357-372.

Khurana, R., Ionescu-Zanetti, C., Pope, M., Li, J., Nielson, L., Ramírez-Alvarado, M., Regan, L., Fink, A. L., Carter, S. A. (2003). A general model for amyloid fibril assembly based on morphological studies using atomic force microscopy. Biophys. J. *85*, 1135-1144.

Kim, H. Y., Cho, M. K., Kumar, A., Maier, E., Siebenhaar, C., Becker, S., Fernandez, C. O., Lashuel, H. A., Benz, R., Lange, A., Zweckstetter, M. (2009). Structural properties of pore-forming oligomers of alpha-synuclein. J. Am. Chem. Soc. *131*, 17482-17489.

Kitada, T., Asakawa, S., Hattori, N., Matsumine, H., Yamamura, Y., Minoshima, S., Yokochi, M., Mizuno, Y., Shimizu, N. (1998). Mutations in the parkin gene cause autosomal recessive juvenile parkinsonism. Nature *392*, 605-608.

Klucken, J., Outeiro, T. F., Nguyen, P., McLean, P. J., Hyman, B. T. (2006). Detection of novel intracellular alpha-synuclein oligomeric species by fluorescence lifetime imaging. FASEB J. *20*, 2050-2057.

Kordower, J. H., Chu, Y., Hauser, R. A., Freeman, T. B., Olanow, C. W. (2008). Lewy body-like pathology in long-term embryonic nigral transplants in Parkinson's disease. Nat. Med. *14*, 504-506.

Krause, M., Fogel, W., Heck, A., Hacke, W., Bonsanto, M., Trenkwalder, C., Tronnier, V. (2001). Deep brain stimulation for the treatment of Parkinson's disease: subthalamic nucleus versus globus pallidus internus. J. Neurol. Neurosurg. Psychiatry *70*, 464–470.

Krüger, R., Kuhn, W., Müller, T., Woitalla, D., Graeber, M., Kösel, S., Przuntek, H., Epplen, J. T., Schöls, L., Riess, O. (1998). Ala30Pro mutation in the gene encoding alpha-synuclein in Parkinson's disease. *18*, 106-108.

Kurz, A., May, C., Schmidt, O., Müller, T., Stephan, C., Meyer, H. E., Gispert, S., Auburger, G., Marcus, K. (2012). A53T-alpha-synuclein-overexpression in the mouse nigrostriatal pathway leads to early increase of 14-3-3 epsilon and late increase of GFAP. J. Neural. Transm. *119*, 297-312.

Lashuel, H. A., Petre, B. M., Wall, J., Simon, M., Nowak, R. J., Walz, T., Lansbury, P. T. Jr. (2002). Alpha-synuclein, especially the Parkinson's disease-associated mutants, forms pore-like annular and tubular protofibrils. J. Mol. Biol. *322*, 1089-1102.

Lee, H. J., Choi, C., Lee, S. J. (2002). Membrane-bound alpha-synuclein has a high aggregation propensity and the ability to seed the aggregation of the cytosolic form. J. Biol. Chem. *277*, 671-678.

Lee, H. J., Khoshaghideh, F., Patel, S., Lee, S. J. (2004). Clearance of alpha-synuclein oligomeric intermediates via the lysosomal degradation pathway. J. Neurosci. *24*, 1888-1896.

Lee, J. H., Hong, C. S., Lee, S., Yang, J. E., Park, Y. I., Lee, D., Hyeon, T., Jung, S., Paik, S. R. (2012). Radiating amyloid fibril formation on the surface of lipid membranes through unit-assembly of oligomeric species of α-synuclein. PLoS One 7(10):e47580.

Lesage, S., Brice, A. (2012). Role of mendelian genes in "sporadic" Parkinson's disease. Parkinsonism Relat. Disord. *18*, S66-S70.

LeVine, H. (1993). Thioflavine T interaction with synthetic Alzheimer's disease beta-amyloid peptides: detection of amyloid aggregation in solution. Protein Sci. *2*, 404-410.

Li, J. Y., Englund, E., Holton, J. L., Soulet, D., Hagell, P., Lees, A. J., Lashley, T., Quinn, N. P., Rehncrona, S., Björklund, A., Widner, H., Revesz, T., Lindvall, O., Brundin, P. (2008). Lewy bodies in grafted neurons in subjects with

Parkinson's disease suggest host-to-graft disease propagation. Nat. Med. *14*, 501-503.

Li, J., Uversky, V. N., Fink, A. L. (2001). Effect of familial Parkinson's disease point mutations A30P and A53T on the structural properties, aggregation, and fibrillation of human alpha-synuclein. Biochemistry *40*, 11604-11613.

Li, X., Wang, Q. J., Pan, N., Lee, S., Zhao, Y., Chait, B. T., Yue, Z. (2011). Phosphorylation-dependent 14-3-3 binding to LRRK2 is impaired by common mutations of familial Parkinson's disease. PLoS One *6*(3):e17153.

Liu, S., Ninan, I., Antonova, I., Battaglia, F., Trinchese, F., Narasanna, A., Kolodilov, N., Dauer, W., Hawkins, R. D., Arancio, O. (2004). alpha-Synuclein produces a long-lasting increase in neurotransmitter release. EMBO J. *23*, 4506-4516.

Lotharius, J., Brundin, P. (2002). Pathogenesis of Parkinson's disease: dopamine, vesicles and α-synuclein. Nat. Rev. Neurosci. *3*, 932–942.

Luk, K. C., Mills, I. P., Trojanowski, J. Q., Lee, V. M. (2008). Interactions between Hsp70 and the hydrophobic core of alpha-synuclein inhibit fibril assembly. Biochemistry *47*, 12614-12625.

Luk, K. C., Hyde, E. G., Trojanowski, J. Q., Lee, V. M. (2007). Sensitive fluorescence polarization technique for rapid screening of alpha-synuclein oligomerization/fibrillization inhibitors. Biochemistry *46*, 12522-12529.

Luk, K. C., Kehm, V., Carroll, J., Zhang, B., O'Brien, P., Trojanowski, J. Q., Lee, V. M. (2012). Pathological α-synuclein transmission initiates Parkinson-like neurodegeneration in nontransgenic mice. Science *338*, 949-953.

Luk, K. C., Song, C., O'Brien, P., Stieber, A., Branch, J. R., Brunden, K. R., Trojanowski, J. Q., Lee, V. M. (2009). Exogenous alpha-synuclein fibrils seed the formation of Lewy body-like intracellular inclusions in cultured cells. Proc. Natl. Acad. Sci. USA *106*, 20051-20056.

Maguire-Zeiss, K. A., Federoff, H. J. (2010). Future directions for immune modulation in neurodegenerative disorders: focus on Parkinson's disease. J. Neural. Transm. *117*, 1019-1025.

Mak, S. K., McCormack, A. L., Manning-Bog, A. B., Cuervo, A. M., Di Monte, D. A. (2010). Lysosomal degradation of alpha-synuclein in vivo. J. Biol. Chem. *285*, 13621-13629.

Martin, H., Rostas, J., Patel, Y., Aitken, A. (1994). Subcellular localisation of 14-3-3 isoforms in rat brain using specific antibodies. J. Neurochem. 63, 2259-2265.

Mayevsky, A., Rogatsky, G. G. (2007). Mitochondrial function in vivo evaluated by NADH fluorescence: from animal models to human studies. Am. J. Physiol. Cell Physiol. *292*, C615-C640

McLean, P. J., Kawamata, H., Hyman, B. T. (2001). Alpha-synuclein-enhanced green fluorescent protein fusion proteins form proteasome sensitive inclusions in primary neurons. Neuroscience *104*, 901-912.

Middleton, E.R., Rhoades, E. (2010). Effects of curvature and composition on α-synuclein binding to lipid vesicles. Biophys. J. *99*, 2279–2288.

Morris, A. M., Watzky, M. A., Finke, R. G. (2009). Protein aggregation kinetics, mechanism, and curve-fitting: a review of the literature. Biochim. Biophys. Acta *1794*, 375-397.

Mosharov, E. V., Staal, R. G., Bové, J., Prou, D., Hananiya, A., Markov, D., Poulsen, N., Larsen, K. E., Moore, C. M., Troyer, M. D., Edwards, R. H., Przedborski, S., Sulzer, D. (2006). Alpha-synuclein overexpression increases cytosolic catecholamine concentration. J. Neurosci. *26*, 9304-9311.

Nakamura, K., Nemani, V. M., Azarbal, F., Skibinski, G., Levy, J. M., Egami, K., Munishkina, L., Zhang, J., Gardner, B., Wakabayashi, J., Sesaki, H., Cheng, Y., Finkbeiner, S.,Nussbaum, R. L., Masliah, E., Edwards, R. H. (2011). Direct membrane association drives mitochondrial fission by the Parkinson disease-associated protein alpha-synuclein. J. Biol. Chem. *286*, 20710-20726.

Nath, S., Goodwin, J., Engelborghs, Y., Pountney, D. L. (2011). Raised calcium promotes α-synuclein aggregate formation. Mol. Cell. Neurosci. *46*, 516-526.

Nath, S., Meuvis, J., Hendrix, J., Carl, S. A., Engelborghs, Y. (2010). Early aggregation steps in alpha-synuclein as measured by FCS and FRET: evidence for a contagious conformational change. Biophys. J. *98*, 1302-1311.

Necula, M., Chirita, C. N., Kuret, J. (2003). Rapid anionic micelle-mediated alpha-synuclein fibrillization in vitro. J. Biol. Chem. 278, 46674-44680.

Nonaka, T., Hasegawa, M. (2011). In vitro recapitulation of aberrant protein inclusions in neurodegenerative diseases: New cellular models of neurodegenerative diseases. Commun Integr Biol. *4*, 501-502.

Nonaka, T., Watanabe, S. T., Iwatsubo, T., Hasegawa, M. (2010). Seeded aggregation and toxicity of alpha-synuclein and tau: cellular models of neurodegenerative diseases. J. Biol. Chem. *285*, 34885-34898.

Nichols, R. J., Dzamko, N., Morrice, N. A., Campbell, D. G., Deak, M., Ordureau, A., Macartney, T., Tong, Y., Shen, J., Prescott, A. R., Alessi, D. R. (2010). 14-3-3 binding to LRRK2 is disrupted by multiple Parkinson's disease-associated mutations and regulates cytoplasmic localization. Biochem. J. *430*, 393-404.

Obsil, T., Obsilova, V. (2011). Structural basis of 14-3-3 protein functions. Semin. Cell Dev. Biol. *22*, 663-672.

Olzscha, H., Schermann, S. M., Woerner, A. C., Pinkert, S., Hecht, M. H., Tartaglia, G. G., Vendruscolo, M., Hayer-Hartl, M., Hartl, F. U., Vabulas, R. M. (2011). Amyloid-like aggregates sequester numerous metastable proteins with essential cellular functions. Cell *144*, 67-78.

Ossato, G., Digman, M. A., Aiken, C., Lukacsovich, T., Marsh, J. L., Gratton, E. (2010). A two-step path to inclusion formation of huntingtin peptides revealed by number and brightness analysis. Biophys. J. *98*, 3078-3085.

Ostrerova, N., Petrucelli, L., Farrer, M., Mehta, N., Choi, P., Hardy, J., Wolozin, B. (1999). alpha-Synuclein shares physical and functional homology with 14-3-3 proteins. J. Neurosci. *19*, 5782-5791.

Outeiro, T. F., Putcha, P., Tetzlaff, J. E., Spoelgen, R., Koker, M., Carvalho, F., Hyman, B. T., McLean, P. J. (2008). Formation of toxic oligomeric alpha-synuclein species in living cells. PLoS One *3*(4):e1867.

Paleologou, K. E., Oueslati, A., Shakked, G., Rospigliosi, C. C., Kim, H. Y., Lamberto, G. R., Fernandez, C. O., Schmid, A., Chegini, F., Gai, W. P., Chiappe, D., Moniatte, M.,Schneider, B. L., Aebischer, P., Eliezer, D., Zweckstetter, M., Masliah, E., Lashuel, H. A. (2010). Phosphorylation at S87 is enhanced in synucleinopathies, inhibits alpha-synuclein oligomerization, and influences synuclein-membrane interactions. J. Neurosci. *30*, 3184-3198.

Paleologou, K. E., Schmid, A. W., Rospigliosi, C. C., Kim, H. Y., Lamberto, G. R., Fredenburg, R. A., Lansbury, P. T. Jr., Fernandez, C. O., Eliezer, D., Zweckstetter, M., Lashuel, H. A. (2008). Phosphorylation at Ser-129 but not the phosphomimics S129E/D inhibits the fibrillation of alpha-synuclein. J. Biol. Chem. *283*, 16895-16905.

Palero, J. A., Bader, A. N., de Bruijn, H. S., der Ploeg van den Heuvel, A., Sterenborg, H. J., Gerritsen, H. C. (2011). In vivo monitoring of protein-bound and free NADH during ischemia by nonlinear spectral imaging microscopy. Biomed Opt Express. *2*, 1030-1039.

Patterson, G. H., Knobel, S. M., Sharif, W. D., Kain, S. R., Piston, D. W. (1997). Use of the Green Fluorescent Protein and Its Mutants in Quantitative Fluorescence Microscopy. Biophys. J. *73*, 2782-2790.

Perrin, R. J., Woods, W. S., Clayton, D. F., George, J. M. (2000). Interaction of human alpha-Synuclein and Parkinson's disease variants with phospholipids. Structural analysis using site-directed mutagenesis. J. Biol. Chem. *275*, 34393-34398.

Politis, M., Lindvall, O. (2012). Clinical application of stem cell therapy in Parkinson's disease. BMC Med. 10:1.

Polymeropoulos, M. H., Lavedan, C., Leroy, E., Ide, S. E., Dehejia, A., Dutra, A., Pike, B., Root, H., Rubenstein, J., Boyer, R., Stenroos, E. S., Chandrasekharappa, S., Athanassiadou, A., Papapetropoulos, T., Johnson, W. G., Lazzarini, A. M., Duvoisin, R. C., Di Iorio, G., Golbe, L. I., Nussbaum, R. L. (1997). Mutation in the alpha-synuclein gene identified in families with Parkinson's disease. Science *276*, 2045-2047.

Pountney, D. L., Lowe, R., Quilty, M., Vickers, J. C., Voelcker, N. H., Gai, W. P. (2004). Annular alpha-synuclein species from purified multiple system atrophy inclusions. J. Neurochem. *90*, 502-512.

Qin, Z., Hu, D., Han, S., Hong, D. P., Fink, A. L. (2007). Role of different regions of alpha-synuclein in the assembly of fibrils. Biochemistry *46*, 13322-13330.

Ramirez, A., Heimbach, A., Gründemann, J., Stiller, B., Hampshire, D., Cid, L. P., Goebel, I., Mubaidin, A. F., Wriekat, A. L., Roeper, J., Al-Din, A., Hillmer, A. M., Karsak, M., Liss, B.,Woods, C. G., Behrens, M. I., Kubisch, C. (2006). Hereditary parkinsonism with dementia is caused by mutations in ATP13A2, encoding a lysosomal type 5 P-type ATPase. Nat. Genet. *38*, 1184–1191.

Reynolds, N. P., Soragni, A., Rabe, M., Verdes, D., Liverani, E., Handschin, S., Riek, R., Seeger, S. (2011). Mechanism of membrane interaction and disruption by α-synuclein. J. Am. Chem. Soc. *133*, 19366-19375.

Roberti MJ, Jovin TM, Jares-Erijman E. (2011). Confocal fluorescence anisotropy and FRAP imaging of α-synuclein amyloid aggregates in living cells. PLoS One *6*(8):e23338.

Roberti, M. J., Bertoncini, C. W., Klement, R., Jares-Erijman, E. A., Jovin, T. M. (2007). Fluorescence imaging of amyloid formation in living cells by a functional, tetracysteine-tagged alpha-synuclein. Nat Methods *4*, 345-351.

Ross, C. A., Poirier, M. A. (2005). What is the role of protein aggregation in neurodegeneration? Nat. Rev. Mol. Cell. Biol. 6, 891-898.

Rossow, M. J., Sasaki, J. M., Digman, M. A., Gratton, E. (2010). Raster image correlation spectroscopy in live cells. Nat. Protoc. *5*, 1761-1774.

Sato, S., Chiba, T., Sakata, E., Kato, K., Mizuno, Y., Hattori, N., Tanaka, K. (2006). 14-3-3eta is a novel regulator of parkin ubiquitin ligase. EMBO J. *25*, 211-221.

Schapira, A.H. (2009). Neurobiology and treatment of Parkinson's disease. Trends Pharmacol Sci *30*, 41-47.

Serpell, L. C., Berriman, J., Jakes, R., Goedert, M., Crowther, R. A. (2000). Fiber diffraction of synthetic alpha-synuclein filaments shows amyloid-like cross-beta conformation. Proc. Natl. Acad. Sci. USA *97*, 4897-4902.

Sherer, N. M., Mothes, W. (2008). Cytonemes and tunneling nanotubules in cell-cell communication and viral pathogenesis. Trends Cell Biol. *18*, 414-420.

Shikano, S., Coblitz, B., Wu, M., Li, M. (2006). 14-3-3 proteins: regulation of endoplasmic reticulum localization and surface expression of membrane proteins. Trends Cell Biol. *16*, 370-375.

Shirakashi, Y., Kawamoto, Y., Tomimoto, H., Takahashi, R., Ihara, M. (2006). alpha-Synuclein is colocalized with 14-3-3 and synphilin-1 in A53T transgenic mice. Acta Neuropathol. *112*, 681-689.

Sievers, S. A., Karanicolas, J., Chang, H. W., Zhao, A., Jiang, L., Zirafi, O., Stevens, J. T., Münch, J., Baker, D., Eisenberg, D. (2011). Structure-based design of non-natural amino-acid inhibitors of amyloid fibril formation. Nature *475*, 96-100.

Singleton, A. B., Farrer, M., Johnson, J., Singleton, A., Hague, S., Kachergus, J., Hulihan, M., Peuralinna, T., Dutra, A., Nussbaum, R., Lincoln, S., Crawley, A., Hanson, M., Maraganore, D., Adler, C., Cookson, M. R., Muenter, M., Baptista, M., Miller, D., Blancato, J., Hardy, J., Gwinn-Hardy, K. (2003). alpha-Synuclein locus triplication causes Parkinson's disease. Science 302, 841.

Slone, S. R., Lesort, M., Yacoubian, T. A. (2011). 14-3-3theta protects against neurotoxicity in a cellular Parkinson's disease model through inhibition of the apoptotic factor Bax. PLoS One *6*(7):e21720.

Smith, W. W., Jiang, H., Pei, Z., Tanaka, Y., Morita, H., Sawa, A., Dawson, V. L., Dawson, T. M., Ross, C. A. (2005). Endoplasmic reticulum stress and mitochondrial cell death pathways mediate A53T mutant alpha-synuclein-induced toxicity. Hum. Mol. Genet. *14*, 3801-3811.

Spillantini, M. G., Crowther, R. A., Jakes, R., Hasegawa, M., Goedert, M. (1998) alpha-Synuclein in filamentous inclusions of Lewy bodies from Parkinson's disease and dementia with lewy bodies. Proc. Natl. Acad. Sci. USA *95*, 6469-6473.

Steinacker, P., Aitken, A., Otto, M. (2011). 14-3-3 proteins in neurodegeneration. Semin. Cell. Dev. Biol. 22, 696-704.

Stringari, C., Cinquin, A., Cinquin, O., Digman, M. A., Donovan, P. J., Gratton, E. (2011). Phasor approach to fluorescence lifetime microscopy distinguishes different metabolic states of germ cells in a live tissue. Proc. Natl. Acad. Sci. USA *108*, 13582-13587.

Stringari, C., Nourse, J. L., Flanagan, L. A., Gratton, E. (2012). Phasor fluorescence lifetime microscopy of free and protein-bound NADH reveals neural stem cell differentiation potential. PLoS One *7*,(11):e48014.

Stroffekova, K., Proenza, C., Beam, K. G. (2001). The protein-labeling reagent FLASH-EDT2 binds not only to CCXXCC motifs but also non-specifically to endogenous cysteine-rich proteins. Pflugers Arch. *442*, 859-866.

Takahashi, T., Mihara, H. (2008). Peptide and protein mimetics inhibiting amyloid beta-peptide aggregation. Acc. Chem. Res. *41*, 1309-1318.

Tanaka, Y., Engelender, S., Igarashi, S., Rao, R. K., Wanner, T., Tanzi, R. E., Sawa, A., Dawson, V. L., Dawson, T. M., Ross, C. A. (2001). Inducible

expression of mutant alpha-synuclein decreases proteasome activity and increases sensitivity to mitochondria-dependent apoptosis. Hum. Mol. Genet. *10*, 919-926.

Tofaris, G. K. (2012) Lysosome-dependent pathways as a unifying theme in Parkinson's disease. Mov. Disord. *27*, 1364-1369.

Tosatto, L., Andrighetti, A. O., Plotegher, N., Antonini, V., Tessari, I., Ricci, L., Bubacco, L., Dalla Serra, M. (2012). Alpha-synuclein pore forming activity upon membrane association. Biochim Biophys Acta. 1818, 2876-2883.

Trexler, A.J., Rhoades, E. (2009). Alpha-synuclein binds large unilamellar vesicles as an extended helix. Biochemistry *48*, 2304–2306.

Trexler, A. J., Rhoades, E. (2010). Single molecule characterization of α-synuclein in aggregation-prone states. Biophys. J. *99*, 3048-3055.

Tsigelny, I. F., Bar-On, P., Sharikov, Y., Crews, L., Hashimoto, M., Miller, M. A., Keller, S. H., Platoshyn, O., Yuan, J. X,, Masliah, E. (2007). Dynamics of alpha-synuclein aggregation and inhibition of pore-like oligomer development by beta-synuclein. FEBS J. *274*, 1862-1877.

Ubl, A., Berg, D., Holzmann, C., Krüger, R., Berger, K., Arzberger, T., Bornemann, A., Riess, O. (2002). 14-3-3 protein is a component of Lewy bodies in Parkinson's disease-mutation analysis and association studies of 14-3-3 eta. Brain Res. Mol. Brain Res. *108*, 33-9.

Ulmer, T.S., Bax, A., Cole, N.B., Nussbaum, R.L. (2005). Structure and dynamics of micelle-bound human alpha-synuclein. J. Biol. Chem. *280*, 9595–9603.

Umahara, T., Uchihara, T., Iwamoto, T. (2012). Structure-oriented review of 14-3-3 protein isoforms in geriatric neuroscience. Geriatr. Gerontol. Int. *12*, 586-599.

Uversky, V. N., Yamin, G., Souillac, P. O., Goers, J., Glaser, C. B., Fink, A. L. (2002). Methionine oxidation inhibits fibrillation of human alpha-synuclein in vitro. FEBS Lett. *517*, 239-244.

Valente, E. M., Abou-Sleiman, P. M., Caputo, V., Muqit, M. M., Harvey, K., Gispert, S., Ali, Z., Del Turco, D., Bentivoglio, A. R., Healy, D. G., Albanese, A., Nussbaum, R., González-Maldonado, R., Deller, T., Salvi, S., Cortelli, P., Gilks, W. P., Latchman, D. S., Harvey, R. J., Dallapiccola, B., Auburger, G., Wood, N. W. (2004). Hereditary early-onset Parkinson's disease caused by mutations in PINK1. Science *304*, 1158-1160.

van Ham, T. J., Esposito, A., Kumita, J. R., Hsu, S. T., Kaminski Schierle, G. S., Kaminski, C. F., Dobson, C. M., Nollen, E. A., Bertoncini, C. W. (2010). Towards multiparametric fluorescent imaging of amyloid formation: studies of a YFP model of alpha-synucleinaggregation. J. Mol. Biol. *395*, 627-642.

van Raaij, M. E., Segers-Nolten, I. M., Subramaniam, V. (2006). Quantitative morphological analysis reveals ultrastructural diversity of amyloid fibrils from alpha-synucleinmutants. Biophys. J. *91*, L96-L98.

van Raaij, M. E., van Gestel, J., Segers-Nolten, I. M., de Leeuw, S. W., Subramaniam, V. (2008). Concentration dependence of alpha-synuclein fibril length assessed by quantitative atomic force microscopy and statistical-mechanical theory. Biophys. J. *95*, 4871-4878.

van Rooijen, B. D., Claessens, M. M., Subramaniam, V. (2010). Membrane Permeabilization by Oligomeric α-Synuclein: In Search of the Mechanism. PLoS One *5*(12):e14292.

van Hemert, M. J., Niemantsverdriet, M., Schmidt, T., Backendorf, C., Spaink, H. P. (2004). Isoform-specific differences in rapid nucleocytoplasmic shuttling cause distinct subcellular distributions of 14-3-3sigma and 14-3-3 zeta. J. Cell. Sci. *117*, 1411-1420.

Varkey, J., Isas, J. M., Mizuno, N., Jensen, M. B., Bhatia, V. K., Jao, C. C., Pelova, J., Voss, J. C., Stamou, D. G., Steven, A. C., Langen, R. (2010). Membrane curvature induction and tubulation are common features of synucleins and apolipooteins. J. Biol. Chem. *285*, 32486-32493.

Vilar, M., Chou, H. T., Lührs, T., Maji, S. K., Riek-Loher, D., Verel, R., Manning, G., Stahlberg, H., Riek, R. (2008). The fold of alpha-synuclein fibrils. Proc. Natl. Acad. Sci. USA *105*, 8637-8642.

Volpicelli-Daley, L. A., Luk, K. C., Patel, T. P., Tanik, S. A., Riddle, D. M., Stieber, A., Meaney, D. F., Trojanowski, J. Q., Lee, V. M. (2011). Exogenous α-synuclein fibrils induce Lewy body pathology leading to synaptic dysfunction and neuron death. Neuron *72*, 57-71.

Wang, J., Lou, H., Pedersen, C. J., Smith, A. D., Perez, R. G. (2009). 14-3-3zeta contributes to tyrosine hydroxylase activity in MN9D cells: localization of dopamine regulatory proteins to mitochondria. J. Biol. Chem. *284*, 14011-14019.

Waxman, E. A., Giasson, B. I. (2010). A novel, high-efficiency cellular model of fibrillar alpha-synuclein inclusions and the examination of mutations that inhibit amyloid formation. J. Neurochem. *113*, 374-388.

Weinreb, P. H., Zhen, W., Poon, A. W., Conway, K. A., Lansbury, P. T. Jr. (1996). NACP, a protein implicated in Alzheimer's disease and learning, is natively unfolded. Biochemistry *35*, 13709-13715.

Winner, B., Jappelli, R., Maji, S. K., Desplats, P. A., Boyer, L., Aigner, S., Hetzer, C., Loher, T., Vilar, M., Campioni, S., Tzitzilonis, C., Soragni, A., Jessberger, S., Mira, H., Consiglio, A., Pham, E., Masliah, E., Gage, F. H., Riek, R. (2011). In vivo demonstration that alpha-synuclein oligomers are toxic. Proc. Natl. Acad. Sci. USA *108*, 4194-4199.

Wood, S. J., Wypych, J., Steavenson, S., Louis, J. C., Citron, M., Biere, A. L. (1999). alpha-synuclein fibrillogenesis is nucleation-dependent. Implications for the pathogenesis of Parkinson's disease. J. Biol. Chem. *274*, 19509-19512.

Xia, Q., Liao, L., Cheng, D., Duong, D. M., Gearing, M., Lah, J. J., Levey, A. I., Peng, J. (2008). Proteomic identification of novel proteins associated with Lewy bodies. Front. Biosci. *13*, 3850-3856.

Xu, J., Kao, S. Y., Lee, F. J., Song, W., Jin, L. W., Yankner, B. A. (2002). Dopamine-dependent neurotoxicity of alpha-synuclein: a mechanism for selective neurodegeneration in Parkinson disease. Nat. Med. *8*, 600-606.

Yacoubian, T. A., Slone, S. R., Harrington, A. J., Hamamichi, S., Schieltz, J. M., Caldwell, K. A., Caldwell, G. A., Standaert, D. G. (2010). Differential neuroprotective effects of 14-3-3 proteins in models of Parkinson's disease. Cell Death. Dis. 1:e2.

Yamin, G., Uversky, V. N., Fink, A. L. (2003). Nitration inhibits fibrillation of human alpha-synuclein in vitro by formation of soluble oligomers. FEBS Lett. 542, 147-152.

Yang, X., Lee, W. H., Sobott, F., Papagrigoriou, E., Robinson, C. V., Grossmann, J. G., Sundström, M., Doyle, D. A., Elkins, J. M. (2006). Structural basis for protein-protein interactions in the 14-3-3 protein family. Proc. Natl. Acad. Sci. USA *103*, 17237-17242.

Yap, T. L., Pfefferkorn, C. M., Lee, J. C. (2011). Residue-specific fluorescent probes of α-synuclein: detection of early events at the N- and C-termini during fibril assembly. Biochemistry *50*, 1963-1965.

Zakharov, S. D., Hulleman, J. D., Dutseva, E. A., Antonenko, Y. N., Rochet, J. C., Cramer, W. A. (2007). Helical alpha-synuclein forms highly conductive ion channels. Biochemistry *46*, 14369-14379.

Zarranz, J. J., Alegre, J., Gómez-Esteban, J. C., Lezcano, E., Ros, R., Ampuero, I., Vidal, L., Hoenicka, J., Rodriguez, O., Atarés, B., Llorens, V., Gomez Tortosa, E., del Ser, T., Muñoz, D. G., de Yebenes, J. G. (2004). The new mutation, E46K, of alpha-synuclein causes Parkinson and Lewy body dementia. Ann. Neurol. *55*, 164-173.

Zhao, J., Meyerkord, C. L., Du, Y., Khuri, F. R., Fu, H. (2011). 14-3-3 proteins as potential therapeutic targets. Semin Cell Dev Biol. *22*, 705-712.

Zimprich, A., Benet-Pagès, A., Struhal, W., Graf, E., Eck, S. H., Offman, M. N., Haubenberger, D., Spielberger, S., Schulte, E. C., Lichtner, P., Rossle, S. C., Klopp, N., Wolf, E., Seppi, K., Pirker, W., Presslauer, S., Mollenhauer, B., Katzenschlager, R., Foki, T., Hotzy, C., Reinthaler, E., Harutyunyan, A., Kralovics, R., Peters, A., Zimprich, F., Brücke, T., Poewe, W., Auff, E., Trenkwalder, C., Rost, B., Ransmayr, G., Winkelmann, J., Meitinger, T., Strom, T. M. (2011). A mutation in VPS35, encoding a subunit of the

retromer complex, causes late-onset Parkinson disease. Am. J. Hum. Genet. *89*, 168-175.